LUND UNIVERSITY

In-Plane Fracture of Paper

Tryding, Johan

1996

Link to publication

Citation for published version (APA):
Tryding, J. (1996). *In-Plane Fracture of Paper* (1 ed.). [Doctoral Thesis (monograph), Structural Mechanics]. Structural Mechanics, Lund University.

Total number of authors:
1

General rights
Unless other specific re-use rights are stated the following general rights apply:
Copyright and moral rights for the publications made accessible in the public portal are retained by the authors and/or other copyright owners and it is a condition of accessing publications that users recognise and abide by the legal requirements associated with these rights.
• Users may download and print one copy of any publication from the public portal for the purpose of private study or research.
• You may not further distribute the material or use it for any profit-making activity or commercial gain
• You may freely distribute the URL identifying the publication in the public portal

Read more about Creative commons licenses: https://creativecommons.org/licenses/

Take down policy
If you believe that this document breaches copyright please contact us providing details, and we will remove access to the work immediately and investigate your claim.

LUND UNIVERSITY

PO Box 117
221 00 Lund
+46 46-222 00 00

LUND UNIVERSITY | LUND INSTITUTE OF TECHNOLOGY
Division of Structural Mechanics | Sweden 1996 | Report TVSM-1008

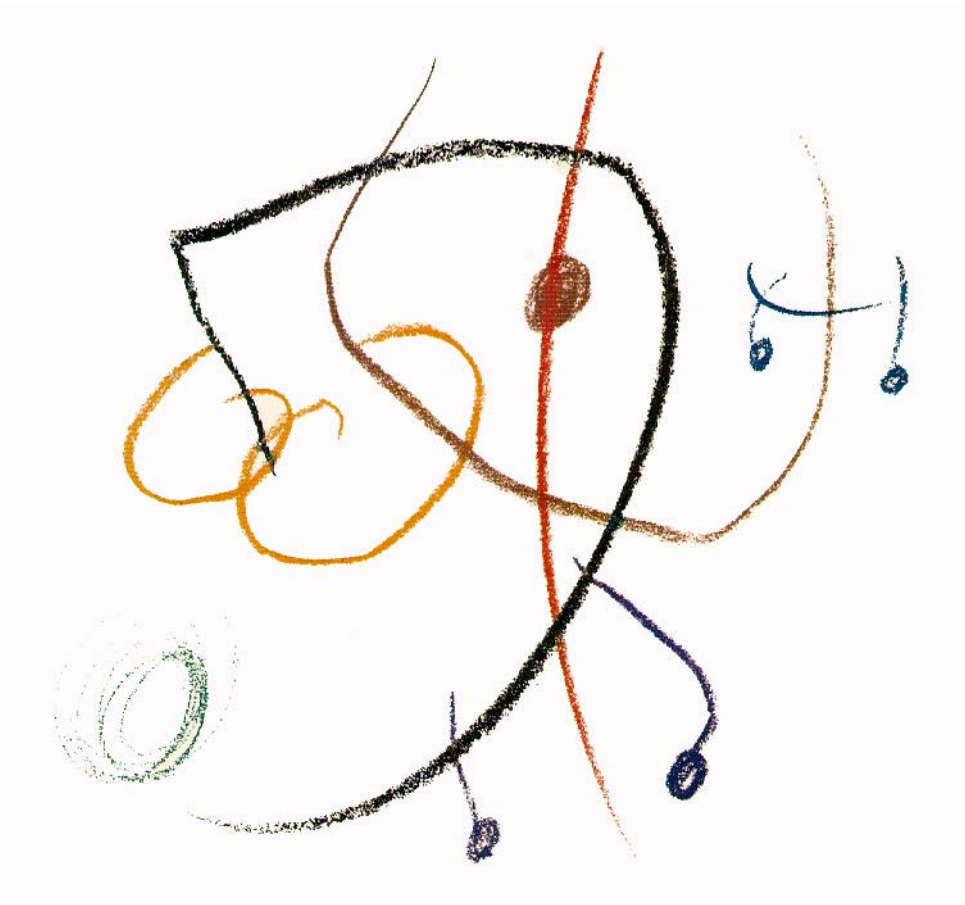

IN-PLANE FRACTURE OF PAPER

JOHAN TRYDING

LUND UNIVERSITY | LUND INSTITUTE OF TECHNOLOGY
Division of Structural Mechanics | Sweden 1996 | Report TVSM-1008
CODEN: LUTVDG/(TVSM-1008)/1-148/(1996) | ISSN 0281-6679

IN-PLANE FRACTURE OF PAPER

JOHAN TRYDING

Acknowledgements

This report comprises results from a research project dealing with fracture mechanics for paper. The work has been carried out at the Division of Structural Mechanics, Lund Institute of Technology. The financial support from Tetra Pak and the Swedish Pulp and Paper Research Foundation is gratefully acknowledged.

I would like to thank my supervisor Docent Per Johan Gustafsson for his guidance, comments and suggestions during the course of the work. Tekn. Dr. Bengt Carlsson at Tetra Pak and Professor Hans Petersson have contributed many valuable discussions, comments and suggestions during the work. Thank you. For comments and suggestions on part of the manuscript I thank Tekn. Dr. Christer Nilsson. For drawing some of the figures I thank Mr. Bo Zadig.

The kind and willing assistance of staff, colleagues and friends at the Division of Structural Mechanics, Tetra Pak and the Department of Solid Mechanics at Lund Institute of Technology is greatly appreciated.

I would also like to express my gratitude to Tetra Pak for giving me access to the paper laboratory and the users' subroutine for the anisotropic elastic-plastic constitutive model developed for Tetra Pak and STFI by A. P. Karafillis, M. C. Boyce and D. M. Parks.

Finally, I thank Associate Professor Richard E. Fisher and my brother Per Tryding for their assistance with my written English.

The illustration on the cover is a reproduction of a drawing made by Joan Miró for Nils Tryding.

Lund in September 1996

Johan Tryding

Abstract

The in-plane failure of paper is studied in this work by means of a cohesive crack model from experimental as well as theoretical perspectives.

Localized damage at in-plane tension of short paper strips is studied for low strain rates. It is observed that under uniaxial in-plane tensile tests, the evolution of the failure is stable and the damage of the paper strip is localized into a narrow zone. The damage in the paper strip develops only after the tensile strength has been reached. The uniaxial fracture properties of paper are defined and characterized by a descending stress-crack widening curve. From this curve the fracture energy can be obtained. A characteristic material parameter of a length dimension is introduced and depends on the fracture energy, the elastic modulus and the fracture strength. The material parameters are found to vary with the material orientation of the paper. A method to measure the fracture material parameters is proposed, where only the load and the elongation of the test specimen need to be recorded. Newsprint, kraft paper and paperboard are examined in this investigation.

The cohesive crack model is used as a basis in the formulation of an orthotropic smeared crack constitutive relation to be used in finite element codes. The advantage of this approach is that it provides a theoretical tool in the study of the initiation and stable growth of a localized damage zone or crack in an arbitrary structure subjected to an arbitrary in-plane loading. The model proposed includes a failure criterion and a failure potential. The failure criterion changes its size and shape during the course of fracture softening. The failure potential determines the orientation of the fracture zone and the subsequent crack. The cohesive crack constitutive model is calibrated against one newsprint and one board paper. Simulation results from a single central notch specimen loaded in mode I are compared with experimental results. It was found that the fracture process region is of significant size and that the deviation from an autonomous fracture performance is considerable.

The constitutive model developed is used in the investigation of the behavior of a fiber-based package material, with a punched opening, in the converting process at constant web tension. Finite element simulations of the converting process are made in order to understand how punched paperboard behaves in converting processes. The simulations are compared with experimental results and a reasonable agreement is obtained.

Keywords

Localized damage, Fracture mechanics, Strain softening, Fracture energy, Paper, Elastic modulus, Strength, Experiment, Theory, Finite element, Newsprint, Kraft paper, Paperboard, Package.

Notations

Notations, symbols and functions are defined the first time that they are used in the text. Brief definitions of the most used notations, symbols and functions are listed below in SI- units:

A	Area.	[m^2]
A_f	Positive scalar.	[Pa]
$\hat{A}_f$	Positive scalar.	[Pa]
A_y	Positive scalar.	[Pa^{4k-1}]
a	Crack length.	[m]
$\mathbf{b}$	Crack plane orientation vector.	[m]
C_i	In-plane compression failure strength, $i = 1, 2, 6$.	[Pa]
$\mathbf{D}$	Continuum stiffness matrix.	[Pa]
$\hat{\mathbf{D}}$	Tangential stiffness matrix.	[Pa]
$\mathbf{D}^{ef}$	Elastic-fracture continuum stiffness matrix.	[Pa]
$\hat{\mathbf{D}}^{ef}$	Elastic-fracture tangential stiffness matrix.	[Pa]
$\bar{\mathbf{D}}^{ef}$	Plane stress elastic-fracture continuum stiffness matrix.	[Pa]
$\hat{\bar{\mathbf{D}}}^{ef}$	Plane stress elastic-fracture tangential stiffness matrix.	[Pa]
$\mathbf{D}^{ep}$	Elastic-plastic continuum stiffness matrix.	[Pa]
$\bar{\mathbf{D}}^{ep}$	Plane stress elastic-plastic continuum stiffness matrix.	[Pa]
δ_t	Crack opening displacement (COD).	[m]
E	Young's modulus.	[Pa]
$\boldsymbol{E}^p$	Strain state variable associated to the IPE stress.	[Pa]
$\boldsymbol{\epsilon}$	Strain vector.	[-]
$\bar{\boldsymbol{\epsilon}}$	Strain vector for plane stress condition.	[-]
$\boldsymbol{\epsilon}^e$	Elastic strain vector.	[-]
$\boldsymbol{\epsilon}^f$	Fracture strain vector.	[-]
$\boldsymbol{\epsilon}^p$	Plastic strain vector.	[-]
ϵ_f	Failure strain.	[-]
ϵ_f^f	Internal state variable.	[-]
ϵ_i	Strain components $i = 1, 2, 3, 6$.	[-]
ϵ_N	Mean value of the nucleation-strain normal distribution.	[-]
ϵ_y^p	Internal plastic strain.	[-]
F	Applied load.	[N]
f	Yield criterion.	[Pa^{2k}]
f_N	Volume fraction of nucleating voids.	[-]
G_e	In-plane released elastic elongation energy.	[J/m^2]
G_f	In-plane fracture energy.	[J/m^2]
G_6	In-plane shear modulus.	[Pa]
G'_{f_1}	Fracture energy in mode I.	[J/m^2]
G'_{f_2}	Fracture energy in mode II.	[J/m^2]

γ_{ij}	Softening parameters, $i = 1, 2, 3$ and $j = 1, 2, 3$.	[-]
H_f	General failure modulus.	[Pa]
H_y	General plastic modulus.	[Pa]
J	J-integral.	[J/m^2]
L	Length.	[m]
$L_{critical}$	Paper strip length at immediate failure.	[m]
L_e	Equivalent length.	[m]
L_{stable}	Paper strip length at stable failure.	[m]
k	Integer with values varying from $+1$ to $+\infty$	[-]
λ_f	Smeared crack multiplier.	[-]
λ_y	Plastic multiplier.	[-]
ℓ_{ch}	Characteristic length of the material.	[m]
$\mathbf{N}$	Cohesive modulus matrix.	[N/m]
N	Slope of the uniaxial stress-widening curve.	[N/m]
N_f	Slope of the equibiaxial stress-widening curve.	[N/m]
$\boldsymbol{\mathcal{L}}$	Mapping matrix.	[-]
ν_{ij}	Poisson's ratio, $i = 1, 2, 3$ and $j = 1, 2, 3$.	[-]
P	Equibiaxial failure strength.	[Pa]
p	Parameter in the failure criterion.	[-]
Φ	Failure criterion.	[Pa]
ϕ	Stress function.	[Pa^{2k}]
Ψ	Failure potential.	[Pa]
Q_{12}	Constant in the failure criterion.	[-]
q	Parameter in the failure criterion.	[-]
q_1, q_2, q_3	Parameters in the Gurson yield criterion.	[-]
$\mathbf{R}$	Transformation matrix.	[-]
R	Extent of the process region.	[m]
R_{ii}, R_{12}	Constants in the failure criterion, $i = 1, 2, 6$.	[-]
$\boldsymbol{S}$	IPE stress vector.	[Pa]
S_i	IPE stress components $i = 1, 2, 3, 6$.	[Pa]
S_I, S_{II}, S_{III}	IPE principal deviatoric stress components.	[Pa]
S_{11}, S_{22}	Constants in the failure criterion.	[-]
s_N	Standard deviation of the nucleation-strain normal distribution.	[-]
$\boldsymbol{\sigma}$	Stress vector.	[Pa]
$\bar{\boldsymbol{\sigma}}$	Stress vector for plane stress condition.	[Pa]
$\boldsymbol{\sigma}_T$	Trial stress vector.	[Pa]
σ_e	Effective stress.	[Pa]
σ_i	Stress components $i = 1, 2, 3, 6$.	[Pa]
σ_∞	Remote stress.	[Pa]
σ_ψ	Effective stress potential.	[Pa]
σ_y	Yield stress.	[Pa]

$\mathbf{\Sigma}$	Vector function of stress.	[Pa]
T_i	In-plane tension failure strength, $i = 1, 2, 6$.	[Pa]
θ	Crack plane angle.	[rad]
u	Total elongation.	[m]
ς	Parameter in the failure criterion.	[-]
W	Width of specimen.	[m]
W	Strain energy density.	[J/m^3]
W_e	Elastic strain energy density.	[J/m^3]
W_i	Inelastic strain energy density.	[J/m^3]
$\mathbf{w}$	Crack widening vector.	[m]
w	Crack widening.	[m]
w_{max}	maximal crack widening.	[m]

Contents

1 Introduction **1**
1.1 Background . . . 1
1.2 Aim and scope of the present work . . . 2
1.3 Overview of the work . . . 4
1.3.1 Basic assumptions . . . 4
1.3.2 Summary of the work . . . 5

2 Characterization of uniaxial tensile fracture **9**
2.1 Introduction . . . 9
2.2 Pre-peak stress behavior . . . 9
2.3 Post-peak stress behavior . . . 13
2.4 Model for tensile fracture performance . . . 15
2.5 Analysis of stability at fracture . . . 18
2.6 Intrinsic material length . . . 21

3 Experimental methods and results **23**
3.1 Introduction . . . 23
3.2 Test specimens and procedure . . . 23
3.3 Testing results . . . 25
3.3.1 Stress-strain curves from standard specimens . . . 25
3.3.2 Influence of specimen dimension on the $\sigma(\epsilon)$ curve . . . 28
3.3.3 Orientation of fracture section . . . 28
3.3.4 Stress-widening curves . . . 30
3.3.5 Fracture energy and characteristic length . . . 34
3.3.6 Slope and simplified shape of $\sigma(w)$ curve . . . 35
3.4 Critical and stable length . . . 36
3.5 Proposed method for testing fracture properties . . . 37
3.5.1 Ascending part of the load-elongation curve . . . 38
3.5.2 Descending part of the load-elongation curve . . . 39
3.5.3 Comments . . . 39

4 In-plane constitutive models for paper **41**
4.1 Introduction . . . 41
4.2 In-plane elastic-plastic constitutive model . . . 42

4.2.1 Introduction . . . 42
4.2.2 Plastic constitutive relation . . . 43
4.2.3 The Karafillis-Boyce yield criterion . . . 43
4.2.4 Evolution laws . . . 44
4.2.5 The elastic-plastic continuum stiffness matrix . . . 45
4.2.6 Comments . . . 46
4.3 In-plane elastic-cohesive softening model . . . 47
4.3.1 Introduction . . . 47
4.3.2 In-plane orthotropic smeared crack model . . . 48
4.3.3 Fracture energy concept . . . 50
4.3.4 Stress rate vs. crack widening rate relation . . . 51
4.3.5 The failure criterion . . . 52
4.3.6 Evolution laws . . . 57
4.3.7 The failure potential . . . 58
4.3.8 Continuum stiffness matrix . . . 60
4.3.9 Tangential stiffness matrix . . . 61
4.3.10 Tangential stiffness components . . . 63
4.3.11 Crack Plane . . . 65

5 Numerical calibration 67
5.1 Introduction . . . 67
5.2 Numerical implementation of the models . . . 67
5.3 Calibration of the elastic-plastic model . . . 68
5.3.1 Calibration of the Karafillis-Boyce yield criterion . . . 68
5.3.2 Comparison with experiments . . . 72
5.4 Calibration of the elastic-cohesive model . . . 72
5.4.1 Calibration of the failure criterion . . . 72
5.4.2 Calibration of the failure potential . . . 74
5.4.3 Comparison with experiments . . . 74
5.4.4 Mesh objectivity . . . 77
5.4.5 Restrictions on the mesh . . . 77
5.5 Combination of the KB and ECS models . . . 78
5.5.1 Loading in the CD . . . 79
5.5.2 Loading in the MD . . . 81
5.6 Comments . . . 81

6 Analysis of notch specimen 85
6.1 Introduction . . . 85
6.2 Central cracked sheet in mode I . . . 85
6.3 Experimental observations . . . 86
6.4 Comparison with finite element simulations . . . 89
6.4.1 Comparison with simulations in the MD . . . 89
6.4.2 Comparison with simulations in the CD . . . 96
6.5 Process region ahead of the crack tip . . . 98

6.6 Limit load estimation 100

7 Analysis of perforated opening in a package 103
7.1 Introduction 103
7.2 Calibrations of the constitutive models 104
7.2.1 Calibrations of the metal foil model 104
7.2.2 Calibration of the PE-type model 106
7.2.3 Calibration of the paperboard models 106
7.3 Experiments and simulations of a board in tension 108
7.3.1 Experimental setup 110
7.3.2 Experimental observations 110
7.3.3 Comparison with finite element simulations 111
7.4 Simulation of a package laminate in tension 118

8 Concluding remarks 123
8.1 Summary 123
8.2 Conclusions 125
8.3 Future development 126

Bibliography 129

Chapter 1

Introduction

1.1 Background

The strength of paper under arbitrary loading is of great importance in many industrial applications. Since the early days of industrial use of paper the burst test [97] has been used to characterize paper. Over time, controlled experimental testing has been reported in the literature [29, 79, 89] to be used in the characterization of paper strength at initiation of failure. However, efforts to fully characterize the strength of paper for every stress state by experiments have proven to be both tedious and difficult. These difficulties have led to the development of theoretical approaches that describe the failure envelope of paper in the stress space, with parameters that are easily measured with standard tests. The tests are made on specimens without any pre-existing geometry defects, e.g. pre-existing cracks. Several failure envelopes have been developed, cf. [29, 100]. To fully characterize failure of paper additional information is needed, such as the failure evolution direction and the energy dissipation when a new crack surface is generated. If only the failure envelope in stress space is known, basically only failure of paper in a homogeneous and statically determinate state of stress can be analysed and predicted.

Here a cohesive crack type of approach intended to characterize fracture in paper is used in the formulation of a fracture softening model for paper. The cohesive crack model is characterized by a relation between the descending stress and the crack widening during failure of the paper. The stress-crack widening curve is obtained from tests of uniaxial loaded paper strips without any pre-existing crack. To record a stable descending load-elongation curve, from which the stress-crack widening curve is obtained, the paper strip must be short and the test equipment stiff. The fracture energy needed to separate the fracture surfaces is defined as the area under the stress-crack widening curve.

Cohesive crack models are frequently and successfully used to characterize the fracture in brittle and quasibrittle material such as e.g. concrete [42, 74], fiber-reinforced plastic and laminates [4, 82], wood [35] and wood adhesive joints [105].

Cohesive crack models are fundamentally different from the classical fracture mechanics models, where the theory is based on a critical quantity that controls the

onset of growth of a pre-existing sharp crack, cf. [33, 45, 76]. The critical quantity is expressed by e.g. the stress intensity factor, the energy release rate, the J-integral or the crack opening displacement. The classical fracture mechanics models can in general be expected to give good results if the size of the fracture process region is very small compared to the length of the crack and the ligament. The applicability of cohesive crack models is in several senses more general. The fracture properties of the material are defined in a more modulated manner and there are no presumptions regarding the size (the length) of the fracture region or regarding existence of a crack. One reason why cohesive crack models have become an object for major research and application only in recent decades might be that applied analysis in general requires use of a computer with good capacity for numerical calculations, e.g. by the finite element method.

In the manufacturing and processing of paper the mechanical loading is complex and varying. It may lead to permanent deformations and failure that might or might not be desired. In such loading cases simulation tools can be used as a complement to traditional design processes. The analysis is carried out in order to improve the performance and to reduce time and cost during manufacture, processing and design of existing and newly developed fiber-based materials and packages. Simulation of the manufacture of package materials and packages includes processes such as creasing, perforation, lamination and forming. The creasing and perforation operation of the paperboard is done in order to obtain a distinct form and opening of the package. The lamination process is where the paperboard is laminated together with polymer films and metal foil to give the package material the properties required to preserve the quality of the package product. The forming and product filling process of the package material into a package is done by the package machine.

Simulations of consumer use of packages are a complex issue, since a distinct handling of the packages is not to be found as in the manufacturing process. This is because people handle the packages in different ways and also have different references concerning what is defined as good or bad package performance. However, comparative simulations can be made on packages if a distinct load or deformation on the package is assumed. This gives information on how different packages respond to external loads and will increase the overall understanding of package performance.

In this work the finite element method is used in the simulations, offering the advantage that the load-deformation response of any structures can be simulated for a variety of loadings and for different material properties. No other computer based technique known today offers such complete generality as does the finite element method.

1.2 Aim and scope of the present work

The aim of this work is to develop a fracture mechanical model for simulation of crack initiation and crack growth in paper at in-plane tension. The project has

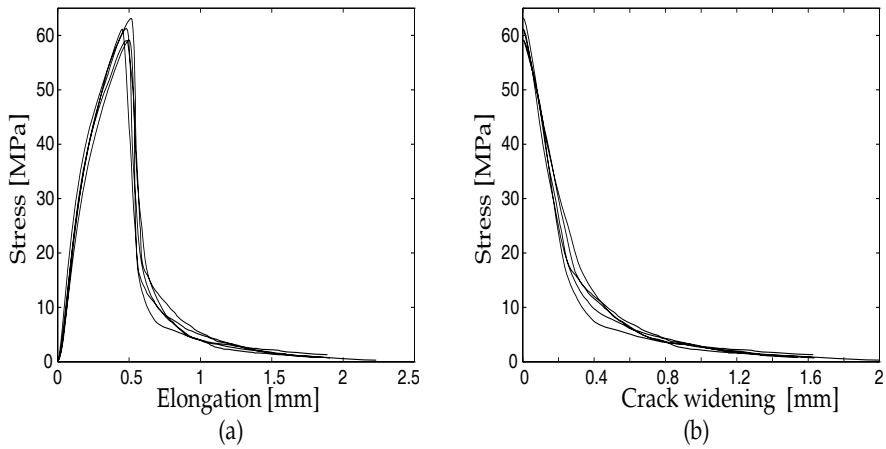

Figure 1.1: *Stress-deformation relations for paperboard 120 g/m^2 strips. (a) Typical stress-elongation curves, loaded in the machine direction. (b) Stress-crack widening curves obtained from the stress-elongation curves.*

included experimental, theoretical and numerical work.

The experimental work sought to study and measure the fracture softening performance and the fracture energy when the failure zone evolves stably in uniaxial tensile tests. The development of a localized failure zone occurs after the tensile strength has been reached, and is characterized by the descending part of the recorded stress-elongation curve, Fig. 1.1(a). The ascending part of the stress-elongation curve in Fig. 1.1(a) gives the stress-strain curve for the paper in a conventional manner, whereas the descending part of the stress-elongation curve in Fig. 1.1(a) gives the stress-crack widening curve for the paper, cf. Fig. 1.1(b). The stress-widening curve reflects the performance of the fracture process region and characterizes the fracture properties of the actual paper. Both the stress-strain curve and the stress-widening curve are assumed to be independent of the geometry of the uniaxial test specimen, i.e. the curves characterize the material behavior of paper at uniaxial tensile loading.

The cohesive crack model is intended to describe the fracture evolution in paper. The cohesive crack model developed in this work includes the primary features at in-plane tension failure of paper, i.e. the anisotropic softening and irreversibility, cf. [93], Fig. 1.2(a). Features which are important but not critical are the decrease in the stiffness during softening, Fig. 1.2(b), and the time dependent behavior. These features are not included in the present study. Moreover, in the present modelling and analysis of tensile failure, the effects of possible yielding or buckling due to large compressive stress are not taken into account.

In the formulation of a constitutive relation for paper, the stress-crack widening curve can be used to characterize the failure of the material. The corresponding

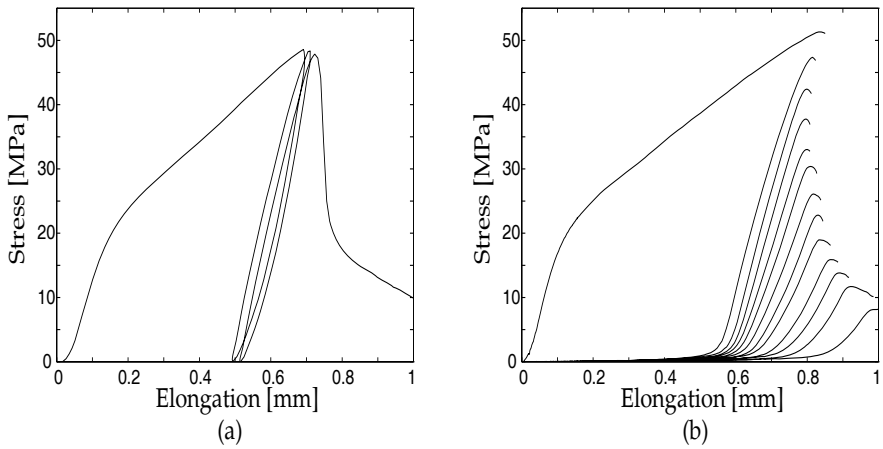

Figure 1.2: *Stress-elongation relations for paperboard 120 g/m^2 strip at loading and reloading. (a) Softening and irreversibility in the cross-machine direction (CD). (b) Reloading stiffness after different magnitude softening in the CD.*

cohesive softening constitutive stress-strain relation has been implemented as a users' material subroutine into the commercial finite element code ABAQUS/Standard[1], in order to be able to make simulations of the initiation and growth of fracture in structures with and without pre-existing cracks and defects due to a variety of loadings and different paper materials. An application example taken from the Tetra Pak company is analysed in order to show the usefulness of the developed cohesive softening model.

1.3 Overview of the work

1.3.1 Basic assumptions

The structure of paper consists in the main of wood fibers linked together fiber-to-fiber into a network, cf. Fig. 1.3. There are conceptually many different models to be used in order to describe the mechanical response of paper. Models are the network, cf. [23, 38, 47, 71], laminate and continuum models, cf. [50, 58, 66, 72, 81, 84, 95]. Figure 1.4 shows the levels of characterization of mechanical properties of paper. In a network model the individual fibers and fiber-to-fiber connections are modelled into a paper sheet. For continuum models it is assumed that a representative volume of fibers and fiber-to-fiber connections can be treated as a continuum. In this work the paper is treated as a homogeneous orthotropic plane stress continuum.

[1] ABAQUS/Standard is a registered trademark of Hibbitt, Karlsson & Sorensen, Inc.

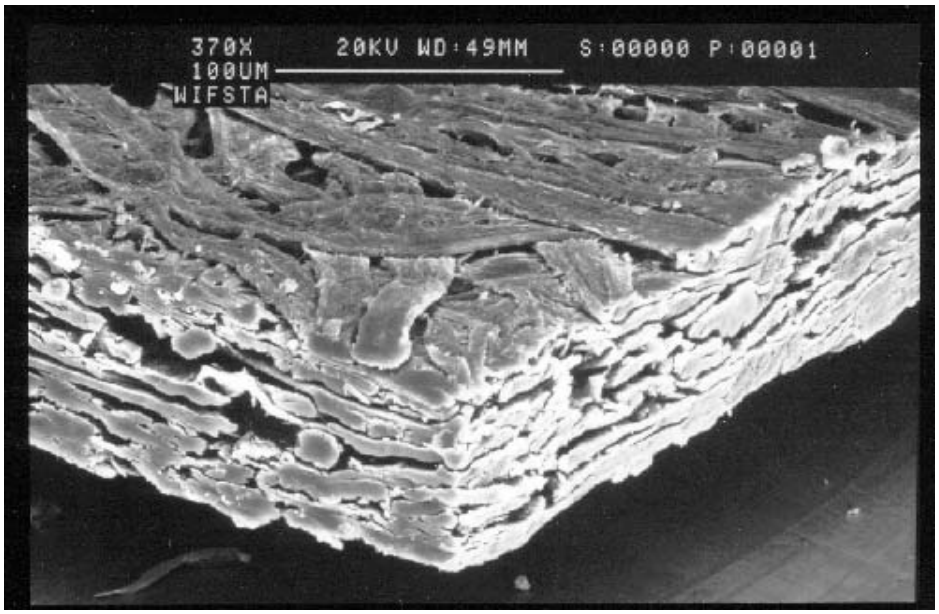

Figure 1.3: *Photo of a paper sheet, from C. Fellers, STFI.*

1.3.2 Summary of the work

Chapter 2 discusses characterization of tensile fracture. A review of the pre-peak stress behavior at uniaxial tension of paper is provided. The post-peak stress behavior is discussed for paper strips short enough to yield a stable descending load-elongation curve. Stable descending load-elongation curves are shown to be transformable into stress-crack widening curves which characterize the failure of paper. Stress-crack widening curves for paper have not been found in the available literature by the author. Chapter 2 concludes by discussing conditions for stable tensile fracture and testing, and by mentioning various measures of intrinsic material length.

In Chapter 3 an experimental method for determination of in-plane tensile fracture properties is proposed, and several experimental results are presented. Illustrative examples of three types of paper have been tested: newsprint, kraft paper and board. To study the test method, tests were made with specimens of various length and width. The results include stress-crack widening curves for tension in the machine direction (MD) and the cross-machine direction (CD). In addition, several directions in between were tested, stress-strain curves were determined, stability of fracture for various specimen lengths studied and material parameters evaluated.

Table 1.1 includeds some key parameters studied experimentally in Chapter 3 for the papers tested in this work, i.e. the fracture energy, the elastic modulus, tensile strength and failure strain. The failure strain is defined as the strain at peak stress. Test methods and results are given in greater detail in Chapters 2 and 3.

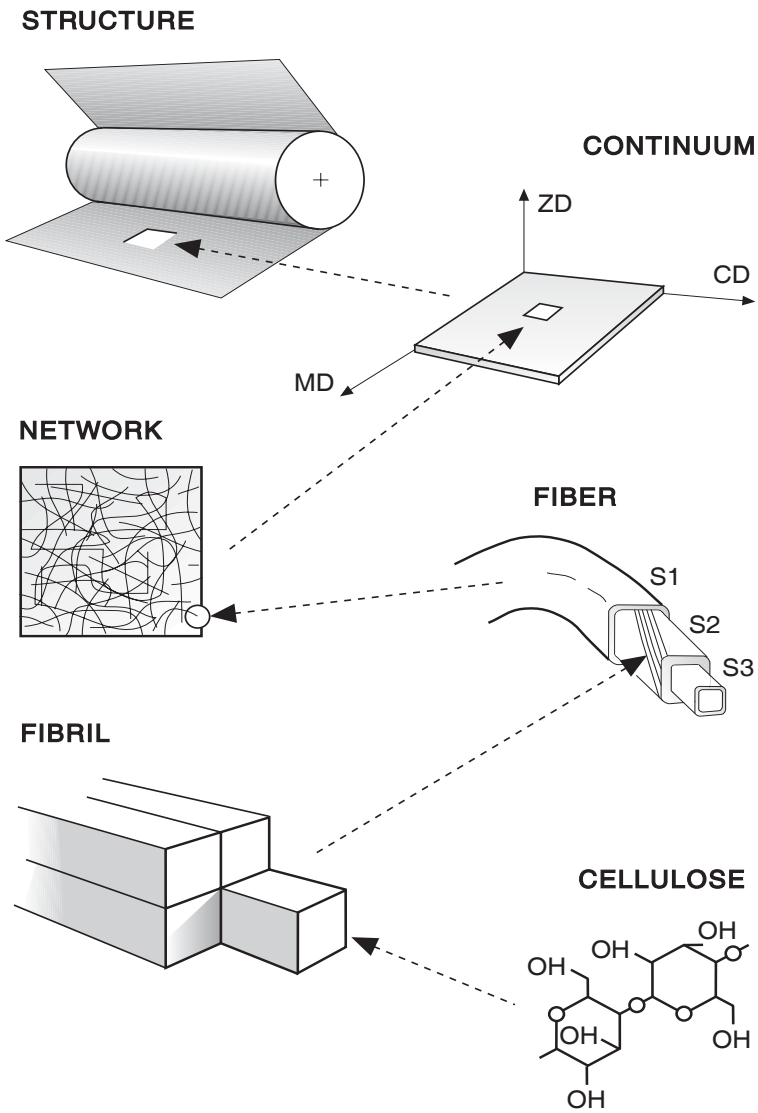

Figure 1.4: *Characterization levels for mechanical properties of paper, after G. A. Baum [6].*

	Newsprint		Kraft paper		Board I		Board II	
Basis weight, g/m^2	45		70		120		240	
Thickness, μm	72		100		154		390	
Density, kg/m^3	643		700		779		620	
	MD	CD	MD	CD	MD	CD	MD	CD
Elastic modulus, MPa	4560	873	3470	2520	6780	3570	5420	1900
Tensile strength, MPa	31.9	10.8	57.3	33.1	57.7	37.4	45.0	15.0
Failure strain, %	0.92	2.8	5.4	6.5	2.6	6.0	1.3	5.1
Fracture energy, kJ/m^2	7.10	4.52	29.0	24.6	17.0	18.5	14.8	14.2

Table 1.1: *Material data for the tested papers (mean values).*

Chapter 4 deals with in-plane constitutive modelling of paper. Following a general introduction, first an elastic-plastic model [50] for the pre-peak stress behavior of paper is briefly reviewed. Then an elastic-cohesive softening constitutive model for paper is proposed to describe the fracture softening post-peak stress behavior. Strain localization during fracture is taken into account through the fracture energy, and intrinsic length measure of the material is given by the stress-crack widening curve. In other respects the model follows the framework of local action elastic-plastic constitutive theory. The proposed model is anisotropic and includes both a failure surface that changes size and shape during the course of fracture, and a failure potential that determines the orientation of the plane of fracture. The initial shape of failure surface can be regarded as a modification of the yield surface reported in [41]. The modified surface takes into account the different failure stress observed in paper in tension and compression. Chapter 4 is completed by derivation of the stiffness matrix for the failure softening material and adjustment of the matrix in order to get good convergence properties during numerical calculations. The numerical procedures follow methods which can be found in the literature, cf. [64, 91, 102].

In Chapter 5, numerical implementation of the models dealt with in Chapter 4 into a commercial finite element code is briefly discussed. Then the models are calibrated to experimental data. The calibration of the present fracture softening model is presented and discussed in detail. In this context objectivity and restrictions in relation to finite element mesh are also studied. Moreover, restrictions when combining the present fracture model with an elastic-plastic model are studied.

Chapter 6 concerns the analysis of a rectangular sheet containing a central crack. Numerical simulations with the elastic-cohesive softening model are made and the results are compared with experimental observation.

In Chapter 7 a paperboard web with a punched opening in the converting process is studied. Both experimental and numerical simulations are used in the analysis of the punched web. The example is taken from Tetra Pak.

Concluding remarks, discussions and further research needs are found in Chapter 8.

Chapter 2

Characterization of uniaxial tensile fracture

2.1 Introduction

The characterization of tensile fracture is here investigated for uniaxial in-plane loading. The pre-peak stress behavior of paper is reviewed in Section 2.2, cf. [3, 23, 27, 46, 58, 71, 72], and the post-peak stress behavior of paper is discussed in detail in Section 2.3. Section 2.4 describes a model for tensile fracture performance. Stability at fracture and intrinsic material length measures of paper are discussed in Sections 2.5 and 2.6, respectively.

It has been reported in the literature that the tension failure mechanism in paper is related to the length of uniaxially tested paper strips, cf. [19, 21, 32, 43, 93]. If the paper strip is sufficiently long the paper will rupture suddenly, and if the paper strip is shortened the paper will exhibit a "non-immediate" rupture, [32, 43]. Further shortening of the paper strip will give a stable evolution of the failure zone [19, 21].

The experimental observations reported in the literature [19, 21, 32, 43, 93] form one of the bases for the modelling of uniaxial tensile fracture of paper discussed in this chapter. The discussion of the model has its theoretical background in recent decades of research in the area of strain instability, strain localization and fracture softening during tension failure, e.g. [17, 42, 74].

It is assumed that the in-plane stresses and strains are related to the three principal axes of the material. The 1-axis coincides with the machine direction (MD) and the 2-axis coincides with the cross-machine direction (CD), whereas the out-of-plane stresses and strains are related to the 3-axis which coincides with the thickness direction (ZD) of the paper.

2.2 Pre-peak stress behavior

Load-elongation curves for strips of paper in approximate homogenous tension in the MD are shown in Fig. 2.1. The curves in Fig. 2.1 are the results from two

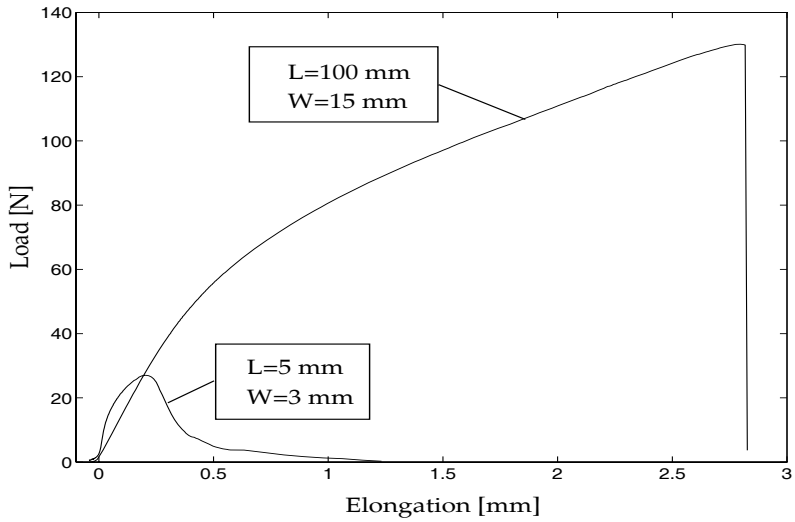

Figure 2.1: *Load-elongation curves in the MD (paperboard 120 g/m^2).*

paperboard 120 g/m^2 strips, from which one of the curves has been cut 3 mm wide and is 5 mm long between the clamped jaws, and the other one has been cut 15 mm wide and is 100 mm long between the clamped jaws. In Fig. 2.1 L is defined as the length between the clamped jaws, W is the width of the specimen, F is the load and u is the elongation of the paper strip in the loading direction. The curve denoted $L = 5$ mm shows a stable descending part, i.e. stable fracture, whereas the curve denoted $L = 100$ mm shows no descending part at all, i.e. exhibits immediate fracture.

The ascending part of the load-elongation curve for paper strips can be approximately regarded as self-similar, if the test is made under a uniaxial state, cf. [46, 69, 70], i.e. the ascending load-elongation curves are transformed into a single stress-strain curve. The stress, σ, is defined as the load, F, divided by the cross section area, A, and the strain, ϵ, is defined as the elongation, u, divided by the paper strip length, L. In Fig. 2.2 the ascending load-elongation curves in Fig. 2.1 are transformed into stress-strain curves, and it is shown that the curves are approximately transformed into a single stress-strain curve. The disparity between the curves in Fig. 2.2, which starts approximately at strain 1.5%, is discussed in Section 3.3.2. The deviation at very small strain is due to the test equipment and is not typical for the performance of the paper.

From the stress-strain curve, which is assumed to uniquely define the ascending part of the load-elongation response for the paper at all strip lengths, material parameters are defined. The elastic modulus in Fig. 2.3 is denoted by E and the stress and strain at peak stress are called the fracture stress, σ_f, and failure strain,

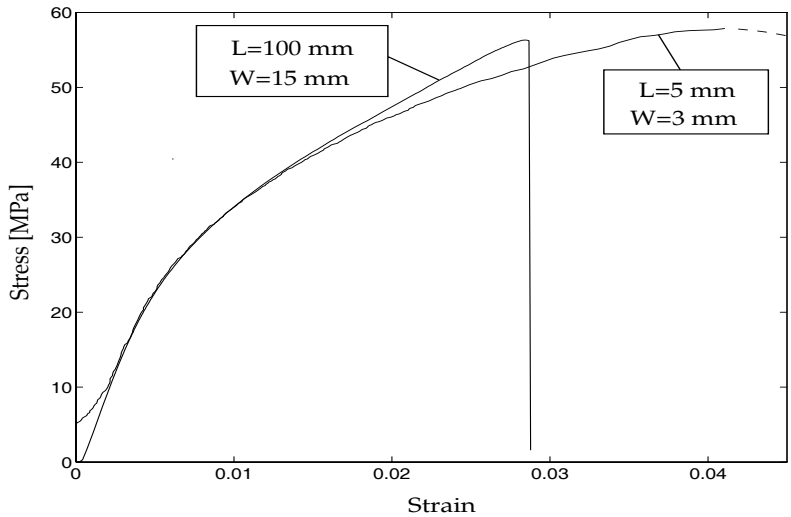

Figure 2.2: *Stress-strain curves obtained from Fig. 2.1 (paperboard 120 g/m^2).*

ϵ_f. The strain energy density, W, at the failure strain, ϵ_f, is defined as the area under the stress-strain curve in Fig. 2.3, i.e. as

$$\mathrm{W} = \int_0^{\epsilon_f} \sigma(\epsilon) d\epsilon \tag{2.1}$$

The uniaxial tensile stress-strain behavior for a paperboard when alternately loaded and unloaded and measured in the CD is shown in Fig. 2.4. The results indicate that paper shows closed hysteresis loops beyond the linear elastic part of the stress-strain curve due to unloading-reverse loading [3, 93]. The occurrence of the closed hysteresis loops, called the Masing effect [59], indicates that paper before peak stress behaves as an elastic-plastic material with plastic deformation at unloading. So, the strain energy density, W, consists of the elastic strain energy density, W_e, and the inelastic strain energy density, W_i, i.e. $\mathrm{W} = \mathrm{W}_e + \mathrm{W}_i$, (see Fig. 2.3). The elastic strain energy density is recovered during relaxation, for example at failure, whereas the inelastic strain energy dissipates, due to fiber reorientation etc. The relaxed elastic strain energy density, W_e, in the figure is the dashed area, and the inelastic strain energy density, W_i, is the area under the stress-strain curve subtracted from the dashed area.

Figure 2.5 shows an example of the in-plane uniaxial tensile stress-strain behavior of paper reported in the literature, [73]. The paperboard 240 g/m^2 samples were cut 50 mm wide and long enough to be clamped between jaws 210 mm apart. The tests were performed at an average humidity of 50 $\pm$ 5 %. The curves in Fig. 2.5 are due to tension loading in the 1- and 2-directions, i.e. $\sigma_1(\epsilon_1)$, $\sigma_1(\epsilon_2)$, $\sigma_2(\epsilon_1)$ and

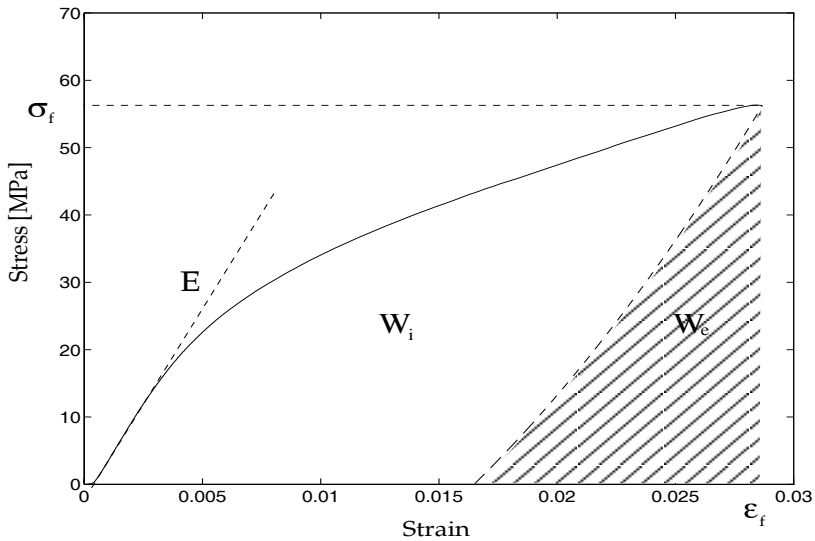

Figure 2.3: *The stress-strain curve is obtained from the ascending load-elongation curves in Fig. 2.1.*

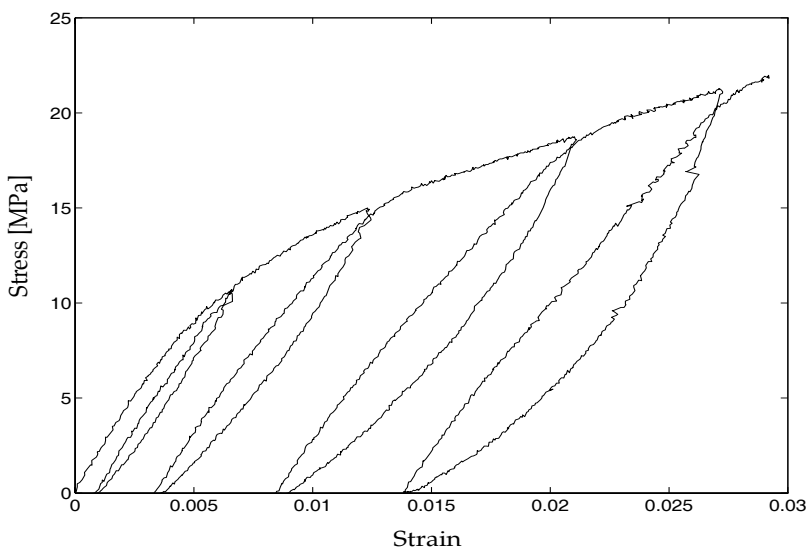

Figure 2.4: *Load-reloading applied in the CD (paperboard 240 g/m^2) [73].*

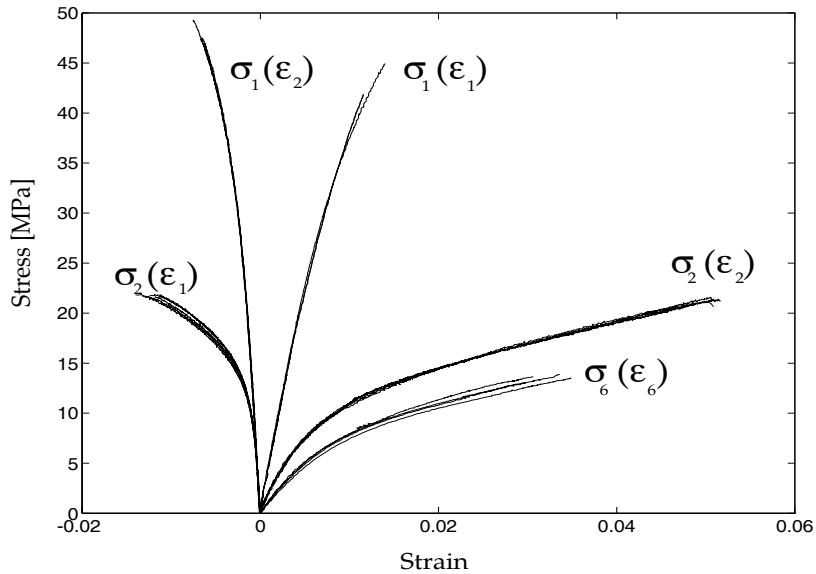

Figure 2.5: *Stress-strain curves due to tension and shear loading with reference to the 1- and 2-direction [73].*

$\sigma_2(\epsilon_2)$, where σ_1 and σ_2 are the stresses and ϵ_1 and ϵ_2 are the strains in the 1- and 2-direction, respectively. The shear stress-shear strain relation, $\sigma_6(\epsilon_6)$, is also shown in Fig. 2.5. From the curves in Fig. 2.5 it is noted, when the properties in the 1- and 2-directions are compared, that the material shows an anisotropic behavior. The ratios between the moduli and the yield stress in the 1- and 2-directions are larger than a factor of 2. Furthermore the σ_1-ϵ_2 curve and the σ_2-ϵ_1 curve are equal only as long as the material is elastic, i.e. the symmetry properties are violated when the material becomes plastic. The curves provide the data needed to describe the in-plane elastic stiffness properties of tension and shear (tensile moduli and Poisson's ratios). They also serve to describe the plastic properties once the material has yielded (the yield stresses, strain hardening and plastic lateral straining), [50].

2.3 Post-peak stress behavior

It has been reported [19, 21, 32, 43, 93] that for a sufficiently long paper strip the paper will rupture suddenly, as is shown in Fig. 2.1 for the paperboard 120 g/m^2 strip of a length of L=100 mm. If, however, the paper strip is shortened it will exhibit a semi-immediate rupture (or a semi-stable) fracture. Further shortening will give a stable evolution of the fracture. Figure 2.1 shows the load-elongation

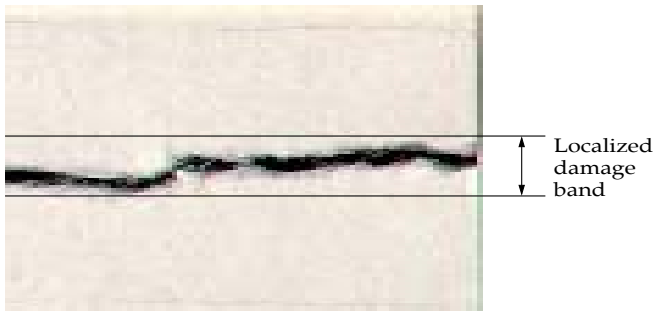

Figure 2.6: *Photo of a damaged paper strip, L=150 mm.*

curve for the stable fracture, obtained from a uniaxial loaded paper strip of a length of L=5 mm and a width of W=3 mm. We see that both the load-elongation curves in Fig. 2.1 consist of a stable ascending part, whereas the descending part behaves as instable or stable depending on the strip length.

If paper strips short enough to give stable descending load-elongation curves are elongated beyond the instant when $\epsilon = \epsilon_f$ and $\sigma = \sigma_f$ it is then assumed that further deformation of the paper will be localized into a narrow zone, Fig. 2.6, in a manner similar to that reported for materials like concrete, [42, 74]. The extension along the paper strip of this damage or fracture process zone is assumed to be independent of the length of the paper strip, cf. Section 3.3.4. It is furthermore assumed that the localized deformation is caused by both plastic and damage softening, until the paper strip has formed an almost free surface throughout its width. The paper strip is now held together only through single fiber bridges. This assumption is supported by displacement controlled load-reloading of a paperboard 120 g/m^2 strip where we see that the initial reloading elastic stiffness decreases continuously as the localized damage growth increases, cf. Fig. 2.7. Figure 2.7(a) shows the softening and irreversibility; Fig. 2.7(b) shows the decrease in the stiffness and failure stress during softening. The curves shown in Fig. 2.7(b) are the reloading curves at different magnitudes of softening and are obtained by unloading at prescribed elongations after the failure load has been reached. In Fig. 2.7(b) it is seen that the first reloading curve has approximately the same stiffness as the initial stiffness, i.e. initially dominates the plastic softening effects. From Fig. 2.7(b) it is also seen that the failure stress at reloading of the curves is less than the stress at unloading, i.e. occurrence of damage in the localized band during an unloading-reloading cycle is evident. In the construction of the constitutive model in Chapter 4 it is assumed that the localized deformation is caused only by plastic softening.

From previous studies, cf. [48, 70, 80], it is shown that the damage evolution in paper is predominantly caused by bond failure. To completely separate the paper strip, now held together through single fiber bridges, a certain amount of work is needed in order to pull out these fibers until the paper strip has been separated into two paper strips [12].

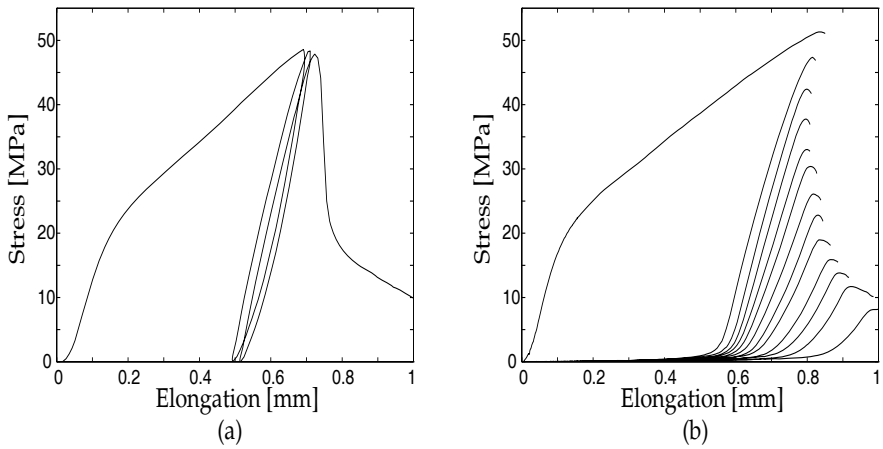

Figure 2.7: *Stress-elongation relations for paperboard 120 g/m^2 strip at loading and reloading. (a) Softening and irreversibility in the CD. (b) Reloading stiffness after different magnitudes of softening in the CD.*

The assumed fracture mechanism indicates that the measured elongation does not correspond to a homogenous deformation in the paper strip. Instead, the total elongation of the paper strip, u, can be thought of as the sum of the local deformation in the fracturing damage band and a uniform strain outside the damage band. The strain outside the damage band decreases during the course of fracture due to the decrease in stress. Accordingly, fracture can be assumed to take place in the narrow band, Fig. 2.6, while the other part of the paper strip is unloading. On the analogy of this description of failure kinematics, the recorded stress can be thought of as a cohesive stress acting across the narrow fracture band, cf. [5].

2.4 Model for tensile fracture performance

The stable descending load-elongation curves, like the one shown in Fig. 2.1, were found by Hillerborg et al., [42], to be transformable into a single cohesive stress-widening curve, Fig. 2.8, which defines the constitutive properties of the material during tensile fracture. The widening of the damage band, w, is defined as the total elongation, u, subtracted from the uniform elongation of the relaxing undamaged part of the paper strip, $u_r = \epsilon L$, i.e.

$$w = u - \epsilon L \tag{2.2}$$

see Fig. 2.9 and Fig. 2.10. w is accordingly the additional fracture deformation within the damage band. We know that the stress, σ, and the strain, ϵ, are determined by the unloading performance of the material, and that load-unloading tests

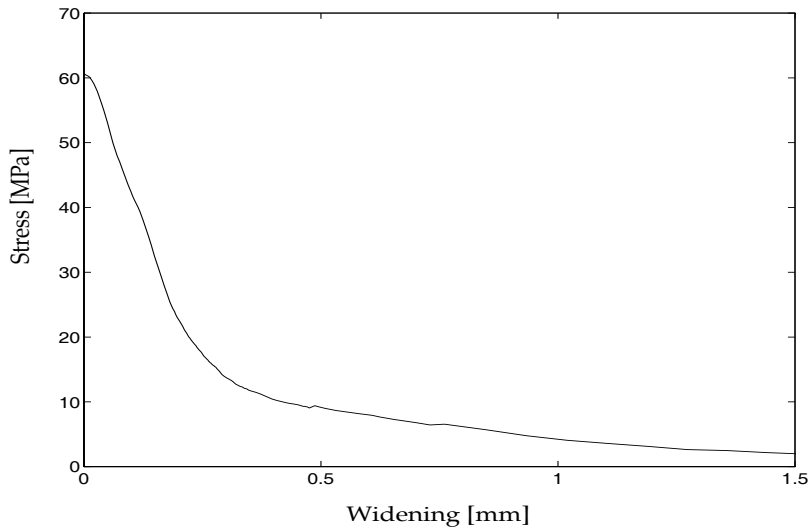

Figure 2.8: *The stress-widening curve, $\sigma(w)$, is obtained from a paperboard 120 g/m^2 strip (W=15 mm and L=5 mm). The area under the curve is the fracture energy, G_f.*

of paper indicate that the material properties before start of fracture are elastic-plastic, [3], see Fig. 2.3. In that case and under the assumption that during the entire unloading path the slope is equal to the elastic modulus, E, then the uniform strain during fracture is

$$\epsilon = \epsilon_f - \frac{(\sigma_f - \sigma)}{E} \tag{2.3}$$

Insertion of Eq. (2.3) into Eq. (2.2) gives the widening of the damage band, w, as

$$w = u - \epsilon_f L + \frac{(\sigma_f - \sigma)}{E} L \tag{2.4}$$

If this widening of the damage band in Eq. (2.4) and the stress, $\sigma = F/A$, are applied to the short paper strip in Fig. 2.1, then the load-elongation curve is transformed into a stress-widening curve as shown in Fig. 2.8. The stress-widening curve characterizes the fracture performance of the narrow damage band and is assumed to be the same for all paper strip lengths.

The fracture energy, G_f, is defined as the area under the cohesive stress-widening curve. Accordingly, the fracture energy can phenomenologically be described as a function of the cohesive stress, $\sigma(w)$, and the widening of the localized fracture band, cf. [42], as

$$G_f = \int_0^{w_{max}} \sigma(w) dw \tag{2.5}$$

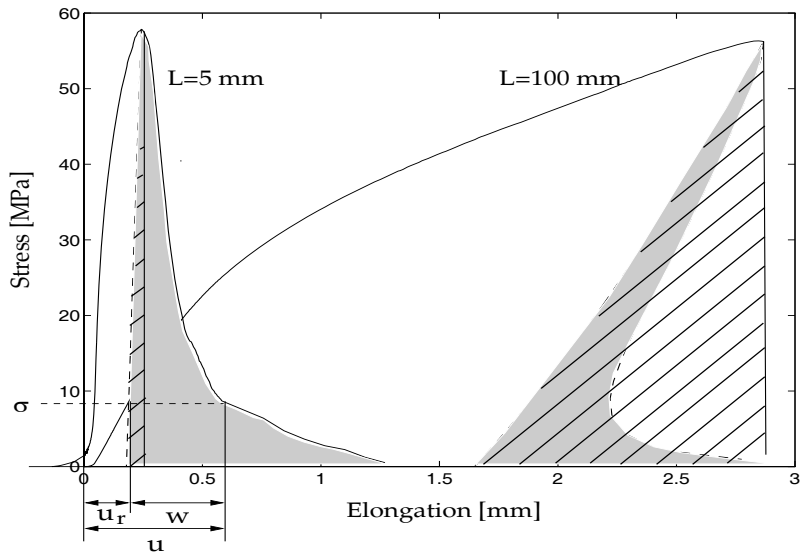

Figure 2.9: *The stress-elongation curves for the long and short paper strips.*

where w_{max} is the crack widening at a completely separated fracture surface. If the specimen length is larger than the width of the fracture zone and if the paper is assumed to be homogenous, then it may be expected that the fracture dissipation, G_f, (the grey area in Fig. 2.9) becomes independent of the specimen length. The width of the fracture zone can be assumed to be about the same as or slightly less than, the fiber length. So, the specimen must at least be some millimetres long.

The observation above that the elastic strain energy density, W_e, and the fracture energy, G_f, are approximately self-similar explains the observed behavior, i.e. that the descending load-elongation curves are dependent on the length of the uniaxial tested paper strip, cf. [19, 21, 32, 43, 93]. For long paper strips the incremental released elastic elongation energy (per unit cross section area), i.e. $\Delta G_e = \Delta \mathrm{W}_e L$, during the entire course of the failure is greater than the incremental fracture energy, ΔG_f, i.e. $\Delta G_e > \Delta G_f$. This is illustrated in Fig. 2.9 for the L=100 mm long paper strip, where the released elastic elongation energy, the dashed area in Fig. 2.9, is greater than the fracture energy, the grey area in Fig. 2.9. Thus the released elastic elongation energy alone is sufficient to completely separate the material in an immediate and brittle fashion. For paper strips of a length less than the length at which the strip exhibits immediate rupture, fracture is partly stable and partly unstable. The reason for this is that the incremental released elastic elongation energy, ΔG_e, during the course of failure becomes either greater or less than the incremental fracture energy, ΔG_f. Further shortening of the paper strip length will eventually cause the stress-elongation curve to show a stable descending branch with

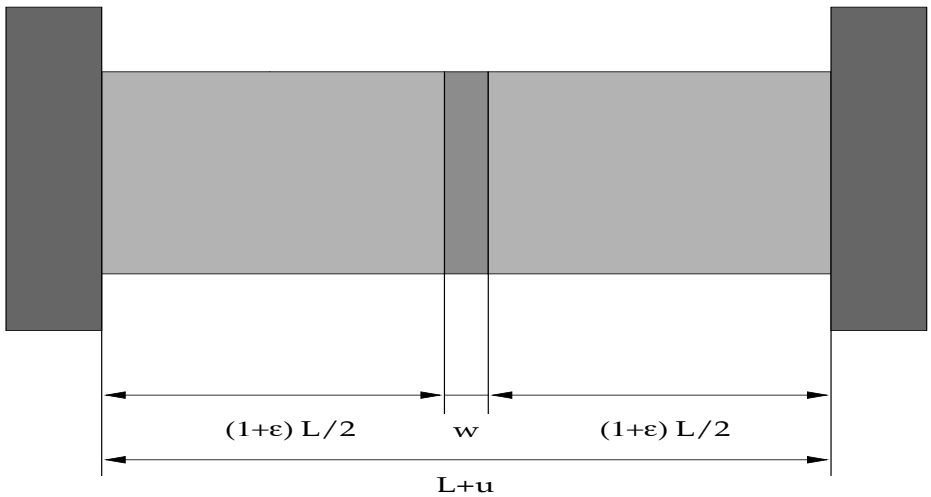

Figure 2.10: *The paper strip of length L held between the grips at the elongation u.*

no immediate fall of the stress at all [19, 21, 43]. This is shown in Fig. 2.9 for the L=5 mm long paper strip, where the incremental released elastic elongation energy, ΔG_e, is always less than the incremental fracture energy, ΔG_f, during the entire course of failure, i.e. $\Delta G_e < \Delta G_f$. Thus additional energy must be supplied to create further damage and, subsequently, to completely separate the material.

2.5 Analysis of stability at fracture

The critical length, $L_{critical}$, is defined as the shortest length of the paper strip for which the load-elongation curve (in stroke-controlled testing by a stiff testing device) immediately falls from a point of instability to zero load [32]. A paper strip of a length greater than the critical length exhibits rupture in a brittle fashion, cf. Fig. 2.1. If instability occurs it is almost always immediately after the instant of maximum load. The length of the longest paper strips which cause the load-elongation curve to show a stable descending branch with no immediate fall of the load [19, 21, 43], cf. Fig. 2.1, is the definition for the stable length, L_{stable}, of the paper strip. The case when $L_{critical} > L > L_{stable}$ implies that a sudden drop of the load occurs from a point of instability to a lower load, not equal to zero.

The length L_{stable} can be obtained from an analysis of the model of the fracture of the paper strip in Fig. 2.10, [74]. The prescribed total elongation, u, in the figure is the sum of the uniform elongation of the relaxing undamaged part, ϵL, and the widening of the damage band, w, cf. [74], i.e.

$$u = \epsilon L + w \tag{2.6}$$

The uniform elongation of the relaxing undamaged part, $\epsilon(\sigma)L$, is assumed to be the sum of the relaxing elastic part, $\epsilon^e(\sigma)L$, and the constant plastic part, $\epsilon^p L$, i.e. $\epsilon(\sigma)L = (\epsilon^e(\sigma) + \epsilon^p)L$. Insertion into Eq. (2.6) gives

$$u = (\epsilon^e(\sigma) + \epsilon^p)\, L + w(\sigma) \tag{2.7}$$

At instability a virtual change in the load is less then zero, i.e. $\delta F < 0$ and a virtual change in the elongation is equal to zero, i.e. $\delta u = 0$. So, a virtual change of Eq. (2.7) gives

$$\delta u = \frac{\partial \epsilon^e(\sigma) L}{\partial F}\delta F + \frac{\partial w(\sigma)}{\partial F}\delta F = 0 \tag{2.8}$$

Insertion of $\delta F = \delta\sigma A$ (the cross section area, A, is assumed to be constant) into Eq. (2.8) gives

$$\left\{ \frac{\partial \epsilon^e(\sigma)}{\partial \sigma} L + \frac{\partial w(\sigma)}{\partial \sigma} \right\} \delta\sigma = 0 \tag{2.9}$$

Since $\delta F = \delta\sigma A < 0$ and $A > 0$, we obtain

$$\frac{\partial \epsilon^e(\sigma)}{\partial \sigma} L + \frac{\partial w(\sigma)}{\partial \sigma} = 0 \tag{2.10}$$

The stress-elastic strain curve in Fig. 2.3 is assumed to be linear during the relaxing of the undamaged part of the strip, i.e.

$$\delta\sigma = \frac{\partial \sigma}{\partial \epsilon^e}\delta\epsilon^e = E\delta\epsilon^e \tag{2.11}$$

The cohesive stress-widening curve, $\sigma(w)$, with its typical form is shown in Fig. 2.11. From the curve shape in Fig. 2.11 it is clear that the σ-w relation can be represented by a monotonous decreasing function for which the slope is defined as

$$\delta\sigma = \frac{\partial \sigma}{\partial w}\delta w = -N(w)\delta w, \qquad 0 < w \leq w_{max} \tag{2.12}$$

After insertion of Eqs. (2.11) and (2.12) into Eq. (2.10) and some rearrangements, the strip length at instability is given as

$$L = \frac{E}{N(w)} \tag{2.13}$$

The strip length L_{stable} is determined by the steepest part of the $\sigma(w)$ curve, i.e. when $N(w) = N_{max}$, cf. Fig. 2.11. This results in stable stress-elongation curves being recorded if the length of the paper, L, is less than or equal to

$$L_{stable} = \frac{E}{N_{max}} \tag{2.14}$$

For materials with typical $\sigma(w)$ performance as shown in Fig. 2.11, it is often convenient and reasonable to make a straight line approximation of the curve by

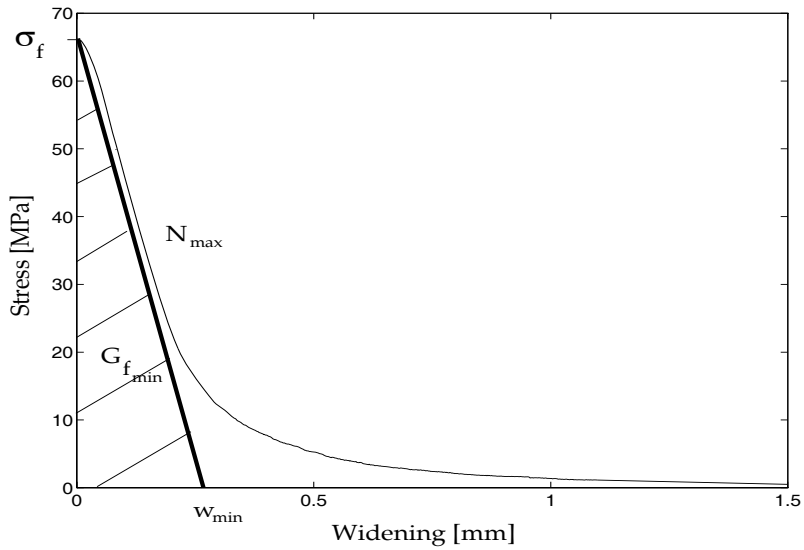

Figure 2.11: *Stress-widening curve obtained from a paperboard 120 g/m^2 strip (W=15 mm and L=5 mm)*

means of the peak stress σ_f and the steepest part of the $\sigma(w)$-curve as illustrated in Fig. 2.11. The corresponding zero stress deformation value is denoted w_{min} and the corresponding fracture energy is

$$G_{f_{min}} = \frac{1}{2}\sigma_f w_{min} = \frac{1}{2}\sigma_f^2 \frac{1}{N_{max}} \tag{2.15}$$

Insertion of Eq. (2.15) into Eq. (2.14) gives

$$L_{stable} = 2\left(\frac{G_{f_{min}}}{G_f}\right)\frac{EG_f}{\sigma_f^2} \tag{2.16}$$

Poor stiffness of the loading equipment may significantly reduce the shortest strip length that can be used. Normally the load cell is by far the most flexible part of loading equipment. The stiffness of the equipment can be assumed to equal the stiffness of the load cell, $F/K_{loadcell}$. If the load cell elongation, $F/K_{loadcell}$ is included in Equation (2.6), then the total prescribed elongation becomes,

$$u = \epsilon L + w + \frac{F}{K_{loadcell}} \tag{2.17}$$

A similar derivation as above gives the stable length,

$$L_{stable} = 2\left(\frac{G_{f_{min}}}{G_f}\right)\frac{EG_f}{\sigma_f^2} - \frac{EA}{K_{loadcell}} \tag{2.18}$$

Comparison between Eq. (2.16) and Eq. (2.18) shows that the stable strip length, L_{stable}, during testing is dependent on the load cell stiffness, $K_{loadcell}$, and on the specimen area, A.

2.6 Intrinsic material length

Hillerborg et al., [42], have shown that it is possible to find a material parameter of the dimension length, called the intrinsic or characteristic length of the material, ℓ_{ch}. This material parameter is found from the fracture energy, G_f, the failure strength, σ_f and the elastic moduli E, as [42],

$$\ell_{ch} = \frac{EG_f}{\sigma_f^2} \tag{2.19}$$

A fracture mechanics concept is here used to show how an intrinsic material length parameter can be found, expressed as in Eq. (2.19). The Barenblatt-Dugdale crack model is applied to a crack of the length $2a$ in an infinite body which is loaded with a uniform remote stress, σ_∞, under plane stress condition, cf. [76]. In the Barenblatt-Dugdale crack model the stress-widening curve in Eq. (2.12) is a slope which approaches zero, i.e. $N \to +0$. The fracture energy dissipation to the crack tip is measured by the J-integral, [76]. The extent of the yielding zone ahead of the crack tip at the fully developed process region for plane stress condition is (at small-scale yielding), [76],

$$\frac{\pi}{8}\frac{EJ_c}{\sigma_f^2} \tag{2.20}$$

where J_c is the J-integral at the fully developed process region. Comparison of the expression for the maximal extent of the yielding zone ahead of the crack tip in Eq. (2.20) with the characteristic length in Eq. (2.19) shows that a study of the fracture process zone at the tip of a crack results in the same kind of intrinsic length parameter as the damage band model or cohesive crack model discussed above.

From linear elastic fracture mechanics the following characteristic length is sometimes used

$$\left(\frac{K_c}{\sigma_f}\right)^2 \tag{2.21}$$

for normalization of theoretical calculation with respect to the specimen's absolute length and the absolute length of the crack. In Eq. (2.21) K_c is the stress intensity factor at failure. The characteristic length in Eq. (2.21) is in analogy with the length measure in Eq. (2.19) and Eq. (2.20).

Chapter 3

Experimental methods and results

3.1 Introduction

Experimental methods and results are used in this chapter to show the characterization of tensile fracture discussed in Chapter 2. A test method is developed for stable descending load-elongation curves in Section 3.2. The testing results are presented and discussed in Section 3.3. The critical and stable length of paper is discussed in Section 3.4. A test method is proposed for characterization of tensile fracture properties of paper in Section 3.5.

The papers used in the tests were newsprint 45 g/m^2, kraft paper 70 g/m^2 and paperboard 120 g/m^2, cf. Table 1.1. The tests were made at a relative humidity of $50 \pm 2\%$ and at a temperature of $23 \pm 1°$ C.

3.2 Test specimens and procedure

The tensile test procedure used here for obtaining the ascending part of the load-elongation curve is a modification of the Tappi official test method, T 494 os-70 [98]. From each test unit of the sample, at least 5 test specimens were cut in each principal direction, and in three directions, equally divided by 22.5 degrees, between the principal directions. All specimens were 15 mm wide with parallel sides, and long enough to be clamped in jaws 150 mm apart. For the 120 g/m^2 paperboard, 3 mm wide specimens with parallel sides and long enough to be clamped in jaws 15 mm apart were also tested in the MD. The constant rate of elongation for a 150 mm test span is 7.5 mm/min, and for a 15 mm test span, 0.75 mm/min. Note that in the T 494 os-70 standard there are 10 specimens in each test unit, and the constant rate of elongation for a 100 mm test span is 12.5 ± 2.5 mm/min. However, the specimen geometry with the 150 mm test span is within the permitted modification of the T 494 os-70 standard.

The tensile test procedure used for obtaining the descending part of the load-elongation curve is here the same as for the ascending part, with the exception that the specimen length between the jaws is less than the stable paper strip length, cf.

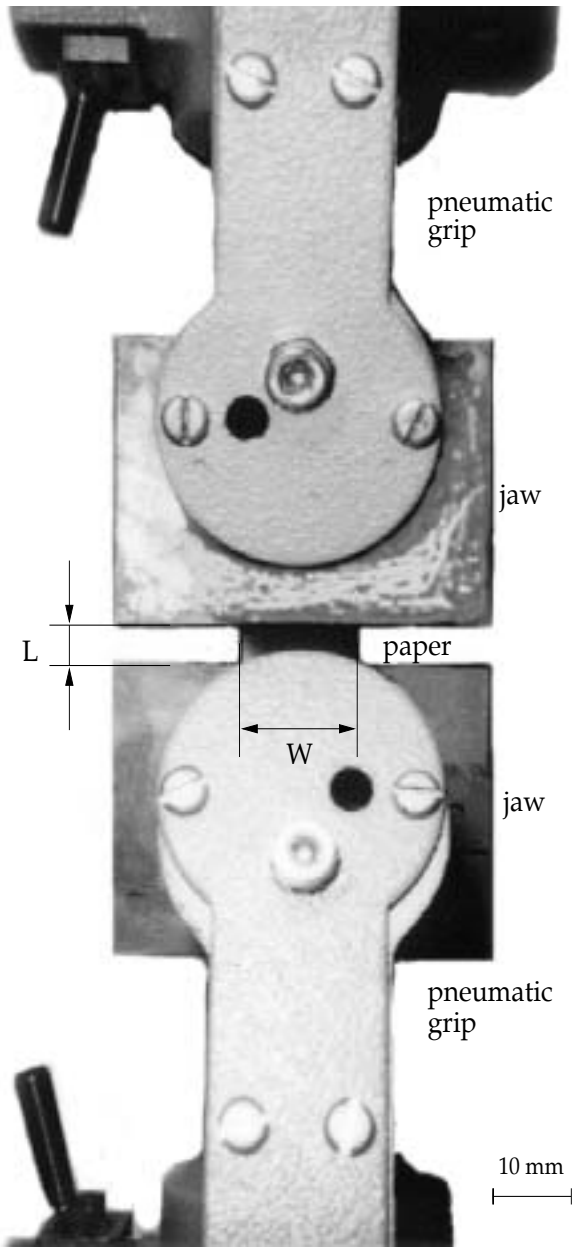

Figure 3.1: *The experimental setup with the specimen held by pneumatic grips.*

	Newsprint 45 g/m^2		Kraft paper 70 g/m^2		Paperboard 120 g/m^2	
φ	σ_f [MPa]	E [GPa]	σ_f [MPa]	E [GPa]	σ_f [MPa]	E [GPa]
0°	31.9 ± 3.6	$4.56 \pm .78$	57.3 ± 3.1	$3.47 \pm .32$	57.7 ± 1.7	$6.78 \pm .19$
22.5°	23.6 ± 2.3	$2.98 \pm .18$	49.5 ± 1.7	$3.58 \pm .17$	53.6 ± 2.3	$6.03 \pm .43$
45°	15.4 ± 0.2	$1.48 \pm .09$	41.0 ± 2.3	$3.23 \pm .19$	42.6 ± 0.9	$4.72 \pm .31$
67.5°	11.4 ± 1.0	$.931 \pm .07$	37.7 ± 1.6	$2.84 \pm .27$	45.3 ± 0.9	$4.50 \pm .12$
90°	10.8 ± 0.4	$.872 \pm .02$	33.1 ± 2.0	$2.52 \pm .10$	37.4 ± 1.6	$3.57 \pm .07$

Table 3.1: *Material data for the tested papers, mean values ± standard deviation.*

Section 2.5. From each test unit of the sample, at least 5 test specimens were cut in each principal direction, and in eight directions, equally divided by 10 degrees, between the principal directions. All specimens were 15 mm wide, with parallel sides, and long enough to be clamped in jaws 5 mm apart. For the 120 g/m^2 paperboard, 3 mm and 15 mm wide specimens with parallel sides and long enough to be clamped in jaws 5 mm and 15 mm apart, respectively, were also tested in the MD. The constant rate of elongation for a test span L is adjusted to give the same strain rate, $0.05L$ mm/min. Figure 3.1 shows the experimental setup with the specimen.

The uniaxial tests were carried out with an Instron universal testing instrument (model 4502) including a 100 N and a 10 kN tension-compression load cell. The 100 N load cell stiffness was measured to $K_{loadcell} = 0.674$ MN/m (obtained for the load interval of 0-10 N) and the 10 kN load cell stiffness was measured to $K_{loadcell} = 1.12$ MN/m (obtained for the load interval of 0-150 N). The 100 N load cell was only used for the 3 mm wide samples. The paper strip samples were held by pneumatic vice-action grips (1 kN capacity) between two parallel textured jaw faces, cf. Fig. 3.1. This type of grip has the advantage of allowing accurate fixation without any sliding, as well as rapid and easy loading of the paper strips. The uniaxial load-elongation curves were sampled into a PC. The load was recorded by the load cell and the elongation by the moving crosshead.

3.3 Testing results

3.3.1 Stress-strain curves from standard specimens

Paper strips long enough to suddenly rupture at maximal load are here tested, i.e. $L > L_{critical}$. The papers used in the test are newsprint 45 g/m^2, kraft paper 70 g/m^2 and paperboard 120 g/m^2. All papers are cut in 0, 22.5, 45, 67.5 and 90 degrees with respect to the MD. The MD refers to the $\varphi = 0°$ angle and accordingly the CD refers to the $\varphi = 90°$ angle. For each paper and for each direction at least five nominally equal tests are made.

Table 3.1 shows the material data obtained from the test for failure stress, σ_f, and the elastic modulus, E, as mean values ± standard deviation. Here, the failure

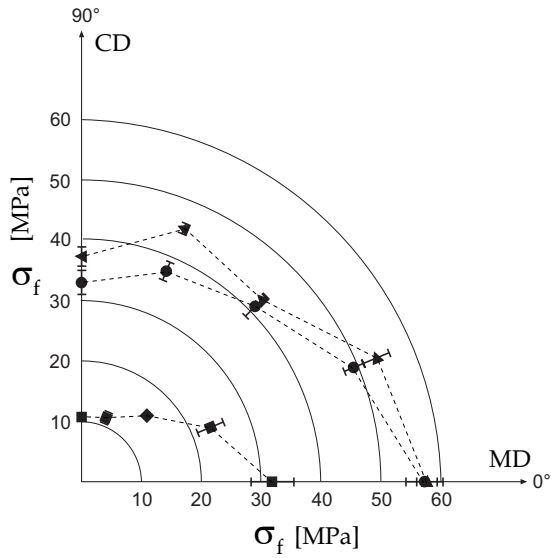

Figure 3.2: *The failure stress from Table 3.1 polar-plotted in the orientational directions for newsprint (■), kraft paper (●) and paperboard (▲). The bar refers to the standard deviation.*

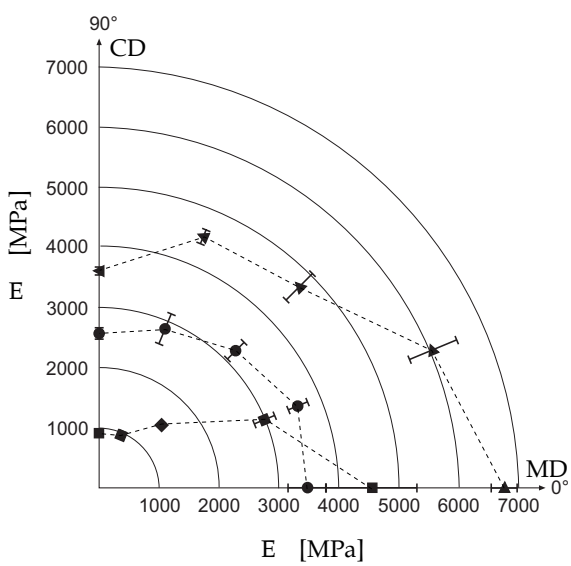

Figure 3.3: *The elastic moduli from Table 3.1 polar-plotted in the orientational directions for newsprint (■), kraft paper (●) and paperboard (▲). The bar refers to the standard deviation.*

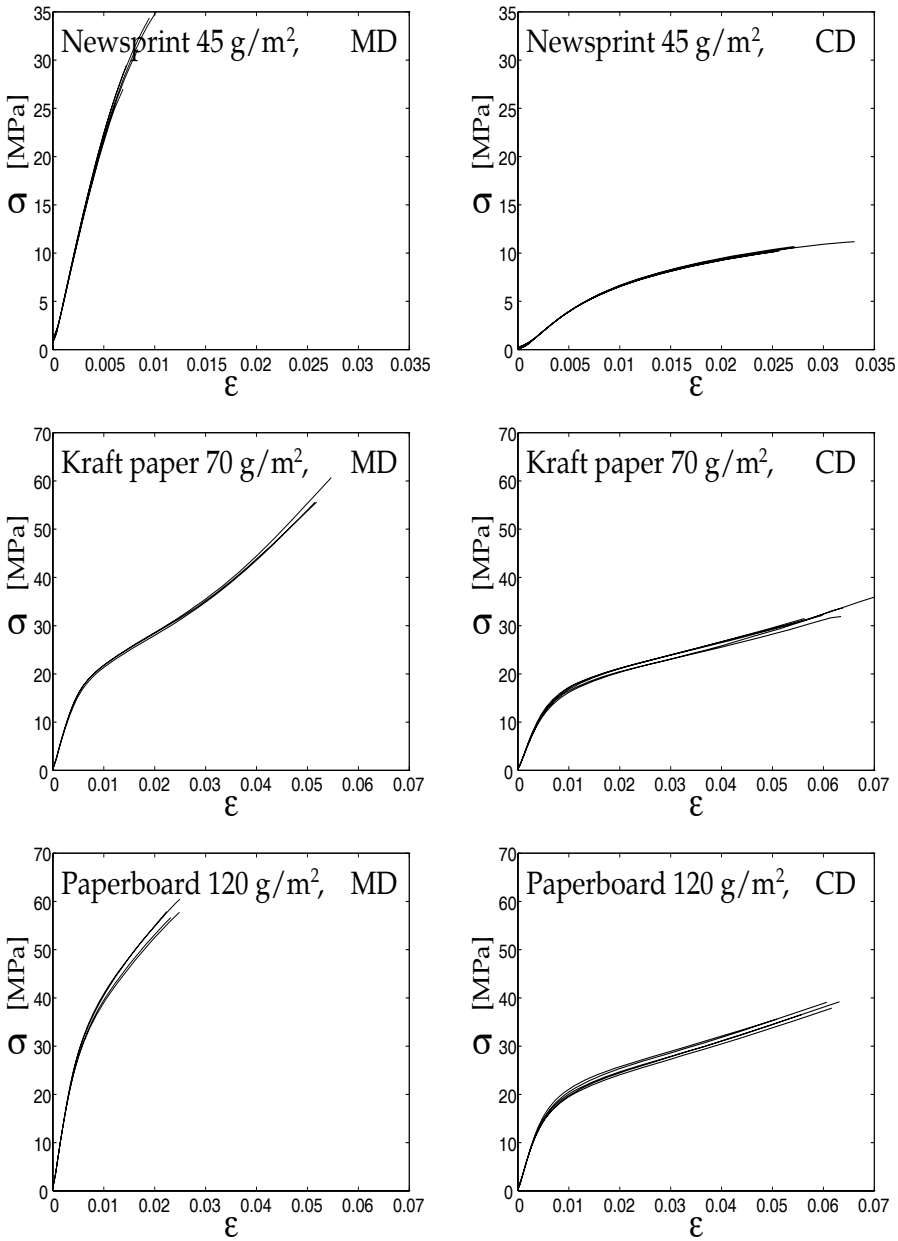

Figure 3.4: *Stress-strain curves for newsprint* 45 g/m^2, *kraft paper* 70 g/m^2 *and paperboard* 120 g/m^2.

stress is obtained as the measured maximum load divided by the width and the thickess (cf. Table 1.1) of the specimen. The elastic modulus is obtained from the linear part of the stress-strain curve, when the stress is sufficiently low for the specimen to remain elastic. In Figs. 3.2 and 3.3 the material data from Table 3.1 are polar-plotted versus the orientation direction of the paper sheet. Figure 3.2 shows that the failure stress for all the tested papers is orientation-direction dependent and for the newsprint a large orientation-direction dependency is revealed. The elastic moduli in Fig. 3.3 show a large orientation-direction dependency for the newsprint compared with the kraft paper and paperboard. The elastic moduli for the kraft paper in Fig. 3.3 show little orientation dependency.

It should be pointed out that the elastic moduli in Table 3.1 are compensated for the 10 kN load cell stiffness. Note that the 10 kN load cell stiffness (1.12 MN/m) is approximately 10 % of the 120 g/m^2 paperboard specimen stiffness (0.096 MN/m) in the MD. So, it is recommended that the measured data should always be compensated for the load cell stiffness.

The stress-strain curves for the three papers in the principal directions are shown in Fig. 3.4. It is also shown in Fig. 3.4 that all the curves are eminently reproducible and show the same basic properties as described and discussed in relation to Fig. 2.3 above, and that different stress-strain curves are obtained in the MD and CD.

3.3.2 Influence of specimen dimension on the $\sigma(\epsilon)$ curve

Figure 3.5 shows the stress-strain curves for different lengths and widths. In Fig. 3.5(a) the diversity is shown between four paperboard 120 g/m^2 strips of the length $L = 150$ mm and the width $W = 15$ mm and eight paperboard 120 g/m^2 strips of the length $L = 5$ mm and the width $W = 3$ mm. In Fig. 3.5(b) the diversity is shown between four paperboard 120 g/m^2 strips of the length $L = 150$ mm and the width $W = 15$ mm and five paperboard 120 g/m^2 strips of the length $L = 5$ mm and the width $W = 15$ mm. In Fig. 3.6 the width-length ratio, W/L, and failure strain, ϵ_f, from Fig. 3.5 are plotted. When $W/L \to +0$ the failure strain becomes equal to the uniaxial failure strain, due to zero transverse stress. It is assumed that when $W/L \to +\infty$ the failure strain approaches a failure strain restrained by the zero transverse strain.

3.3.3 Orientation of fracture section

The direction, α, of the damage band in the paper strip cut in different orientation, φ, is defined in Fig. 3.7. Table 3.2 shows the measured interval of the damage band, α, at different cut directions, φ, for the tested strips in Section 3.3.1.

Table 3.2 reveals that the fracture path of the damage band for all tested strips cut and loaded in principal directions ruptures in a straight crack path perpendicular to the loading direction. For the strips cut and loaded in 22.5, 45 and 67.5 degrees with respect to the MD, Table 3.2 shows that the fracture section tends to orient itself in the neighborhood of the principal directions of the paper. The results

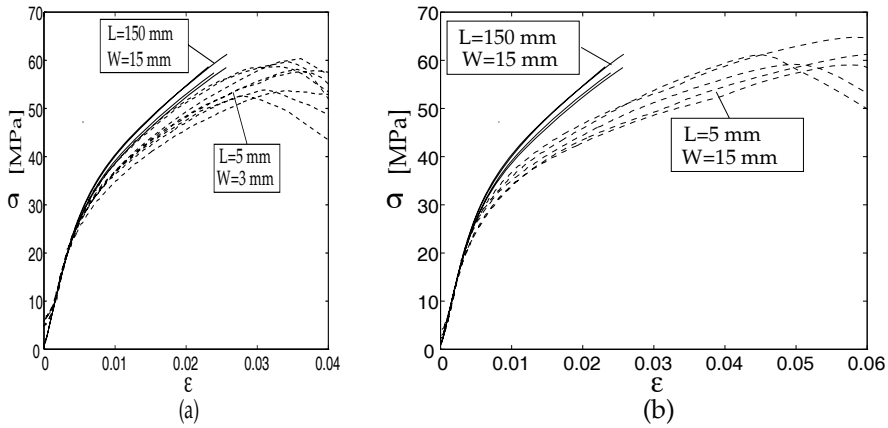

Figure 3.5: *Stress-strain curves for paperboard* 120 g/m^2.

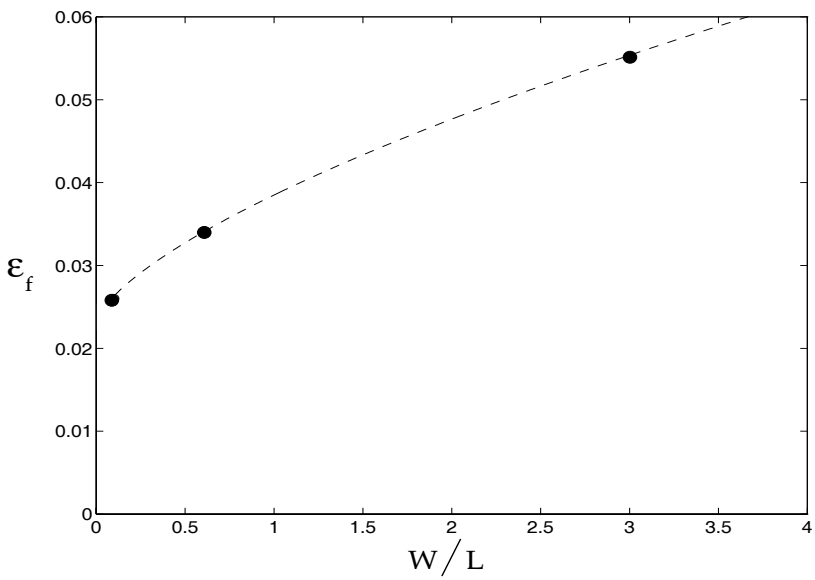

Figure 3.6: ϵ_f-W/L *curve for paperboard* 120 g/m^2.

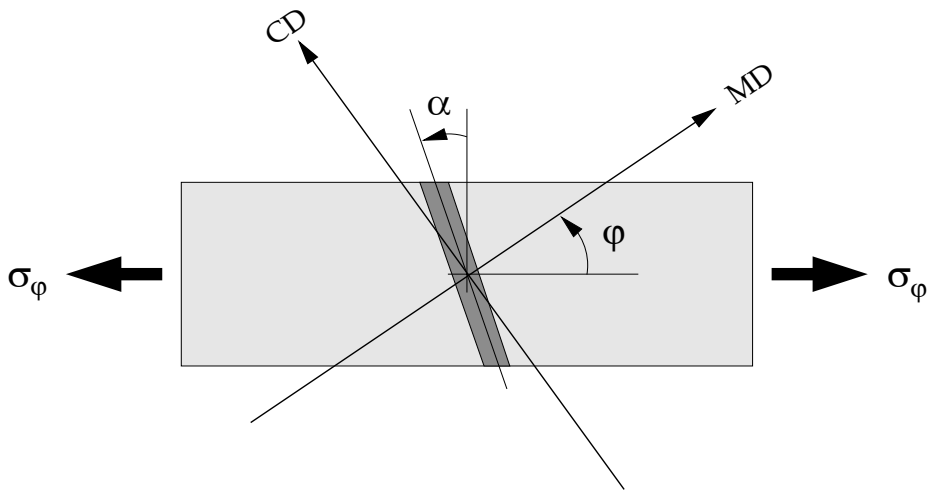

Figure 3.7: *Orientation, α, of the plane of fracture (thick dark gray line) due to load at different cut direction, φ.*

	Newsprint 45 g/m^2	Kraft paper 70 g/m^2	Paperboard 120 g/m^2
φ	α	α	α
0°	0°	0°	0°
22.5°	19° to 32°	0° to 30°	0°
45°	30° to 42°	10° to 35°	19° to 40°
67.5°	−25° to −11°	−39° to −30°	−36° to −22°
90°	0°	0°	0°

Table 3.2: *Interval in degree of the directional orientation of the damage band. The definition of the angle α and φ is found in Fig. 3.7.*

from Table 3.2 suggest that the fracture section orients itself near to the principal directions of the paper.

3.3.4 Stress-widening curves

Paper strips short enough to give a stable descending load-elongation curve after maximal load are here tested, i.e $L < L_{stable}$.

The widening of the damage zone and its self-similarity

For paperboard 120 g/m^2 three specimen geometries were tested with different widths and lengths cut in the MD. The three specimen geometries were (a) $W = 15$ mm and $L = 15$ mm, (b) $W = 5$ mm and $L = 15$ mm, and (c) $W = 3$ mm and

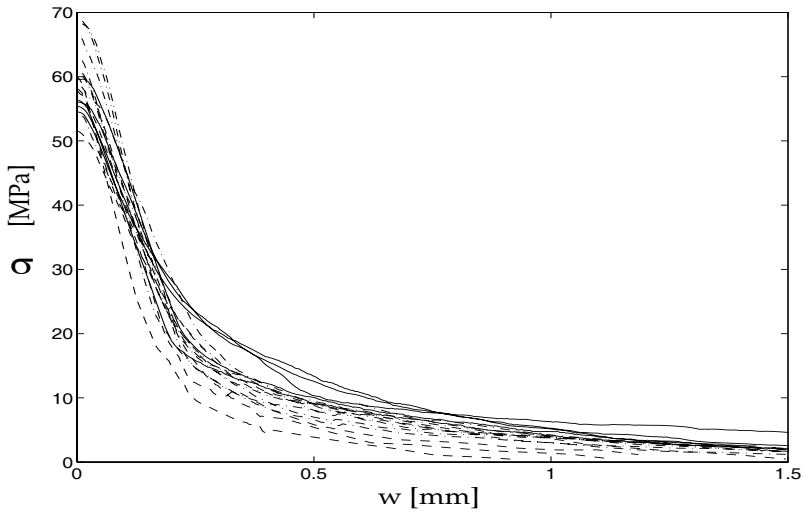

Figure 3.8: *The $\sigma(w)$ curves are obtained from three paper strip geometries, namely: (a) $L = 15$ mm and $W = 15$ mm (solid lines), (b) $L = 5$ mm and $W = 15$ mm (dashdot lines) and (c) $L = 5$ mm and $W = 3$ mm (dashed lines).*

$L = 5$ mm. For geometry (a) 5 strips were tested, for (b) 8 strips were tested and for (c) 4 strips were tested. In Fig. 3.8 the stress-widening curves for the three specimen geometries are shown. As appears in the figure, the stress-widening curves are approximately independent of the paper strip length and width. So, the transformation from load-elongation curve to stress-widening curve appears to be approximately self-similar. Self-similarity means that the widening of the damage zone, w, is governed only by properties of the material and is accordingly independent of the geometry of the specimen.

Stress-widening curves of various papers

Newsprint 45 g/m^2, kraft paper 70 g/m^2 and paperboard 120 g/m^2 were tested for one single specimen geometry. For each paper and for each direction, five nominally equal tests were made. All papers were cut from 0° to 90° in intervals of 10° with respect to the MD. The papers were 15 mm wide and long enough to be clamped in jaws 5 mm apart, cf. Fig 3.1. In Fig. 3.9 are shown the cohesive stress-widening curves in the MD and CD for newsprint, kraft paper and paperboard. It is also shown in Fig. 3.9 that all the curves are reproducible and show the same basic properties as described and discussed in relation to Fig. 2.8 above, and that different cohesive stress-widening curves in the MD and CD are obtained.

From comparison with Figs. 3.4 and 3.9 it is shown that the maximum stress is

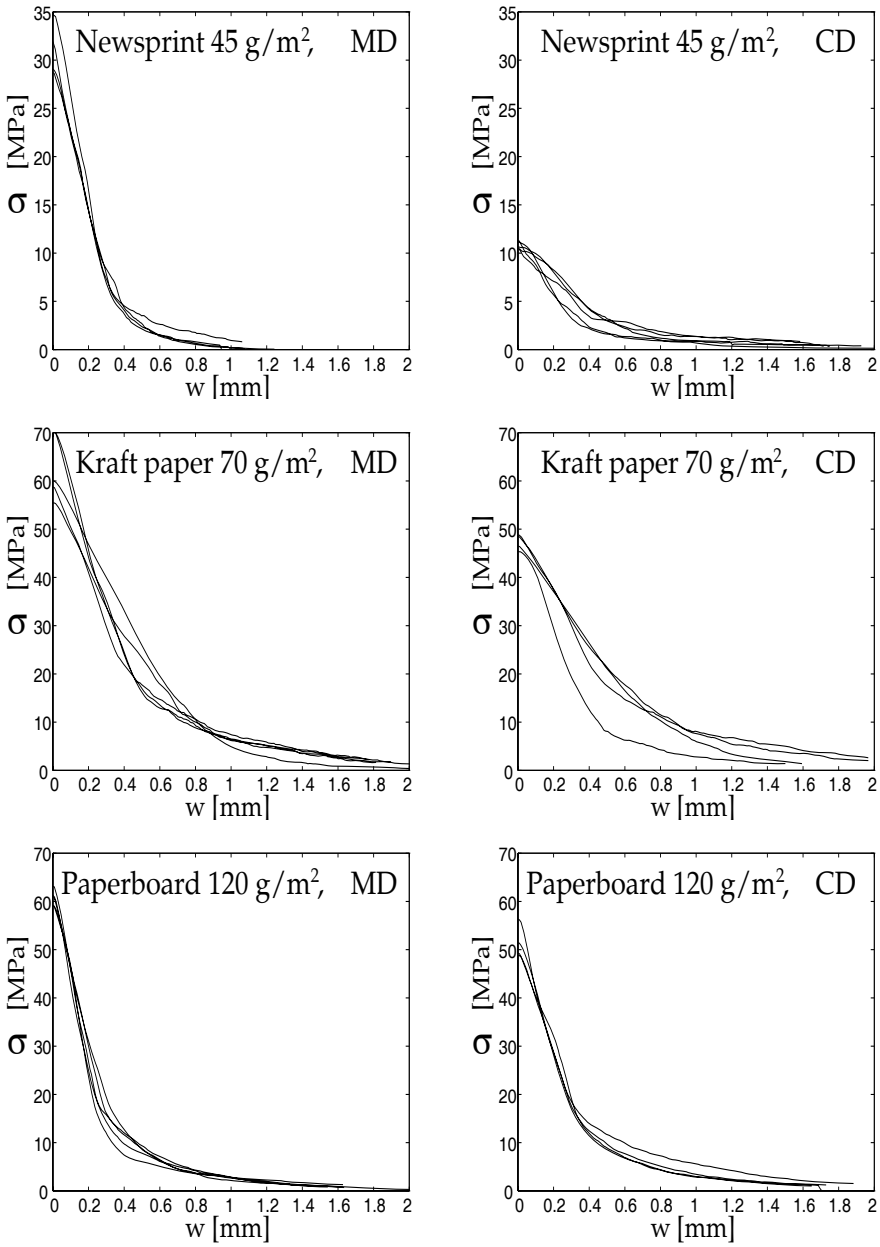

Figure 3.9: *Cohesive stress-widening curves, for newsprint* 45 g/m^2, *kraft paper* 70 g/m^2 *and paperboard* 120 g/m^2.

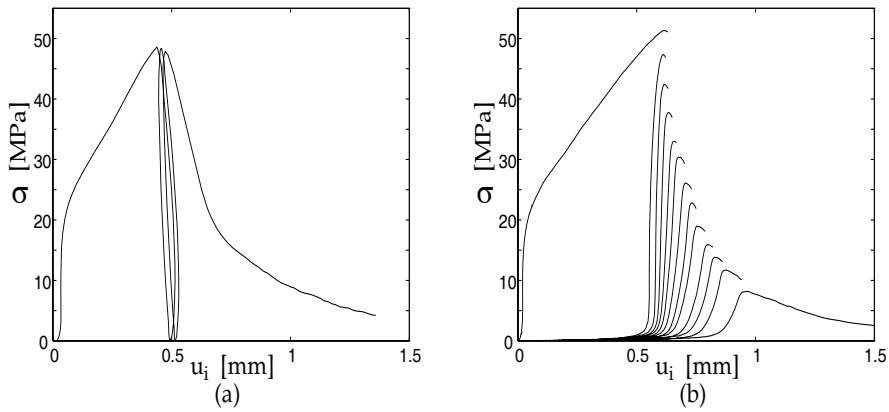

Figure 3.10: *Stress-widening curves at loading and reloading, for paperboard* 120 *g/m*^{2}*. (a) Softening and irreversibility in the CD. (b) Decrease in the reloading stiffness during softening in the CD.*

slightly decreased with increasing paper strip length. This is due to the "weak link" phenomenon, i.e. the longer the strip, the higher the probability that flaws or other micro defects will occur in the strip [75, 104].

From the observation regarding fracture direction shown in Table 3.2 it can be expected (and it was observed) that paper strips of a length of 5 mm and a width of 15 mm loaded at angles off the principal axis direction yield a crack path that is more or less zig-zag, due to interactions with the grips. Therefore, it is suggested that tests off the principal direction be disregarded due to inaccurate results that may occur because of interactions with the grips. Short paper strips loaded in the principal axis direction yield a straight crack path perpendicular to the loading direction and do not interact with the grips.

It should be pointed out that the maximal stiffness of the tested specimen, $K = EA/L$, in Table 3.1 is 2.87 MN/m. The specimen stiffness is of the same order as that of the 10 kN load cell stiffness which was measured to 1.12 MN/m. So, if the elastic moduli are to be obtained from strip lengths of 5 mm, then the measured results of the elastic moduli and the load cell stiffness must be used to calculated the elastic moduli of the specimen.

Irreversibility and decrease in the failure stress and stiffness during softening

Figure 3.10(a) shows the stress-inelastic elongation behavior from one paperboard 120 g/m^2 strip when alternately loaded and unloaded in the CD under load control. The inelastic elongation, u_i, is defined as the total elongation, u, subtracted from the elastic elongation, u_e, i.e. $u_i = u - u_e$, where u_e is assumed to correspond to the first and linear part of the measured curve. The results indicate that paper during

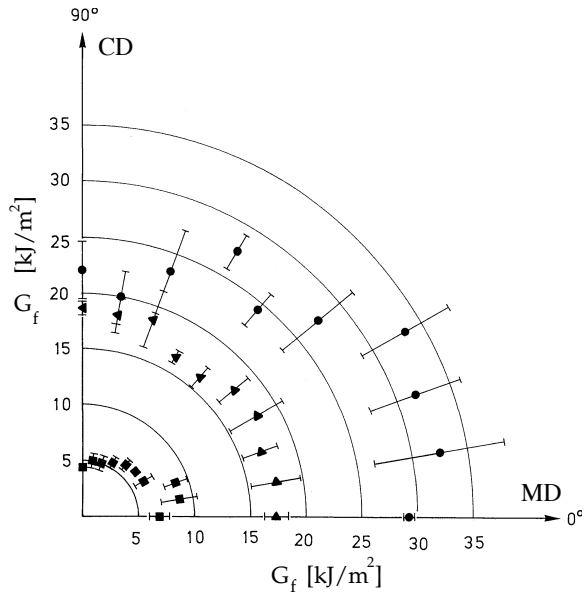

Figure 3.11: *The fracture energy in kJ/m^2, with error bars denoting the standard deviation for newsprint (■), kraft paper (●) and paperboard (▲), at different orientational directions of the paper sheet.*

fracture has a softening nature with hysteresis. The curves shown in Fig. 3.10(b) are the reloading curves at different magnitudes of softening, and are obtained by unloading at prescribed elongations after the failure load has been reached. Figure 3.10(b) shows the decrease in the failure stress and elastic stiffness during softening in the CD. It is seen that the first reloading curve has approximately the same stiffness as the initial stiffness, i.e. initially dominates the plastic softening effects. From Fig. 3.10(b) it is also seen that the failure stress at reloading of the curves is less than the stress at the unloading, i.e. occurrence of damage in the localized band during an unloading-reloading cycle is evident. So, the localized crack zone consists of a plastic and a damage part. In Fig. 3.10(b) one characteristic test is shown of seven nominally equal tests made in the CD.

3.3.5 Fracture energy and characteristic length

In Fig. 3.11 the fracture energy is polar-plotted versus the orientation direction for the three papers. The fracture energy is obtained from the cohesive stress-widening curves by numerical integration of Eq. (2.5) and from the assumption of a straight crack path perpendicular to the loading direction.

The fracture energy in Table 3.3 with the standard deviation is 7.10 ± 0.87 kJ/m^2 in the MD and 4.52 ± 0.68 kJ/m^2 in the CD for the newsprint. For the kraft paper

	Newsprint 45 g/m^2	Kraft paper 70 g/m^2	Paperboard 120 g/m^2
φ	G_f [kJ/m^2]	G_f [kJ/m^2]	G_f [kJ/m^2]
0°	7.10 ± .87	29.0 ± .45	17.0 ± .97
10°	8.42 ± 1.4	32.8 ± 6.3	17.6 ± 2.3
20°	8.42 ± .86	31.2 ± 3.7	16.4 ± 1.3
30°	6.66 ± 1.3	33.2 ± 5.4	18.1 ± 1.9
40°	6.55 ± .80	27.4 ± 4.0	17.6 ± 3.5
50°	6.31 ± .55	24.2 ± 1.6	16.3 ± 1.3
60°	5.38 ± .39	27.8 ± 2.0	16.9 ± .87
70°	5.12 ± .34	23.4 ± 4.1	18.6 ± 2.3
80°	5.06 ± .94	20.0 ± 2.4	17.9 ± 1.1
90°	4.52 ± .68	24.6 ± 4.8	18.5 ± 1.5

Table 3.3: *Fracture energy for the tested papers, mean values ± standard deviation.*

the fracture energy with the standard deviation is 29.0 ± 0.45 kJ/m^2 in the MD and 24.6 ± 4.8 kJ/m^2 in the CD. And for paperboard the fracture energy with the standard deviation is 17.0 ± 1.0 kJ/m^2 in the MD and 18.5 ± 1.5 kJ/m^2 in the CD. In Table 3.3 the fracture energy values are tabulated for cut direction from 0° to 90° in intervals of 10° with respect to the MD. The newsprint and kraft paper in Fig. 3.11 show a large orientation-direction dependency of the fracture energy, whereas the paperboard shows little or no orientation dependency. The zig-zag fracture pattern obtained for the short paper strips may be the reason for the larger standard deviation for the off-principal axes tests than for the tests made in the principal axes, cf. Fig. 3.11.

A length scale that represents the event that occurs at the mesoscale, such as the enlargements of gaps or areas with no contact between fibers and tearing of the fiber cell walls, may be introduced directly or indirectly in a mathematical model. Hillerborg et al. [42] defined a characteristic length of materials as

$$\ell_{ch} = \frac{EG_f}{\sigma_f^2} \tag{3.1}$$

The orientation dependency of the characteristic length, ℓ_{ch}, for newsprint, kraft paper and paperboard is shown in Fig. 3.12. The characteristic length in Fig. 3.12 is obtained from insertion of the measured values for the fracture energy, cf. Fig. 3.11, the fracture stress and the elastic moduli, cf. Figs. 3.2 and 3.3, into Eq. (3.1).

3.3.6 Slope and simplified shape of $\sigma(w)$ curve

For paper, it appears from the test results that the $\sigma(w)$ curve consists first of an approximately linear part and than of a long non-linear tail part. (The first part might correspond to failure of fibers and fiber-to-fiber connections and the second part to fiber-to-fiber friction during pull-out of fibers.) In some cases it is of

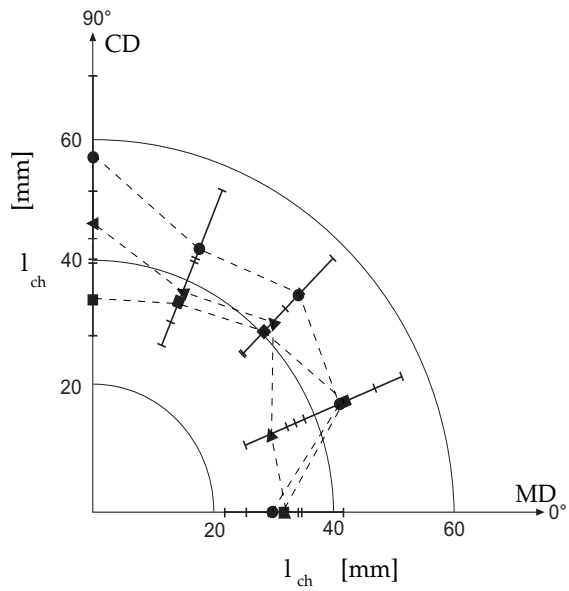

Figure 3.12: *The characteristic length, $\ell_{ch} = EG_f/\sigma_f^2$ in the unit mm, with error bars denoting the standard deviation, for newsprint (■), kraft paper (●) and paperboard (▲), at different orientational directions of the paper sheet.*

prime interest to consider the steepest part of the $\sigma(w)$ curve, and for many applied analyses of fracture the first part of the curve is most important. The second tail-part of the curve may in some cases not even be activated before the instant of global damage or failure of the actual paper or paper article.

For the above reasons, in Table 3.4, N_{max} is indicated for the steepest and approximately linear first part of the $\sigma(w)$ curve for the three papers when loaded in the MD and CD. The corresponding $G_{f_{min}}$ as defined in Fig. 2.11 is also given. To enable comparision and to summarize test results, G_f, E, σ_f and EG_f/σ_f^2 and $EG_{f_{min}}/\sigma_f^2$ are also included in Table 3.4.

3.4 Critical and stable length

The critical length, $L_{critical}$, is defined as the shortest length of the paper strip for which the load-elongation curve (in stroke-controlled testing by a stiff testing device) immediately falls from a point of instability to zero stress [32]. The length of the longest paper strips which cause the load-elongation curve to show a stable descending branch with no immediate fall of the stress [19], cf. Fig. 2.1, is the definition for the stable length, L_{stable}, of the paper strip. The case when $L_{critical} > L > L_{stable}$ implies that a sudden drop of the stress occurs from a point of instability

	Newsprint		Kraft paper		Paperboard	
	MD	CD	MD	CD	MD	CD
N_{max}, GN/m^3	86.9	23.7	88.8	57.1	153.8	108.3
$G_{f_{min}}$, kJ/m^2	5.85	2.55	20.2	20.1	11.7	12.5
G_f, kJ/m^2	7.10	4.52	29.0	24.6	17.0	18.5
E, MPa	4560	873	3470	2520	6780	3570
σ_f, MPa	31.9	10.8	57.3	33.1	57.7	37.4
$EG_{f_{min}}/\sigma_f^2$, mm	26.2	18.4	19.5	22.1	22.1	16.5
EG_f/σ_f^2, mm	31.8	33.8	30.70	56.7	34.7	47.3

Table 3.4: *Material data from the three papers' stress-widening curves.*

to a lower stress, not equal to zero.

Table 3.5 presents experimentally determined values for the critical and the stable paper lengths tabulated in the MD and CD. The values in Table 3.5 were obtained by gradually (in steps of 5 mm) shortening the paper strip length from 75 mm to 15 mm. For each length two nominally equal tests were made. A width of 15 mm was used throughout the tests. In the table 's' refers to $L \leq L_{stable}$, '-' refers to $L_{stable} < L < L_{critical}$ and 'i' refers to $L \geq L_{critical}$. Only those lengths in the table referred to as 's', '-' or 'i' were tested. Table 3.5 shows that the critical paper length values are greater than the stable paper length values, as stated above, and that the values in the CD are greater than those in the MD.

In Table 3.6 measured and calculated values for the stable paper length are tabulated in the MD and CD. The calculated values for the stable paper length are obtained by inserting measured values of the failure stress and the elastic moduli from Table 3.1 and the fracture energy, $G_{f_{min}}$, from Table 3.4 together with the 10 kN load cell stiffness (1.12 MN/m) into Eq. (2.18). It is shown in the table that the calculated values of the stable length and the measured values are in the same range. The reason for the large difference between the measured and calculated values for newsprint 45 g/m^2 in the MD is not known.

3.5 Proposed method for testing fracture properties

For measuring the mode I fracture properties, it is important that the specimen types and procedures proposed are relevant and easy to use, in order to give the required properties of the paper tested in a correct and rational manner.

The uniaxial tests are best carried out on a stiff universal testing instrument including a stiff load cell. The paper strip samples are preferably held by pneumatic vice-action grips between two parallel jaw faces, cf. Fig. 3.1. This type of grip has the advantage of allowing accurate fixation without any sliding, as well as rapid and easy loading of the paper strips. In the uniaxial load-elongation tension test the

L [mm]	Newsprint		Kraft paper		Paperboard	
	MD	CD	MD	CD	MD	CD
15	s		s		s	
20	s	s	s	s	s	s
25	-	s	s	s	-	s
30	-	s	s	s	-	s
35	i	-	-	s	-	-
40				-	-	
45					i	
50	i	-	-	-	i	-
55			-			
60		-	i	-		-
65		i		-		i
70						
75				i		

Table 3.5: *Stable or instable specimen length. In the table 's' refers to* $L \leq L_{stable}$*, '-' refers to* $L_{stable} < L < L_{critical}$ *and 'i' refers to* $L \geq L_{critical}$*.*

	Measured L_{stable}		Calculated L_{stable}	
	MD	CD	MD	CD
Newsprint	20-25	30-35	48	36
Kraft paper	30-35	35-40	34	41
Paperboard	20-25	30-35	30	26

Table 3.6: *The stable paper length in mm.*

length, L, (see Fig. 3.1) is easy to adjust to the required length, whereas the width, W, (see Fig. 3.1) must be cut in order to get the required width. It is therefore suggested that the width for different lengths be the same. The load is recorded by the load cell and the elongation by the moving crosshead.

It is suggested that the material parameters that can be found from the stress-strain curve be taken from paper strips that exhibit immediate rupture. The descending part of the load-elongation curve should be taken from paper strips that exhibit stable rupture.

3.5.1 Ascending part of the load-elongation curve

The material parameters found from the ascending part of the load-elongation curve are the failure strength σ_f and the elastic modulus E. The test method for the ascending part of the uniaxial load-elongation curve should follow the Tappi standard T 494 os-70, [98]. In addition to σ_f and E the test report should normally include

the $\sigma(\epsilon)$ curve. In the evalution of strain from the crosshead movement, possible compliance in the load cell or other parts of the equipment must be considered.

3.5.2 Descending part of the load-elongation curve

The descending part of the load-elongation curve, giving the stress-widening curve $\sigma(w)$, i.e. fracture softening properties of the fracture region including fracture energy G_f, should only be measured in the MD and CD, since the plane of fracture is in general perpendicular to the load only for uniaxial loads in the MD and CD. Paper strips cut in other directions develop crack paths that may interact with the grips, and this may give inaccurate results. Short paper strips that give stable fracture must be used.

It is recommended to cut from each test unit of the sample 10 test specimens in each principal direction of the paper, 15 mm wide with sides parallel and long enough to be clamped in jaws 5 mm apart. The constant rate of elongation for a 5 mm test span is 0.25 mm/min.

It is further recommended that the environmenal condition follow the Tappi standard T 494 os-70.

It is also recommended, for paperboard greater than 150 g/m^2, to use serrated jaw faces in the grips to avoid sliding, whereas for paper less than or equal to 150 g/m^2, to use flat jaws in grips which have been treated with emery paper to avoid sliding. There is always a risk that serrated jaw faces will damage the paper.

The recorded load-elongation curve is transformed to the stress-widening curve by using Eq. (2.4), i.e.

$$w = u - \epsilon_f L + (\sigma_f - \sigma)\frac{L}{E} \tag{3.2}$$

as is illustrated in Fig. 3.13. The test report for each test should include the $\sigma(w)$ curve and the corresponding fracture energy G_f determined by integration of the $\sigma(w)$ curve. The slope of the steepest linear part of the $\sigma(w)$ curve and the corresponding $G_{f_{min}}$ (Fig. 2.11) may be included if relevant.

3.5.3 Comments

If instability occurs during the test with the above recommended length and width of the paper sample, it is then recommended to first exchange the currently used load cell for a stiffer one and, if the paper strip still shows some instability in the descending part, to shorten the distance between the grips (see Fig. 3.1) until a stable descending part of the load-elongation curve occurs. However, the specimen length should be at least several millimetres, i.e. at least about as long as the fibers in the paper.

In the evaluation of w by means of Eq. (3.2) the stiffness E/L should - as illustrated in Fig. 3.13 - be made equal to the slope of the linear part of the ascending part of the recorded $\sigma(u)$ curve. In this way possible (linear elastic) deformations in

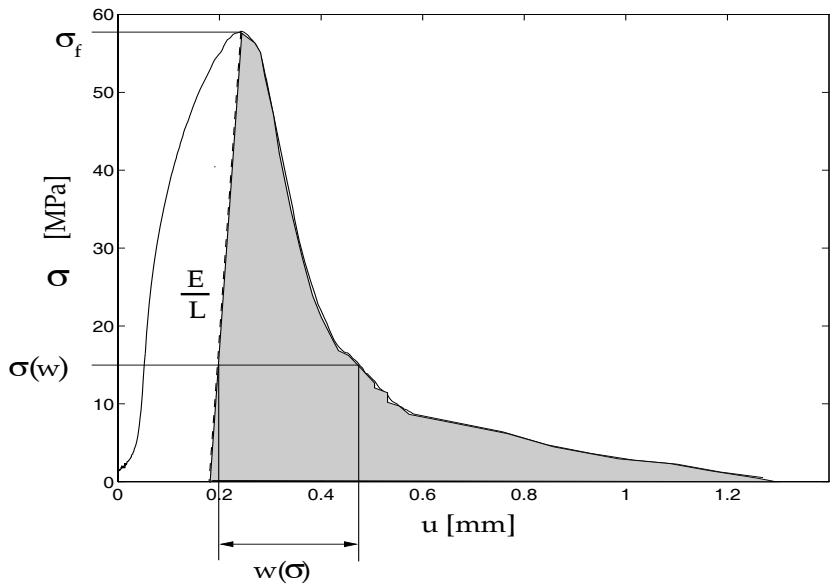

Figure 3.13: *Evaluation of $\sigma(w)$ curve from recorded $\sigma(u)$ curve.*

the load cell and other parts of the equipment are included and taken into account in the evaluation.

Chapter 4

In-plane constitutive models for paper

4.1 Introduction

The experimental observations described in Chapter 3 for the in-plane properties of paper, i.e. the anisotropic elastic, plastic and fracture behavior, are in this chapter described by in-plane constitutive models. In Section 4.2 a pressure independent anisotropic yield criterion, [49], is used in the modelling of anisotropic plasticity. The anisotropic fracture in paper, Section 4.3, is described by an anisotropic failure criterion and a failure potential. In Section 4.3 the formulation of an elastic-cohesive softening constitutive model is also described.

From Fig. 2.1 it is clear that paper behaves as an elastic-plastic-fracture material, whereas the constitutive models to be discussed only cover elastic-plastic or elastic-fracture behavior. This limitation in the constitutive modelling is in general not fully satisfactory. In the following chapters, cases will be discussed where this limitation affects (or slightly affects) the results and where the two constitutive models are mixed as different materials in different regions.

Generally paper is known to be a rate-dependent material, [3]. Here however, rate effects are neglected and paper is considered to be a rate-independent material. The anisotropic elasticity is modelled by a linear elastic orthotropic in-plane stiffness matrix $\mathbf{D}$, cf. Table 4.1. The linear elastic orthotropic stiffness matrix connects the rate of the in-plane elastic strain vector, $\dot{\boldsymbol{\epsilon}}^e$, to the rate of the in-plane stress vector, $\dot{\boldsymbol{\sigma}}$, as

$$\dot{\boldsymbol{\sigma}} = \mathbf{D}\dot{\boldsymbol{\epsilon}}^e \tag{4.1}$$

where $\dot{\boldsymbol{\sigma}} = (\dot{\sigma}_1, \dot{\sigma}_2, \dot{\sigma}_3, \dot{\sigma}_6)^T$ and $\dot{\boldsymbol{\epsilon}}^e = (\dot{\epsilon}_1^e, \dot{\epsilon}_2^e, \dot{\epsilon}_3^e, \dot{\epsilon}_6^e)^T$. The subindexes 1, 2, 3 and 6 denote the MD, CD, ZD and in-plane shear components of the stress and strain rate vectors, respectively. It is assumed the out-of-plane stress is zero, i.e. $\dot{\sigma}_3 = 0$, in Eq. (4.1).

Elastic relations
$\dot{\sigma}_1 = D_{11}\dot{\epsilon}_1^e + D_{12}\dot{\epsilon}_2^e + D_{13}\dot{\epsilon}_3^e$ $\dot{\sigma}_2 = D_{12}\dot{\epsilon}_1^e + D_{22}\dot{\epsilon}_2^e + D_{23}\dot{\epsilon}_3^e$ $\dot{\sigma}_3 = D_{13}\dot{\epsilon}_1^e + D_{23}\dot{\epsilon}_2^e + D_{33}\dot{\epsilon}_3^e$ $\dot{\sigma}_6 = D_{66}\dot{\epsilon}_6^e$ $\dot{\sigma}_3 = 0$
$D_{11} = E_1/(1-\nu_{12}\nu_{21})$ $D_{12} = E_1[\nu_{21}/(1-\nu_{12}\nu_{21})]$ $D_{13} = E_3(\nu_{12}\nu_{23}+\nu_{13})/(1-\nu_{12}\nu_{21})$ $D_{22} = E_2/(1-\nu_{12}\nu_{21})$ $D_{23} = E_3(\nu_{21}\nu_{13}+\nu_{23})/(1-\nu_{12}\nu_{21})$ $D_{33} = E_3/(1-\nu_{12}\nu_{21})$ $D_{66} = G_6$ where it is assumed that $(E_3/E_1) \sim 0$ and $(E_3/E_2) \sim 0$.

Table 4.1: *In-plane elastic and engineering constants of an orthotropic material, cf. [55].*

4.2 In-plane elastic-plastic constitutive model

4.2.1 Introduction

The experimental in-plane anisotropic data for pre-peak stresses in Fig. 2.5 suggest the need to use a plane stress constitutive model to capture the anisotropic elasticity and anisotropic plasticity. The anisotropic elasticity is modelled with an anisotropic moduli matrix, cf. Eq. (4.1). The anisotropic plasticity is more complex to model, since experiments reveal that the yield stresses and strain hardening behave anisotropically, [50, 73]. Karafillis, Boyce and Parks, [50], have suggested a model that is able to capture these features. This constitutive model for paper is, for plane stress condition, the same as a constitutive model suggested in [49]. Below the modelling of anisotropic plasticity by [49] is briefly reviewed.

In this chapter, well-known constitutive laws in plasticity theory are not always given any specific reference. A comprehensive description of plasticity theory can be found in e.g. [11, 40, 51, 56, 60].

The total strain rate vector, $\dot{\boldsymbol{\epsilon}} = (\dot{\epsilon}_1, \dot{\epsilon}_2, \dot{\epsilon}_3, \dot{\epsilon}_6)^T$, is assumed to be the sum of the elastic strain and the plastic strain, as

$$\dot{\boldsymbol{\epsilon}} = \dot{\boldsymbol{\epsilon}}^e + \dot{\boldsymbol{\epsilon}}^p \tag{4.2}$$

where $\dot{\boldsymbol{\epsilon}}^p = (\dot{\epsilon}_1^p, \dot{\epsilon}_2^p, \dot{\epsilon}_3^p, \dot{\epsilon}_6^p)^T$ is the plastic strain rate.

4.2.2 Plastic constitutive relation

The in-plane yield stress rate, $\dot{\sigma}_y$, and the plastic yield strain rate, $\dot{\epsilon}_y^p$, are assumed to have the following constitutive relation,

$$\dot{\sigma}_y = H_y \dot{\epsilon}_y^p \tag{4.3}$$

where $H_y = H_y(\epsilon_y^p)$ is the general plastic modulus.

4.2.3 The Karafillis-Boyce yield criterion

The pressure-independent anisotropic yield criterion used for paper has been developed by Karafillis and Boyce, [49]. The anisotropic yield criterion is an extension of an isotropic yield criterion. The isotropic yield criterion, [49], is able to describe all yield surfaces lying between an upper bound and a lower bound. The upper bound is the limiting value of the sum of the two greater diameters of Mohr's circle, cf. [44, 49]. The lower bound coincides with the Tresca yield criterion [99]. The general isotropic yield criterion by Karafillis and Boyce, [49], is given by

$$f = \phi - 2\sigma_y^{2k} \tag{4.4}$$

where

$$\phi = (1-c)f_1 + c3^{2k}/(2^{2k-1}+1)f_2 \tag{4.5}$$

$0 \leq c \leq 1$ is the mixing factor and k is a positive integer describing the shape of the yield surface. f_1 and f_2 are functions in Eq. (4.5). The function f_1 spans the region between the lower bound and the Mises yield surface, [62], and the function f_2 spans the region between the Mises yield surface and the upper bound. The functions f_1 and f_2 read as

$$f_1 = (S_I - S_{II})^{2k} + (S_{II} - S_{III})^{2k} + (S_{III} - S_I)^{2k} \tag{4.6}$$

$$f_2 = S_I^{2k} + S_{II}^{2k} + S_{III}^{2k} \tag{4.7}$$

where the S_I, S_{II} and S_{III} are the principal deviatoric stress components. For any loading condition the constraint $f \leq 0$ must be fulfilled, where $f = 0$ represents loading from a plastic state.

Anisotropy is obtained from a linear transformation from the anisotropic stress space to the isotropic stress space, called the isotropic plasticity equivalent (IPE) stress space, [49], as

$$\boldsymbol{S} = \boldsymbol{\mathcal{L}}\boldsymbol{\sigma} \tag{4.8}$$

where $\boldsymbol{S} = (S_1, S_2, S_3, S_6)^T$ is the IPE stress acting on the equivalent mapped isotropic material and $\boldsymbol{\mathcal{L}}$ is the mapping matrix. The mapping matrix needs only four constant parameters, $\{C, \alpha_1, \alpha_2, \gamma_3\}$, for plane stress in order to describe the anisotropic plasticity, [49]. This is expressed as

$$\boldsymbol{\mathcal{L}} = C \begin{bmatrix} 1 & \beta_1 & \beta_2 & 0 \\ \beta_1 & \alpha_1 & \beta_3 & 0 \\ \beta_2 & \beta_3 & \alpha_2 & 0 \\ 0 & 0 & 0 & \gamma_3 \end{bmatrix} \tag{4.9}$$

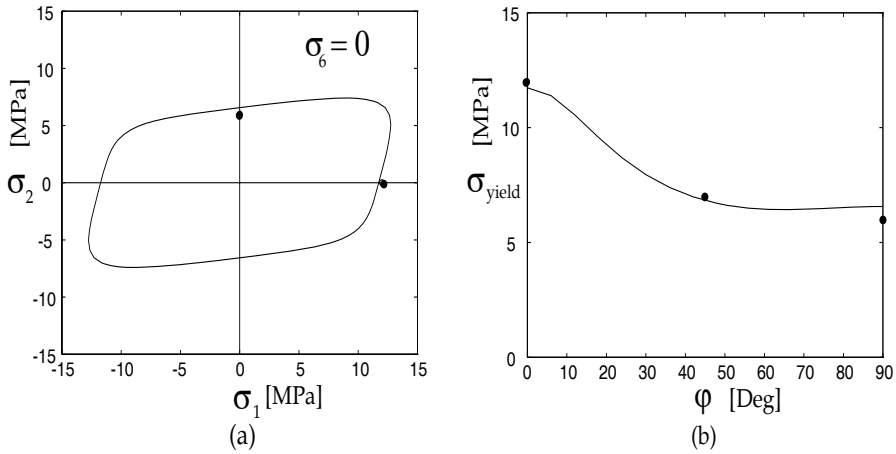

Figure 4.1: *(a) In-plane yield surface at $\sigma_6 = 0$. (b) Yield stress-material direction curve. The circles, ●, are experimental data taken from paperboard 240 g/m^2.*

where $\beta_1 = (\alpha_2 - \alpha_1 - 1)/2$, $\beta_2 = (\alpha_1 - \alpha_2 - 1)/2$ and $\beta_1 = (1 - \alpha_1 - \alpha_2)/2$. Note that the mapping matrix is symmetric, i.e. $\boldsymbol{\mathcal{L}} = \boldsymbol{\mathcal{L}}^T$.

In Fig. 4.1 the initial yield surface is calibrated to paperboard 240 g/m^2, [50]. The in-plane yield surface at zero shear stress, i.e. $\sigma_6 = 0$, is shown in Fig. 4.1(a) and the uniaxial yield stress at different material directions is shown in Fig. 4.1(b). The black circles, ●, in Fig. 4.1 denote experimental data taken from paperboard 240 g/m^2, [73].

It should be pointed out that the Karafillis-Boyce criterion captures both the variation in the yield strength and the variation in the plastic straining. For example, the classical orthotropic yield criterion by Hill, [40], is limited to capturing either the variation in the yield strength or the variation in the plastic straining.

4.2.4 Evolution laws

The evolution laws for the anisotropic plastic strain rate, $\dot{\boldsymbol{\epsilon}}^p$, the IPE strain rate, $\dot{\boldsymbol{E}}^p$, and the uniaxial plastic strain rate $\dot{\epsilon}_y^p$ are assumed to follow the flow rules

$$\dot{\boldsymbol{\epsilon}}^p = \dot{\lambda}_y \frac{\partial f}{\partial \boldsymbol{\sigma}}, \; \dot{\boldsymbol{E}}^p = \dot{\lambda}_y \frac{\partial f}{\partial \boldsymbol{S}} \text{ and } \dot{\epsilon}_y^p = -\dot{\lambda}_y \frac{\partial f}{\partial \sigma_y} \tag{4.10}$$

where the plastic multiplier $\dot{\lambda}_y$, and the yield criterion $f \leq 0$, fulfill the Kuhn-Tucker relations, $\dot{\lambda}_y f = 0$ and $\dot{\lambda}_y \geq 0$. The function f is required to be convex and smooth, which is fulfilled if $2k > 1$ in Eq. (4.4), [49].

The plastic work density in the anisotropic material is assumed to be equal to that of the IPE material, i.e.

$$\boldsymbol{\sigma}^T \dot{\boldsymbol{\epsilon}}^p = \boldsymbol{S}^T \dot{\boldsymbol{E}}^p \tag{4.11}$$

where $\dot{\boldsymbol{E}}^p$ is a strain state variable associated to the IPE stress. From Eqs. (4.11) and (4.8) we obtain

$$\boldsymbol{\sigma}^T \dot{\boldsymbol{\epsilon}}^p = \boldsymbol{S}^T \dot{\boldsymbol{E}}^p = (\boldsymbol{\mathcal{L}}\boldsymbol{\sigma})^T \dot{\boldsymbol{E}}^p = \boldsymbol{\sigma}^T \boldsymbol{\mathcal{L}}^T \dot{\boldsymbol{E}}^p = \boldsymbol{\sigma}^T \boldsymbol{\mathcal{L}} \dot{\boldsymbol{E}}^p \tag{4.12}$$

and hence we may define $\dot{\boldsymbol{E}}^p$ by the relationship

$$\dot{\boldsymbol{\epsilon}}^p = \boldsymbol{\mathcal{L}} \dot{\boldsymbol{E}}^p \tag{4.13}$$

4.2.5 The elastic-plastic continuum stiffness matrix

If plastic loading is occurring, we require that the criterion $f = 0$ is continuously satisfied. This means that the consistency equation, $\dot{f} = 0$, has to be fulfilled, i.e. in view of Eq. (4.4)

$$\dot{\phi} - 4k\sigma_y^{2k-1}\dot{\sigma}_y = 0 \tag{4.14}$$

where $\dot{\sigma}_y$ is the yield stress rate. Hence by Eqs. (4.3), (4.4) and (4.10)c the yield stress rate is given by

$$\dot{\sigma}_y = -H_y \dot{\lambda}_y \frac{\partial f}{\partial \sigma_y} = H_y \dot{\lambda}_y 4k\sigma_y^{2k-1} \tag{4.15}$$

$\dot{\phi}$ is obtained from a combination of Eqs. (4.14) and (4.15) as

$$\dot{\phi} = H_y \dot{\lambda}_y 16k^2 \sigma_y^{4k-2} \tag{4.16}$$

and from Eqs. (4.5)-(4.9), (4.10) and (4.13) we obtain

$$\dot{\phi} = \left(\frac{\partial f}{\partial \boldsymbol{S}}\right)^T \dot{\boldsymbol{S}} = \left(\frac{\partial f}{\partial \boldsymbol{S}}\right)^T \boldsymbol{\mathcal{L}}\dot{\boldsymbol{\sigma}} = \left(\boldsymbol{\mathcal{L}}\frac{\partial f}{\partial \boldsymbol{S}}\right)^T \dot{\boldsymbol{\sigma}} = \left(\frac{\partial f}{\partial \boldsymbol{\sigma}}\right)^T \dot{\boldsymbol{\sigma}} \tag{4.17}$$

Insertion of Eqs. (4.1), (4.2) and (4.10) into Eq. (4.17) shows that the function $\dot{\phi}$ is expressed in the total strain rate and the plastic multiplier relation, as

$$\dot{\phi} = \left(\frac{\partial f}{\partial \boldsymbol{\sigma}}\right)^T \mathbf{D}\dot{\boldsymbol{\epsilon}}^e = \left(\frac{\partial f}{\partial \boldsymbol{\sigma}}\right)^T \mathbf{D}\left(\dot{\boldsymbol{\epsilon}} - \dot{\boldsymbol{\epsilon}}^p\right) = \left(\frac{\partial f}{\partial \boldsymbol{\sigma}}\right)^T \mathbf{D}\left(\dot{\boldsymbol{\epsilon}} - \dot{\lambda}_y \frac{\partial f}{\partial \boldsymbol{\sigma}}\right) \tag{4.18}$$

Combination of Eqs. (4.16) and (4.18) shows that the plastic multiplier is related to the total strain rate as

$$\dot{\lambda}_y = \frac{1}{A_y}\left(\frac{\partial f}{\partial \boldsymbol{\sigma}}\right)^T \mathbf{D}\dot{\boldsymbol{\epsilon}} \tag{4.19}$$

where A_y is a positive scalar given by

$$A_y = \left(\frac{\partial f}{\partial \boldsymbol{\sigma}}\right)^T \mathbf{D}\frac{\partial f}{\partial \boldsymbol{\sigma}} + 16k^2\sigma_y^{4k-2}H_y \tag{4.20}$$

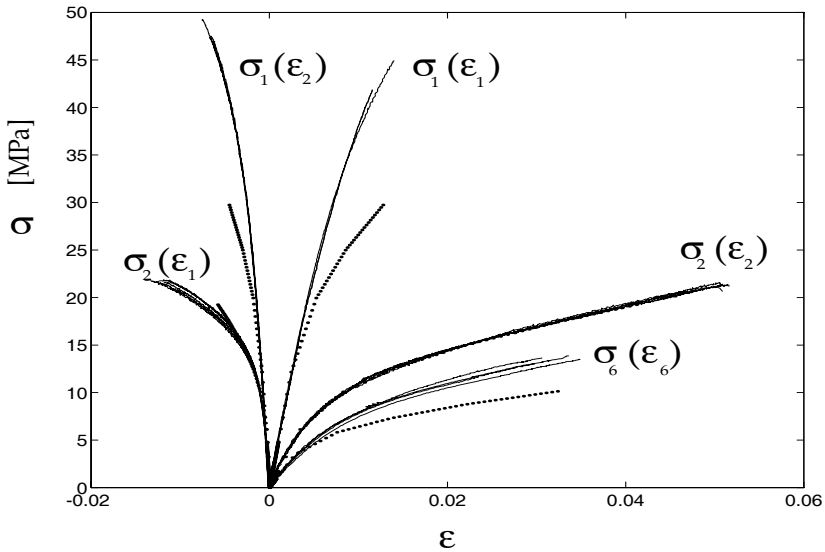

Figure 4.2: *Stress-strain curves due to uniaxial tension loading in the 1- and 2-direction together with the in-plane shear stress-shear strain curve. The solid curves are experimental data and the dotted curves are the behavior of the KB model.*

The continuum stiffness matrix that relates the stress rate to the total strain rate is obtained from insertion of Eqs. (4.2), (4.10) and (4.19) into (4.1), as

$$\dot{\boldsymbol{\sigma}} = \mathbf{D}^{ep}\dot{\boldsymbol{\epsilon}} \tag{4.21}$$

where

$$\mathbf{D}^{ep} = \mathbf{D} - \frac{1}{A_y}\mathbf{D}\frac{\partial f}{\partial \boldsymbol{\sigma}}\left(\frac{\partial f}{\partial \boldsymbol{\sigma}}\right)^T \mathbf{D} \tag{4.22}$$

It is assumed that the out-of-plane stress is zero, i.e. $\dot{\sigma}_3 = 0$, in Eq. (4.21). This means that Eq. (4.21) reduces to

$$\begin{aligned} \dot{\bar{\boldsymbol{\sigma}}} &= \bar{\mathbf{D}}^{ep}\dot{\bar{\boldsymbol{\epsilon}}} \\ \dot{\epsilon}_3 &= \frac{D^{ep}_{13}}{D^{ep}_{33}}\dot{\epsilon}_1 + \frac{D^{ep}_{23}}{D^{ep}_{33}}\dot{\epsilon}_2 + \frac{D^{ep}_{26}}{D^{ep}_{33}}\dot{\epsilon}_6 \end{aligned} \tag{4.23}$$

where $\dot{\bar{\boldsymbol{\sigma}}} = (\dot{\sigma}_1, \dot{\sigma}_2, \dot{\sigma}_6)^T$, $\dot{\bar{\boldsymbol{\epsilon}}} = (\dot{\epsilon}_1, \dot{\epsilon}_2, \dot{\epsilon}_6)^T$ and $\bar{\mathbf{D}}^{ep}$ is the continuum stiffness matrix for plane stress condition.

4.2.6 Comments

The calibration procedure for applying the elastic-plastic plane stress constitutive model to a specific anisotropic material is thoroughly discussed by Karafillis-Boyce,

cf. [49]. Karafillis, Boyce and Parks, [50] have calibrated the Karafillis-Boyce (KB) constitutive model to in-plane paperboard 240 g/m^2 data, [73]. In Fig. 4.2 the in-plane KB constitutive model (dotted lines) is plotted together with experimental data (solid lines). From uniaxial tension tests in the MD, $\sigma_1(\epsilon_1)$ and $\sigma_1(\epsilon_2)$ are recorded and from uniaxial tension tests in the CD, $\sigma_2(\epsilon_1)$ and $\sigma_2(\epsilon_2)$ are recorded, [73]. In Fig. 4.2 the experimental in-plane shear stress-shear strain curve, $\sigma_6(\epsilon_6)$, is obtained from in-plane loading at 45 degrees to the MD, cf. [73]. The model fits the data poorly in the plastic region except in the calibration direction, i.e. the CD. This is assumed to be due to the reason that isotropic hardening is chosen in the KB constitutive model.

4.3 In-plane elastic-cohesive softening constitutive model

4.3.1 Introduction

The cohesive crack model is used as the basis for the formulation of an orthotropic smeared crack constitutive relation to be used in the finite element formulation, cf. [25, 42]. The finite element formulation gives us a theoretical tool in the study of the initiation and stable growth of the localized damage zone in arbitrary in-plane structures due to in-plane loading.

In the finite element method the constitutive model is expressed in the stress-strain space. So the descending stress-crack widening relation has to be rewritten as a stress-crack strain relation. However, it has been shown that if the crack strain is defined in the conventional way, as in continuum mechanics, then the total fracture energy dissipation is approaching zero when the element size becomes infinitely small in the finite element analysis, cf. [8]. To ensure that the correct amount of fracture energy is dissipated independent of the mesh size, other theories must be used. Such methods exist, namely the discrete and smeared crack theory [1, 9, 39, 42, 106] and the so-called higher order continuum based methods, such as the couple-stress [22, 31, 53, 78], non-local [10, 26, 65, 94] and strain-gradient theories [16, 63, 83]. The higher order theories' numerical algorithms are more complex, cf. [16, 78, 94], compared to the discrete and smeared crack theory, cf. [17]. The smeared crack theory can be treated numerically in the same manner as in classical plasticity theory [17]. To obtain mesh objectivity in the smeared strain theory, the localized damage effects must occur inside one element [9, 42], whereas in higher order theories at least two elements must be used to detect the width of the damage zone in order to obtain mesh objectivity, cf. [78, 94]. If the size of the damage zone is not of prime interest, but the overall response is, the smeared strain theory is a suitable choice.

The present aim is to describe the damage evolution in paper, as discussed in Chapter 2. The smeared cracked constitutive theory is adopted and developed to include the primary features at in-plane tension failure of paper, i.e. the anisotropic softening and irreversibility, Fig. 1.2. Features which are important but not critical

include the decrease in the unloading stiffness during softening, Fig. 1.2, and the time dependent behavior. The ascending part of the load-elongation relation investigated in Chapter 2 must in general be constitutively modelled as an anisotropic elastic-plastic solid, cf. [50].

4.3.2 In-plane orthotropic smeared crack model

The fracture energy dissipation investigated in Chapter 2 was shown to be uniquely related to a monotone descending stress-crack widening relation. But the constitutive material relation in a smeared crack finite element formulation must be expressed in a stress-strain relation. The stress-crack widening relation is usually rewritten as a stress-crack strain relation. To obtain mesh objectivity for the anisotropic in-plane failure, the size of the finite elements is considered in the smeared crack constitutive model approach adopted, cf. [25, 42]. The crack strain rate vector, $\dot{\boldsymbol{\epsilon}}^f$, is defined as the mean strain rate caused by fracture in the region that includes the localized damage [42]. In reference [39] an equivalent length, L_e, is defined as the square root of the integration point area in the element. This definition of the equivalent length entails restrictions on the shape of the element, i.e. the elements in the model shall be close to rectangular and their aspect ratios shall be low, [39]. The model will otherwise provide different results if different mesh shapes are used, cf. [39]. In the smeared constitutive theory the failure event is assumed to occur along a fracture plane inside the element. The orientation of this localized damage zone is essential for the smeared properties of the element, and has therefore to be calculated. In higher order theories this is not the case since the localization damage zone is smeared over several elements, cf. [78, 94].

At initiation of the localized damage zone a crack plane is developed inside the element, cf. Fig. 4.3. It is assumed that the crack plane in the element divides the element into two halves and that the halves translate rigidly along the crack plane, cf. Fig. 4.3. In Fig. 4.3 a local coordinate system in the crack plane is given, where the n-direction denotes the normal direction to the crack plane and the t-direction denotes the tangential direction to the crack plane. The shear widening rate along the tangential direction, $\dot{w}_t$, is defined to give a smeared shear crack strain rate in the element in the tangential direction as $\dot{\epsilon}_6^{\prime f} = {L_e}^{-1}\dot{w}_t$. The widening rate in the normal direction to the crack plane, $\dot{w}_n$, is defined to give the smeared crack strain rate in the normal direction as $\dot{\epsilon}_2^{\prime f} = {L_e}^{-1}\dot{w}_n$. The crack strain rate in the tangential direction is defined to be equal to zero, i.e. $\dot{\epsilon}_1^{\prime f} = 0$. So, the smeared crack strain rate vector in the crack plane, $\dot{\boldsymbol{\epsilon}}^{\prime f}$, is defined as the crack widening rate vector in the crack plane, $\dot{\mathbf{w}}'$, smeared over a single equivalent length, L_e, cf. [39], i.e.

$$\dot{\boldsymbol{\epsilon}}^{\prime f} = {L_e}^{-1}\dot{\mathbf{w}}' \tag{4.24}$$

where $\dot{\boldsymbol{\epsilon}}^{\prime f} = \left(\dot{\epsilon}_1^{\prime f}, \dot{\epsilon}_2^{\prime f}, \dot{\epsilon}_3^{\prime f}, \dot{\epsilon}_6^{\prime f}\right)^T$ and $\dot{\mathbf{w}}' = (0, \dot{w}_n, 0, \dot{w}_t)^T$.

The smeared crack strain rate vector in the crack plane, $\dot{\boldsymbol{\epsilon}}^{\prime f}$, is transformed with the matrix, $\mathbf{R}$, into the smeared crack strain rate vector in the principal material

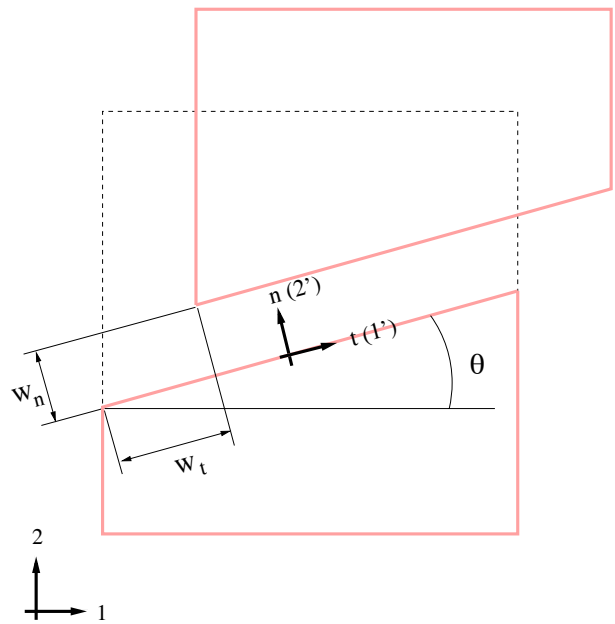

Figure 4.3: *The crack plane at the shear widening, w_t, and widening, w_n.*

direction, $\dot{\boldsymbol{\epsilon}}^f$, as cf. [17],

$$\dot{\boldsymbol{\epsilon}}^f = \mathbf{R}\dot{\boldsymbol{\epsilon}}'^f \tag{4.25}$$

where $\dot{\boldsymbol{\epsilon}}^f = \left(\dot{\epsilon}_1^f, \dot{\epsilon}_2^f, \dot{\epsilon}_3^f, \dot{\epsilon}_6^f\right)^T$. The transformation matrix, $\mathbf{R}$, is expressed in the crack plane angle, θ, cf. Fig. 4.3, as

$$\mathbf{R}^T = \begin{bmatrix} \cos^2(\theta) & \sin^2(\theta) & 0 & 2\sin(\theta)\cos(\theta) \\ \sin^2(\theta) & \cos^2(\theta) & 0 & -2\sin(\theta)\cos(\theta) \\ 0 & 0 & 1 & 0 \\ -\sin(\theta)\cos(\theta) & \sin(\theta)\cos(\theta) & 0 & \left(\cos^2(\theta) - \sin^2(\theta)\right) \end{bmatrix}$$

The relation between the smeared crack strain rate vector in the principal material direction, $\dot{\boldsymbol{\epsilon}}^f$, and crack widening rate vector in the crack plane, $\dot{\mathbf{w}}'$, is obtained from Eqs. (4.24) and (4.25) as

$$\dot{\boldsymbol{\epsilon}}^f = {L_e}^{-1}\mathbf{R}\dot{\mathbf{w}}' = {L_e}^{-1}\dot{\mathbf{w}} \tag{4.26}$$

where $\mathbf{R}\dot{\mathbf{w}}' = \dot{\mathbf{w}} = (\dot{w}_1, \dot{w}_2, \dot{w}_3, \dot{w}_6)^T$ is the crack widening rate vector in the principal material direction.

The definition in Eq. (4.24) means that the results become objective with respect to the mesh size. The equivalent length is a purely geometrical quantity determined by the size and shape of the element. However, other definitions of the equivalent lengths exist, cf. [25].

The total strain rate vector, $\dot{\boldsymbol{\epsilon}} = (\dot{\epsilon}_1, \dot{\epsilon}_2, \dot{\epsilon}_3, \dot{\epsilon}_6)^T$, is assumed to be the sum of the elastic strain and the smeared crack strain defined in Eq. (4.26), as

$$\dot{\boldsymbol{\epsilon}} = \dot{\boldsymbol{\epsilon}}^e + \dot{\boldsymbol{\epsilon}}^f \tag{4.27}$$

The derivation of the relation between the strain rate and the stress rate will be given and discussed in detail in the following subsections.

4.3.3 Fracture energy concept

The fracture energy rate, $\dot{G}_f$, for the in-plane crack plane in Fig. 4.3 is the sum of the fracture energy rate in the normal direction (mode I), $\dot{G}'_{f_1}$, and the tangential direction (mode II), $\dot{G}'_{f_2}$, i.e.

$$\dot{G}_f = \dot{G}'_{f_1} + \dot{G}'_{f_2} \tag{4.28}$$

Hillerborg et al., [42], stated that the rate of the fracture energy is the sum of the product of the uniaxial failure stresses and the crack widenings, cf. Eq. (2.5) in Chapter 2. So, Eq. (4.28) becomes equal to

$$\dot{G}_f = \sigma'_1 \dot{w}'_1 + \sigma'_2 \dot{w}'_2 = \boldsymbol{\sigma}'^T \dot{\mathbf{w}}' \tag{4.29}$$

since $\dot{\mathbf{w}}' = (0, \dot{w}_n, 0, \dot{w}_t)^T$. In Eq. (4.29) $\boldsymbol{\sigma}' = (\sigma'_1, \sigma'_2, \sigma'_3, \sigma'_6)^T$ are the stresses in the crack plane direction.

The fracture energy rate in Eq. (4.29) is expressed in the stresses and the crack widenings in the crack plane direction. To express the fracture energy rate in the stresses and the crack widenings in the principal material direction, a transformation has to be made. The stress, $\boldsymbol{\sigma}$, and crack widening rate, $\dot{\mathbf{w}}$, in the principal material direction are obtained if the stress $\boldsymbol{\sigma}'$, and crack widening rate, $\dot{\mathbf{w}}'$, in the crack plane direction are transformed with the transformation matrix, $\mathbf{R}$, i.e. $\boldsymbol{\sigma}' = \mathbf{R}^T\boldsymbol{\sigma}$ and $\dot{\mathbf{w}} = \mathbf{R}\dot{\mathbf{w}}'$, cf. [17]. The fracture energy rate in terms of the stresses and the crack widenings rate in the principal material direction is then given by

$$\dot{G}_f = \boldsymbol{\sigma}'^T \dot{\mathbf{w}}' = \left(\mathbf{R}^T\boldsymbol{\sigma}\right)^T \left(\mathbf{R}^{-1}\dot{\mathbf{w}}\right) = \boldsymbol{\sigma}^T \mathbf{R}\mathbf{R}^{-1}\dot{\mathbf{w}} = \boldsymbol{\sigma}^T \dot{\mathbf{w}} \tag{4.30}$$

The dissipation of the fracture energy rate is assumed to be equal to or greater than zero, i.e.

$$\boldsymbol{\sigma}^T \dot{\mathbf{w}} - \sigma_f \dot{w}_f \geq 0 \tag{4.31}$$

where $\dot{w}_f$ is an internal state variable whose associated variable is the equibiaxial failure stress σ_f. Insertion of the smeared crack strain-crack widening relation, Eq. (4.26), into the dissipation inequality (4.31) gives

$$\boldsymbol{\sigma}^T \dot{\boldsymbol{\epsilon}}^f - \sigma_f \dot{\epsilon}^f_f \geq 0 \tag{4.32}$$

where $\dot{\epsilon}^f_f = \dot{w}_f / L_e$ is an internal state variable. The in-plane equibiaxial failure stress rate and the equibiaxial crack strain are assumed to satisfy the following constitutive relation, cf. Eq. (2.12),

$$\dot{\sigma}_f = N_f(w_f)\dot{w}_f = L_e N_f(w_f)\dot{\epsilon}^f_f = H_f \dot{\epsilon}^f_f \tag{4.33}$$

where $N_f = N_f(w_f)$ is the slope of the equibiaxial stress-widening curve and H_f is here called the general failure modulus. The general failure modulus is discussed in Section 4.3.8.

4.3.4 Stress rate vs. crack widening rate relation

In Chapter 2 it is shown that the uniaxial stress rate vs. the crack widening rate is uniquely given by a constitutive relation as is shown in Eq. (2.12). From experiments presented in Chapter 3 it is also shown that the stress-crack widening curves in the MD and CD have different shapes. From the observation in Chapter 3 the stress rate vs. the crack widening rate constitutive relation in the MD is given by

$$\dot{\sigma}_1 = N_{11}(w_1)\dot{w}_1 \tag{4.34}$$

and in the CD by

$$\dot{\sigma}_2 = N_{22}(w_2)\dot{w}_2 \tag{4.35}$$

where N_{11} and N_{22} are here called the cohesive moduli in the MD and CD, respectively. Also, the shear stress is assumed to decrease during tensile loading in the MD or the CD due to the development of damage in the damage crack band. It is then assumed, if loading in the MD, the shear stress rate vs. the widening rate in the MD is

$$\dot{\sigma}_6 = N_{61}(w_1)\dot{w}_1 \tag{4.36}$$

and, if loading in the CD, the shear stress rate vs. the widening rate in the CD is

$$\dot{\sigma}_6 = N_{62}(w_2)\dot{w}_2 \tag{4.37}$$

where N_{61} and N_{62} are here called the cohesive shear moduli.

If pure shear loading is applied, it is assumed that the shear stress rate-crack widening rate constitutive relation is given by

$$\dot{\sigma}_6 = N_{66}(w_1, w_2)\dot{w}_6 \tag{4.38}$$

where N_{66} is cohesive shear modulus, estimated from the MD and CD cohesive moduli as

$$N_{66}(w_1, w_2) = -\frac{\sqrt{N_{11}(w_1)N_{22}(w_2)}}{2} \tag{4.39}$$

It is assumed that the base can be traced back to the estimate made for the shear elastic moduli, $G_6 = \sqrt{E_1E_2}/(1+\sqrt{\nu_{12}\nu_{21}})/2$, cf. [7, 55]. The shear elastic modulus estimate, combined with the observation that the failure potential produces a Poisson's ratio equal to zero during the development of localized damage, gives Eq. (4.39).

During shear loading it is also assumed that not only the shear stress decreases but also the tensile stresses, σ_1 and σ_2, decrease according to the following constitutive relation

$$\dot{\sigma}_1 = N_{16}(w_6)\dot{w}_6 \tag{4.40}$$

and

$$\dot{\sigma}_2 = N_{26}(w_6)\dot{w}_6 \tag{4.41}$$

where N_{16} and N_{26} are here called the cohesive shear moduli.

The stress rate vs. the crack widening rate constitutive relations in Eqs. (4.34)-(4.41) are given in matrix form as

$$\dot{\boldsymbol{\sigma}} = \mathbf{N}\dot{\mathbf{w}} \tag{4.42}$$

where $\mathbf{N}$ is here called the cohesive modulus matrix and is given as

$$\mathbf{N} = \begin{bmatrix} N_{11} & 0 & 0 & N_{16} \\ 0 & N_{22} & 0 & N_{26} \\ 0 & 0 & 0 & 0 \\ N_{61} & N_{62} & 0 & N_{66} \end{bmatrix} \tag{4.43}$$

Only the diagonal components $N_{11}(w_1)$ and $N_{22}(w_2)$ in the cohesive modulus matrix, $\mathbf{N}$, were studied in the experiments presented in Chapter 3. In the next chapters it is assumed that the off-diagonal components are zero, i.e. $N_{16} = N_{26} = N_{61} = N_{62} = 0$. This assumption may seem crude; however, the numerical applications in the next chapters related to papers are loaded in the MD or the CD, which suggests that the diagonal components $N_{11}(w_1)$ and $N_{22}(w_2)$ in the cohesive modulus matrix dominate. Also, from experimental observations of tensile loading in the MD or the CD, the damage crack band develops perpendicular to the loading direction, and hence it seems reasonable to assume that the diagonal components in the cohesive modulus matrix dominate.

4.3.5 The failure criterion

The smeared crack strain is assumed to occur only when the stress state reaches the failure strength; this corresponds to the satisfaction of some failure criterion $\Phi = 0$. Failure criteria describing in-plane loading condition at failure have been described for paper sheets in the literature, cf. [79, 100]. Here the failure criterion for in-plane failure of paper proposed in [100] will be used. The initial shape of the failure surface can be regarded as a modification of a yield surface reported in [41]. The advantage of this failure criterion (called the Hill-Tsai-Wu failure criterion in [100]) over the Tsai-Wu criterion is due to the fact that it more accurately fits the experimental biaxial failure stress envelop. Furthermore, the Hill-Tsai-Wu failure criterion is capable of capturing both the variation in the failure strength and the variation in the plastic straining at failure, whereas the Tsai-Wu criterion is limited to predict one or the other.

The failure criterion in [100] for plane stress is expressed in the effective stress, σ_e, (defined below) and the equibiaxial failure stress, σ_f, as

$$\Phi(\boldsymbol{\sigma}, \sigma_f) = \sigma_e(\sigma_1, \sigma_2, \sigma_6) - \sigma_f(\epsilon_f^f),\ \Phi \leq 0 \tag{4.44}$$

where $\Phi = 0$ at development of failure.

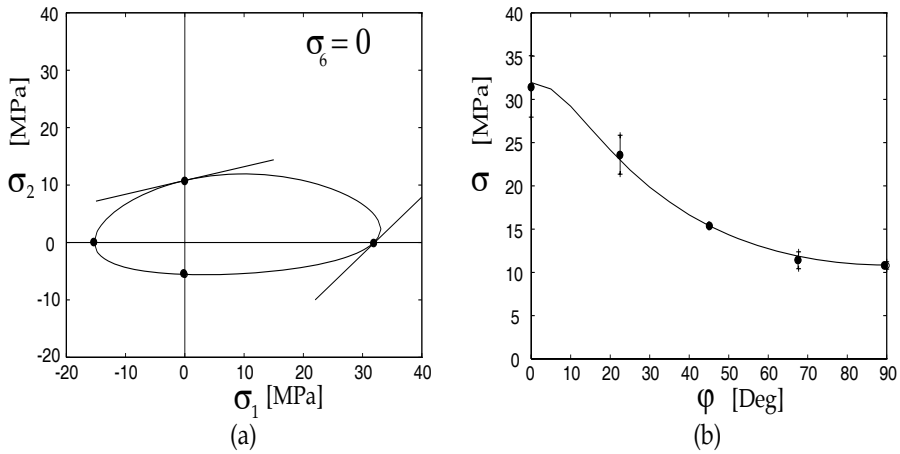

Figure 4.4: *(a) The failure criterion for newsprint. (b) The uniaxial tensile strength at different material directions for newsprint.*

The effective stress, σ_e, in Eq. (4.44) is a function of the in-plane stresses. It is assumed that no in-plane loading can cause any out-of-plane failure, and vice versa. This means that no coupling terms are allowed to exist between the in-plane and the out-of-plane stresses, i.e. no $\sigma_1\sigma_3$ and $\sigma_2\sigma_3$ terms in the effective stress function. From the failure criterion for in-plane failure in [100], the effective stress is defined as

$$\sigma_e = \sqrt{R_{11}\sigma_1^2 + 2\left(\varsigma Q_{12} + R_{12}\right)\sigma_1\sigma_2 + R_{22}\sigma_2^2 + R_{66}\sigma_6^2 + S_{11}\sigma_1 + S_{22}\sigma_2} \tag{4.45}$$

where $\varsigma = p\left(1 - \sigma_1/P\right) + q\left(1 - \sigma_2/P\right)$ is a non-dimensional function of the in-plane stresses σ_1 and σ_2. P is the equibiaxial tensile strength, i.e. the magnitude of the failure strength for the stress state $\sigma_1 = \sigma_2 > 0$, $\sigma_6 = 0$ and $\sigma_3 = 0$. The other parameters

$$\begin{aligned}
R_{11} &= P^2(T_1C_1)^{-1} \\
Q_{12} &= \frac{1}{2}P^2(T_1T_2)^{-1} \\
R_{12} &= \frac{1}{2}\left\{1 - P(T_1^{-1} - C_1^{-1} + T_1^{-1} - C_1^{-1}) - P^2\left[(T_1C_1)^{-1} + (T_2C_2)^{-1}\right]\right\} \\
R_{22} &= P^2(T_2C_2)^{-1} \\
R_{66} &= P^2T_6^{-2} \\
S_{11} &= P^2(T_1^{-1} - C_1^{-1}) \\
S_{22} &= P^2(T_2^{-1} - C_2^{-1})
\end{aligned}$$

are constants in Eq. (4.45) and T_1, T_2 and T_6 are the MD strength in tension, the CD strength in tension and the shear strength, respectively, whereas C_1 and C_2 are

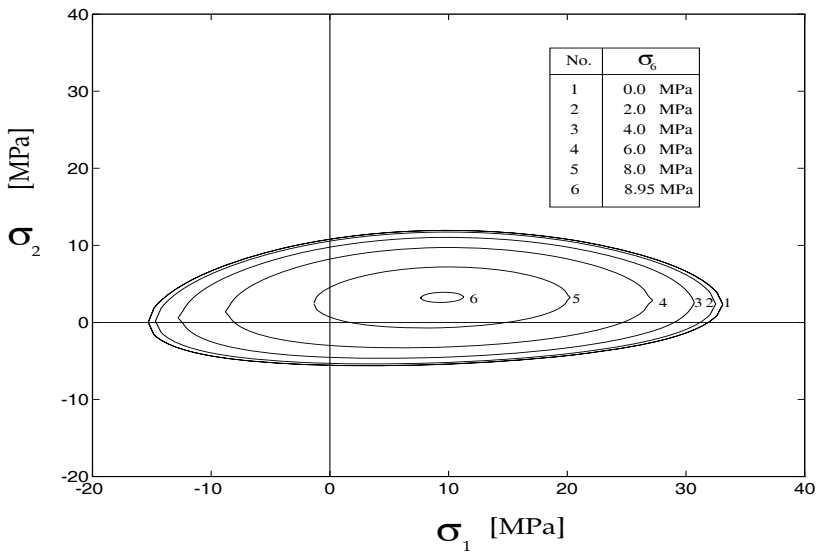

Figure 4.5: *The initial failure criterion for newsprint plotted at different shear stress values.*

the MD and CD compression strengths. The non-dimensional parameters p and q in ς are given in [100] as

$$
\begin{aligned}
p &= \left(\frac{P}{T_1}+\frac{P}{T_2}-1\right)^{-1}\left[\nu_{12}^f\left(1-\frac{T_2}{P}\right)\left(\frac{S_{11}}{T_1}+2R_{11}\right)-\nu_{21}^f\left(\frac{S_{22}}{T_2}+2R_{22}\right)\right.\\
&\quad\left.+\left(\frac{S_{22}}{T_1}-\frac{S_{11}}{T_2}\right)-\frac{T_2}{P}\left(\frac{S_{22}}{T_1}+2R_{12}\right)\right]\\
q &= \left(\frac{P}{T_1}+\frac{P}{T_2}-1\right)^{-1}\left[\nu_{21}^f\left(1-\frac{T_1}{P}\right)\left(\frac{S_{22}}{T_2}+2R_{22}\right)-\nu_{12}^f\left(\frac{S_{11}}{T_1}+2R_{11}\right)\right.\\
&\quad\left.+\left(\frac{S_{11}}{T_2}-\frac{S_{22}}{T_1}\right)-\frac{T_1}{P}\left(\frac{S_{11}}{T_2}+2R_{12}\right)\right] \qquad (4.46)
\end{aligned}
$$

where ν_{12}^f and ν_{21}^f are the failure Poisson's ratios.

Karafillis et al. [50] have shown that associated plasticity is able to describe the anisotropic elastic-plastic in-plane hardening behavior of paperboard 240 g/m^2. This observation means that the in-plane plastic Poisson's ratios, i.e. $\nu_{12}^p = -d\epsilon_2^p/d\epsilon_1^p$ with $\sigma_1 > 0$ and $\nu_{21}^p = -d\epsilon_1^p/d\epsilon_2^p$ with $\sigma_2 > 0$, at rupture are equal to the failure Poisson's ratios, ν_{12}^f and ν_{21}^f, cf. [100], i.e. $\lim_{\epsilon_1\to\epsilon_1^f}\nu_{12}^p = \nu_{12}^f$ and $\lim_{\epsilon_2\to\epsilon_2^f}\nu_{21}^p = \nu_{21}^f$. During continuously stable failure, the plastic Poisson's ratios are assumed to change with the failure strength. At re-loading the failure Poisson's ratios are set equal to the plastic Poisson's ratios.

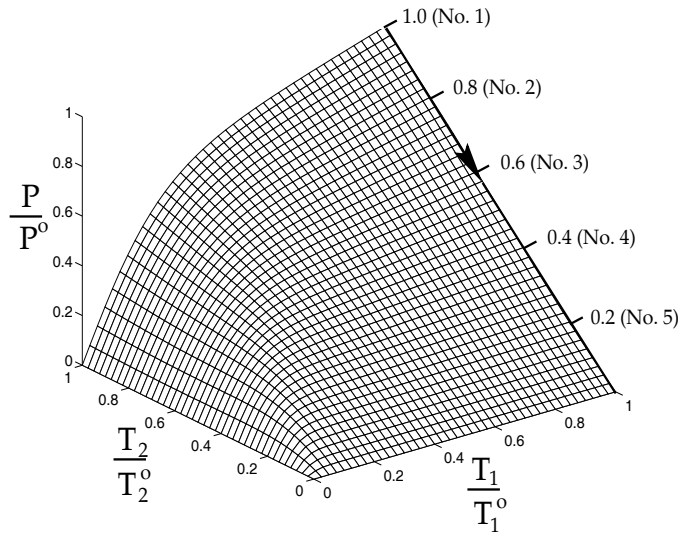

Figure 4.6: *Relation between the equibiaxial strength and the uniaxial strengths determined for newsprint and fulfilling the convexity requirement.*

In Fig. 4.4(a) the failure criterion with experimental strength values given in the next chapter (Table 5.3) is plotted as circles, ●, and the failure Poisson's ratios as tangents to the failure criterion curve. The shear stress is equal to zero, i.e. $\sigma_6 = 0$. The uniaxial tensile strength, given by the failure criterion at different material directions, is plotted in Fig. 4.4(b) together with experimentally obtained strength parameters (●). Note that the error bars indicate the standard deviations of the measured strength values.

The failure criterion at different shear stresses is given by Fig. 4.5. In Fig. 4.5 it is shown that the maximum shear stress σ_6 is ≈ 9 MPa when $\sigma_1 \approx 3.4$ MPa and $\sigma_2 \approx 9.4$ MPa. I.e. the maximum shear stress is not obtained from a pure shear test, i.e. when $\sigma_1 = \sigma_2 = 0$.

It is required that the relation between the equibiaxial failure strength, P, and the failure strengths in the principal material axes, T_1 and T_2, ensures that the failure criterion, $\Phi = 0$, is convex throughout the localized failure process. The relation between the equibiaxial failure strength, P, and the failure strengths, T_1 and T_2, is

$$\frac{P}{P^o} = \Gamma\left(\frac{T_1}{T_1^o}, \frac{T_2}{T_2^o}\right) = \gamma_1\left(\frac{T_2}{T_2^o}\right)\tanh\left[\gamma_2\left(\frac{T_2}{T_2^o}\right)\frac{T_1}{T_1^o}\right] + \gamma_3\left(\frac{T_2}{T_2^o}\right)\frac{T_1}{T_1^o} \tag{4.47}$$

where

$$\gamma_1\left(\frac{T_2}{T_2^o}\right) = \gamma_{11}\left(1 - \gamma_{12}\frac{T_2}{T_2^o}\right)\left(\frac{T_2}{T_2^o}\right)^2 + \gamma_{13}\left(\frac{T_2}{T_2^o}\right)$$

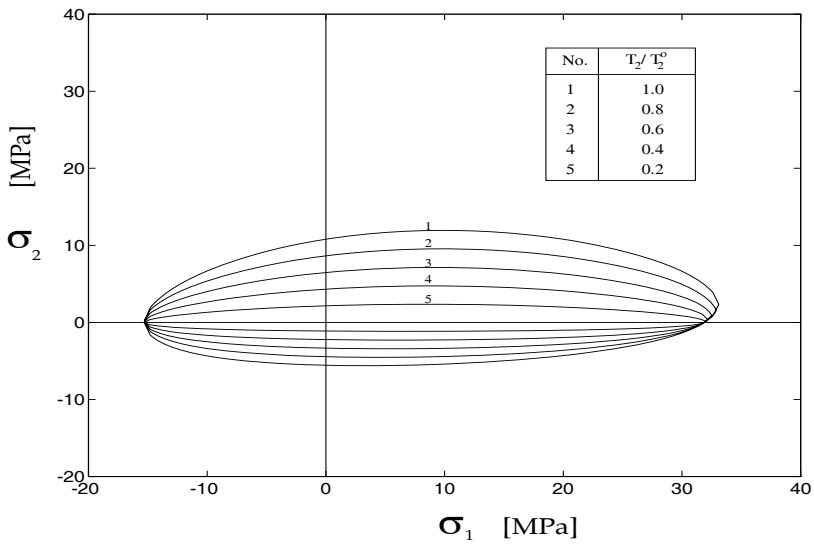

Figure 4.7: *The failure criterion at different tensile strength T_2 values; the shear stress is equal to zero, i.e. $\sigma_6 = 0$.*

$$\begin{aligned}
\gamma_2\left(\frac{T_2}{T_2^o}\right) &= \gamma_{21}\exp\left(-\gamma_{22}\frac{T_2}{T_2^o}\right)+\gamma_{23} \\
\gamma_3\left(\frac{T_2}{T_2^o}\right) &= \gamma_{31}\left(1-\gamma_{32}\frac{T_2}{T_2^o}\right)\left(\frac{T_2}{T_2^o}\right)^2+\gamma_{33}\left(\frac{T_2}{T_2^o}\right)
\end{aligned}$$

and T_1^o, T_2^o, P^o are the initial MD, CD tensile and equibiaxial failure strengths, respectively. Together with the assumption that the compressive strengths and failure Poisson's ratios are decreasing proportionally as

$$C_1 = \frac{C_1^o}{T_1^o}T_1 \text{ and } \nu_{12}^f = \frac{\nu_{12}^{fo}}{T_1^o}T_1 \tag{4.48}$$

and

$$C_2 = \frac{C_2^o}{T_2^o}T_2 \text{ and } \nu_{21}^f = \frac{\nu_{21}^{fo}}{T_2^o}T_2 \tag{4.49}$$

where C_1^o, ν_{12}^{fo} and C_2^o, ν_{21}^{fo} is the initial compressive and failure Poisson ratio in the MD and CD, respectively, this ensures that the failure criterion is convex throughout the localized failure process. The function Γ, in Eq. (4.47), is a descending function of descending values of the failure stresses T_1 and T_2, cf. Fig. 4.6. The anisotropic failure constants γ_{ij} where $i = 1,2,3$ and $j = 1,2,3$ are given in Table 5.3 for newsprint.

The decreasing size of the failure criterion, due to the above rules, for uniaxial decrease in the CD is shown in Figs. 4.6 and 4.7. It is seen that T_2 and P are decreasing but the strength in the MD is not affected by the decrease, i.e. $T_1 = T_1^o$. The reason for this is that the cohesive crack or damage crack band is parallel to MD. If subsequently the paper is loaded in MD, a cohesive crack is allowed to develop perpendicular to the first crack.

4.3.6 Evolution laws

In analogy to associated plasticity theory formulations, which fulfill the postulate of maximum dissipation, the evolution laws for the $\dot{\boldsymbol{\epsilon}}^f$ and $\dot{\epsilon}_f^f$ are assumed to follow flow rules of the form

$$\dot{\boldsymbol{\epsilon}}^f = \dot{\lambda}_f \frac{\partial \Phi}{\partial \boldsymbol{\sigma}} \quad \text{and } \dot{\epsilon}_f^f = -\dot{\lambda}_f \frac{\partial \Phi}{\partial \sigma_f} \tag{4.50}$$

where $\dot{\lambda}_f$, here called the smeared crack multiplier, and the failure criterion, Φ, fulfill the Kuhn-Tucker relations,

$$\Phi \leq 0, \; \dot{\lambda}_f \Phi = 0 \text{ and } \dot{\lambda}_f \geq 0 \tag{4.51}$$

the function Φ being convex and smooth.

In experiments performed by de Ruvo et al. [79], a tube is axially loaded together with internal pressure to give three different stress ratios, 20, 1 and 0.1, between the MD and CD. It is observed that with a stress ratio of 20, the fracture path is perpendicular to the MD and at a stress ratio of 1 the fracture path is equally developed in the MD and CD. For a stress ratio of 0.1 the fracture path is perpendicular to the CD.

The results from an experimental investigation in Chapter 3 of long paper strips[1], uniaxially loaded and cut in $\varphi = 0$, 22.5, 45, 67.5 and 90 degrees with respect to the MD, suggest that the fracture section orients itself near to the principal directions of the paper.

But the failure criteria in Eq. (4.44) as a failure potential cannot predict the crack path experimentally observed. For example, at uniaxial loading the prediction of failure strain direction from the failure surface in Eq. (4.50) gives that $\dot{\epsilon}_1^f = \dot{\lambda}_f \partial\Phi/\partial\sigma_1 \neq 0$ and $\dot{\epsilon}_2^f = \dot{\lambda}_f \partial\Phi/\partial\sigma_2 \neq 0$. However, the experiments in Chapter 3 (Table 3.2) and [79] show that for loading the MD shall $\dot{\epsilon}_1^f \neq 0$ and $\dot{\epsilon}_2^f = 0$ and for loading the CD shall $\dot{\epsilon}_1^f = 0$ and $\dot{\epsilon}_2^f \neq 0$. This means that the evolution law in Eq. (4.50) has to be expressed with a failure potential that is independent of the failure criterion.

It is possible to generalize the evolution laws in Eq. (4.50) as, cf. [61],

$$\dot{\boldsymbol{\epsilon}}^f = \dot{\lambda}_f \frac{\partial \Psi}{\partial \boldsymbol{\sigma}} \quad \text{and } \dot{\epsilon}_f^f = -\dot{\lambda}_f \frac{\partial \Psi}{\partial \sigma_f} \tag{4.52}$$

[1] Newsprint 45 g/m^2, kraft paper 70 g/m^2 and paperboard 120 g/m^2.

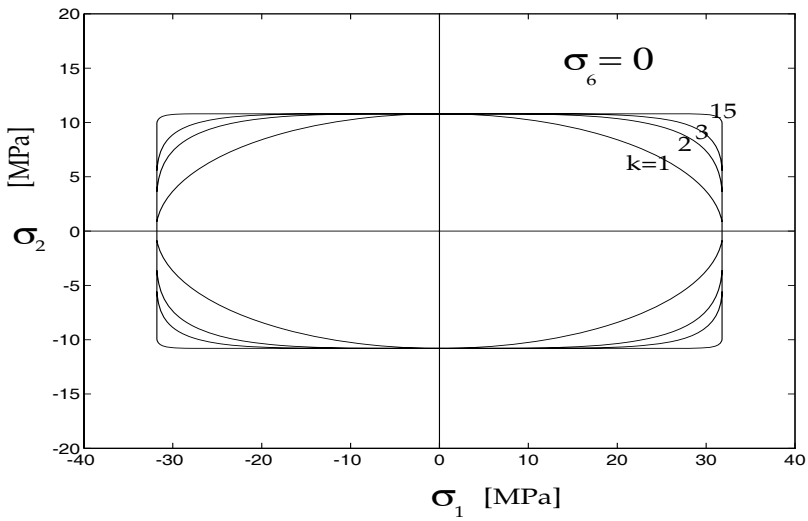

Figure 4.8: *Plot of the failure potential for the shear stress equal to zero, at different values of the positive integer, k, namely $k = 1, 2, 3, 15$.*

where the function$\Psi = \Psi(\boldsymbol{\sigma}, \sigma_f)$ is a failure potential that differs from the failure criterion function. The failure potential is required to be convex and smooth in the stress space.

4.3.7 The failure potential

A failure potential

$$\Psi = \sigma_\psi(\sigma_1, \sigma_2, \sigma_6) - \sigma_f(\epsilon_f^f) \tag{4.53}$$

is seen to be able to describe the in-plane tension fracture path for paper based on experimental observation. In Eq. (4.53) σ_ψ the effective stress potential is defined by

$$\sigma_\psi = \left[\left(\frac{P}{T_1}\right)^{2k} \sigma_1^{2k} + \left(\frac{P}{T_2}\right)^{2k} \sigma_2^{2k} + \left(\frac{P}{T_6}\right)^{2k} \sigma_6^{2k} \right]^{1/(2k)} \tag{4.54}$$

and σ_f is the biaxial failure stress. In Eq. (4.54), k is a positive integer with a value varying from $+1$ to $+\infty$. The exponent in Eq. (4.54) is always an even integer, thereby ensuring equality at tension and compression stress. When $k = 1$ the failure potential describes an ellipsoid in the stress space, whereas $k \to \infty$ corresponds to a box in the stress space, see Fig. 4.8. A box shape of the failure potential means that the failure plane during biaxial loading always develops in one of the principal

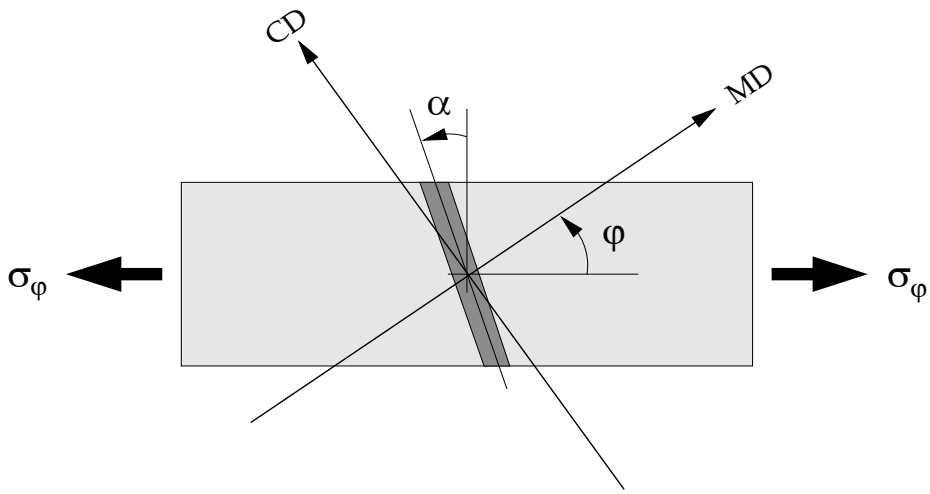

Figure 4.9: *Crack direction, α, (thick dark grey line) due to load at different cut directions, φ.*

	Newsprint	k=1	k=2	k=15
φ	α	α	α	α
0°	0°	0°	0°	0°
22.5°	19° to 32°	8°	18°	22.5°
45°	30° to 42°	17°	30°	45°
67.5°	−25° to −11°	−47°	−25.5°	−22.5°
90°	0°	0°	0°	0°

Table 4.2: *The directional orientation of the damage band. The definitions of the angles α and φ are found in Fig. 4.9*

axes of the material. Figure 4.8 shows the failure potential for various k values from $+1$ to $+\infty$. It is seen that a smooth box shape is obtained for $k \geq 2$.

The failure potential has been calibrated with experimental data from the newsprint 45 g/m^2. Table 4.2 shows the deviations in degrees from crack path for different k in the failure potential compared to the experimental data of the crack path at different cut directions, i.e. $\varphi = 0$, 22.5, 45, 67.5 and 90 degrees, cf. Fig. 4.9.

Note that the failure potential in Eq. (4.53) is developed to describe only the in-plane tension crack path, not the strain localization due to in-plane compression stresses. So the orientation of a possible strain localization band due to in-plane compression is left open for further studies and discussion.

4.3.8 Continuum stiffness matrix

If fracture loading is occurring, we require that the criterion $\Phi = 0$ is continuously satisfied. This means that the consistency equation, $\dot{\Phi} = 0$, has to be fulfilled, i.e. from Eq. (4.44) we have that

$$\dot{\Phi} = \dot{\sigma}_e - \dot{\sigma}_f = 0 \tag{4.55}$$

where $\dot{\sigma}_f$ is the equibiaxial failure stress rate. Hence by Eqs. (4.52)b and (4.53) inserted into Eq. (4.33), the equibiaxial failure stress is given by

$$\dot{\sigma}_f = H_f \dot{\epsilon}_f^f = -H_f \dot{\lambda}_f \frac{\partial \Psi}{\partial \sigma_f} = H_f \dot{\lambda}_f \tag{4.56}$$

Combination of Eqs. (4.55) and (4.56) gives the effective stress rate vs. the smeared crack multiplier relation as

$$\dot{\sigma}_e = H_f \dot{\lambda}_f \tag{4.57}$$

The effective stress, σ_e, is a function of the stress vector, $\boldsymbol{\sigma}$, i.e. $\sigma_e(\boldsymbol{\sigma})$. So, the effective stress rate, $\dot{\sigma}_e$, is given as

$$\dot{\sigma}_e = \left(\frac{\partial \sigma_e}{\partial \boldsymbol{\sigma}}\right)^T \dot{\boldsymbol{\sigma}} \tag{4.58}$$

In Eq. (4.44) is $\Phi(\boldsymbol{\sigma}, \sigma_f) = \sigma_e(\boldsymbol{\sigma}) - \sigma_f$. Differentation of Eq. (4.44) with respect to the stress vector, $\boldsymbol{\sigma}$, gives

$$\frac{\partial \Phi}{\partial \boldsymbol{\sigma}} = \frac{\partial \sigma_e}{\partial \boldsymbol{\sigma}} \tag{4.59}$$

Insertion of Eq. (4.59) into Eq. (4.58) gives the effective stress rate as

$$\dot{\sigma}_e = \left(\frac{\partial \Phi}{\partial \boldsymbol{\sigma}}\right)^T \dot{\boldsymbol{\sigma}} \tag{4.60}$$

Insertion of the smeared crack strain rate vs. crack widening rate, Eq. (4.26), together with the evolution law, Eq. (4.52)a, into the stress rate vs. crack widening relation rate, Eq. (4.42), and thereafter insertion of this into Eq. (4.60) shows that the effective stress rate becomes equal to

$$\dot{\sigma}_e = L_e \left(\frac{\partial \Phi}{\partial \boldsymbol{\sigma}}\right)^T \mathbf{N} \frac{\partial \Psi}{\partial \boldsymbol{\sigma}} \dot{\lambda}_f \tag{4.61}$$

Comparison with Eq. (4.57) shows that the general failure modulus, H_f, is expressed in the cohesive modulus matrix, $\mathbf{N}$, as

$$H_f = L_e \left(\frac{\partial \Phi}{\partial \boldsymbol{\sigma}}\right)^T \mathbf{N} \frac{\partial \Psi}{\partial \boldsymbol{\sigma}} \tag{4.62}$$

Insertion of Eq. (4.1), (4.27) and (4.52)a into Eq. (4.60) gives that the effective stress is expressed into the total strain rate and the smeared crack multiplier relation as

$$\dot{\sigma}_e = \left(\frac{\partial \Phi}{\partial \boldsymbol{\sigma}}\right)^T \mathbf{D}\dot{\boldsymbol{\epsilon}}^e = \left(\frac{\partial \Phi}{\partial \boldsymbol{\sigma}}\right)^T \mathbf{D}\left(\dot{\boldsymbol{\epsilon}} - \dot{\boldsymbol{\epsilon}}^f\right) = \left(\frac{\partial \Phi}{\partial \boldsymbol{\sigma}}\right)^T \mathbf{D}\left(\dot{\boldsymbol{\epsilon}} - \dot{\lambda}_f \frac{\partial \Psi}{\partial \boldsymbol{\sigma}}\right) \tag{4.63}$$

Combination of Eq. (4.57) and Eq. (4.63) gives that the smeared crack multiplier is related to the total strain rate as

$$\dot{\lambda}_f = \frac{1}{A_f}\left(\frac{\partial \Phi}{\partial \boldsymbol{\sigma}}\right)^T \mathbf{D}\dot{\boldsymbol{\epsilon}} \tag{4.64}$$

where A_f is a positive scalar given by

$$A_f = \left(\frac{\partial \Phi}{\partial \boldsymbol{\sigma}}\right)^T \mathbf{D}\frac{\partial \Psi}{\partial \boldsymbol{\sigma}} + H_f \tag{4.65}$$

The continuum stiffness matrix that relates the stress rate to the total strain rate is obtained from insertion of Eqs. (4.27), (4.52)a and (4.64) into (4.1), as

$$\dot{\boldsymbol{\sigma}} = \mathbf{D}^{ef}\dot{\boldsymbol{\epsilon}} \tag{4.66}$$

where

$$\mathbf{D}^{ef} = \mathbf{D} - \frac{1}{A_f}\mathbf{D}\frac{\partial \Psi}{\partial \boldsymbol{\sigma}}\left(\frac{\partial \Phi}{\partial \boldsymbol{\sigma}}\right)^T \mathbf{D} \tag{4.67}$$

It is assumed that the out-of-plane stress is zero, i.e. $\dot{\sigma}_3 = 0$, in Eq. (4.66). This gives that Eq. (4.66) reduces to

$$\begin{aligned} \dot{\bar{\boldsymbol{\sigma}}} &= \bar{\mathbf{D}}^{ef}\dot{\bar{\boldsymbol{\epsilon}}} \\ \dot{\epsilon}_3 &= \frac{D_{13}^{ef}}{D_{33}^{ef}}\dot{\epsilon}_1 + \frac{D_{23}^{ef}}{D_{33}^{ef}}\dot{\epsilon}_2 + \frac{D_{26}^{ef}}{D_{33}^{ef}}\dot{\epsilon}_6 \end{aligned} \tag{4.68}$$

where $\dot{\bar{\boldsymbol{\sigma}}} = (\dot{\sigma}_1, \dot{\sigma}_2, \dot{\sigma}_6)^T$, $\dot{\bar{\boldsymbol{\epsilon}}} = (\dot{\epsilon}_1, \dot{\epsilon}_2, \dot{\epsilon}_6)^T$ and $\bar{\mathbf{D}}^{ef}$ is a continuum stiffness matrix for plane stress condition.

4.3.9 Tangential stiffness matrix

The continuum stiffness matrix exhibits poor convergence properties in cases were large failure strain increments occur, [64]. To obtain quadratic convergence rates at each iteration, a tangential stiffness matrix, different from the continuum stiffness matrix, and consistent with the use of the backward Euler integration scheme (i.e. a fully implicit algorithm) may be used, [91].

It is assumed that the strain rate is constant during the entire increment from time t to time $t + \Delta t$. The incremental stress and strain relation is given from combination of Eqs. (4.1) and (4.27) for the backward Euler algorithm as

$$\Delta\boldsymbol{\sigma} = \mathbf{D}\left(\Delta\boldsymbol{\epsilon} - \Delta\boldsymbol{\epsilon}^f\right) \tag{4.69}$$

where the incremental plastic strain, $\Delta\boldsymbol{\epsilon}^f$, is given from Eq. (4.52)a as

$$\Delta\boldsymbol{\epsilon}^f = \int_t^{t+\Delta t} \dot{\lambda}_f \frac{\partial\Psi}{\partial\boldsymbol{\sigma}} dt = \lambda_f \left.\frac{\partial\Psi}{\partial\boldsymbol{\sigma}}\right|_{t+\Delta t} \tag{4.70}$$

and λ_f is the smeared crack multiplier at time $t+\Delta t$, since the smeared crack multiplier at t is zero. Combination of Eqs. (4.69) and (4.70) gives

$$\Delta\boldsymbol{\sigma} = \mathbf{D}\left(\Delta\boldsymbol{\epsilon} - \lambda_f \left.\frac{\partial\Psi}{\partial\boldsymbol{\sigma}}\right|_{t+\Delta t}\right) \tag{4.71}$$

In Eq. (4.71) are the incremental stresses, $\Delta\boldsymbol{\sigma} = \boldsymbol{\sigma}_{t+\Delta t} - \boldsymbol{\sigma}_t$ and $\mathbf{D}\Delta\boldsymbol{\epsilon} = \boldsymbol{\sigma}_T - \boldsymbol{\sigma}_t$, where $\boldsymbol{\sigma}_{t+\Delta t}$ is the stress at the end of the increment step, i.e. $t+\Delta t$, $\boldsymbol{\sigma}_T$ is the test stress and $\boldsymbol{\sigma}_t$ is the current stress. Inserting this into Eq. (4.71) gives

$$\boldsymbol{\sigma}_{t+\Delta t} = \boldsymbol{\sigma}_T - \lambda_f \mathbf{D} \left.\frac{\partial\Psi}{\partial\boldsymbol{\sigma}}\right|_{t+\Delta t} \tag{4.72}$$

Rewriting Eq. (4.72) to (where the superscripts $t+\Delta t$ have been dropped for clarity)

$$\boldsymbol{\Sigma}(\boldsymbol{\sigma}, \lambda_f) = \boldsymbol{\sigma} - \boldsymbol{\sigma}_T + \lambda_f \mathbf{D}\frac{\partial\Psi}{\partial\boldsymbol{\sigma}} = 0 \tag{4.73}$$

where $\boldsymbol{\Sigma} = (\Sigma_1, \Sigma_2, \Sigma_3, \Sigma_6)^T$. In Eq. (4.73) $\boldsymbol{\Sigma}$ is a function of the stress, $\boldsymbol{\sigma}$, and the smeared crack multiplier, λ_f, at the end of the increment step. The failure criterion, Φ, in Eq. (4.44) together with the relation $\dot{\epsilon}_f^f = \dot{\lambda}_f$ (given by Eqs. (4.52)b and (4.53)) is given by

$$\Phi(\boldsymbol{\sigma}, \lambda_f) = \sigma_e(\boldsymbol{\sigma}) - \sigma_f(\epsilon_f^f) = 0 \tag{4.74}$$

A Taylor series expansion of Eqs. (4.73) and (4.74) at a Gauss point at the current iteration, n, gives

$$\begin{aligned} \boldsymbol{\Sigma}_n &= \boldsymbol{\Sigma}_{n-1} + \Delta\boldsymbol{\Sigma} = 0 \\ \Phi_n &= \Phi_{n-1} + \Delta\Phi = 0 \end{aligned} \tag{4.75}$$

where

$$\begin{aligned} \Delta\boldsymbol{\Sigma} &= \frac{\partial\boldsymbol{\Sigma}}{\partial\boldsymbol{\sigma}}(\boldsymbol{\sigma}_n - \boldsymbol{\sigma}_{n-1}) + \frac{\partial\boldsymbol{\Sigma}}{\partial\lambda_f}(\lambda_n - \lambda_{n-1}) \\ \Delta\Phi &= \left(\frac{\partial\Phi}{\partial\boldsymbol{\sigma}}\right)^T (\boldsymbol{\sigma}_n - \boldsymbol{\sigma}_{n-1}) + \frac{\partial\Phi}{\partial\lambda_f}(\lambda_n - \lambda_{n-1}) \end{aligned} \tag{4.76}$$

with

$$\begin{aligned} \frac{\partial\boldsymbol{\Sigma}}{\partial\boldsymbol{\sigma}} &= \mathbf{I} + \lambda_f \mathbf{D}\frac{\partial^2\Psi}{\partial\boldsymbol{\sigma}^2} \\ \frac{\partial\boldsymbol{\Sigma}}{\partial\lambda_f} &= \mathbf{D}\frac{\partial\Psi}{\partial\boldsymbol{\sigma}} + L_e\mathbf{N}\frac{\partial\Psi}{\partial\boldsymbol{\sigma}} \\ \frac{\partial\Phi}{\partial\boldsymbol{\sigma}} &= \frac{\partial\sigma_e}{\partial\boldsymbol{\sigma}} \\ \frac{\partial\Phi}{\partial\lambda_f} &= H_f \end{aligned} \tag{4.77}$$

In Eq. (4.77) $\mathbf{I}$ is the identity matrix and H_f is the general failure modulus, cf. Eq. (4.62).

Let us define the following matrix

$$\boldsymbol{\mathcal{M}} = \begin{bmatrix} \frac{\partial \boldsymbol{\Sigma}}{\partial \boldsymbol{\sigma}} & \frac{\partial \boldsymbol{\Sigma}}{\partial \lambda_f} \\ \left(\frac{\partial \Phi}{\partial \boldsymbol{\sigma}}\right)^T & \frac{\partial \Phi}{\partial \lambda_f} \end{bmatrix} \tag{4.78}$$

Combination of Eq. (4.75) and Eq. (4.76) with $\boldsymbol{\mathcal{M}}$ gives

$$\begin{bmatrix} \boldsymbol{\sigma}_n \\ \lambda_n \end{bmatrix} = \begin{bmatrix} \boldsymbol{\sigma}_{n-1} \\ \lambda_{n-1} \end{bmatrix} - \boldsymbol{\mathcal{M}}^{-1} \begin{bmatrix} \boldsymbol{\Sigma}_{n-1} \\ \Phi_{n-1} \end{bmatrix} \tag{4.79}$$

The stress, $\boldsymbol{\sigma}$, and the smeared crack multiplier, λ_f, at the end of the incremental step, i.e. $t+\Delta t$, are given by solving the equation system with the Newton-Raphson algorithm. At plane stress condition is $\sigma_3 = 0$ in the established Newton-Raphson scheme.

The crack widening $\mathbf{w}$ and the failure strength stresses, i.e. $\mathbf{T} = (T_1, T_2, 0, T_6)$, in the failure criteria, Φ, and the failure potential, Ψ, must be updated after the iteration, as

$$\mathbf{w}|_{t+\Delta t} = \mathbf{w}|_t + L_e \lambda_f \left.\frac{\partial \Psi}{\partial \boldsymbol{\sigma}}\right|_{t+\Delta t} \tag{4.80}$$

and

$$\mathbf{T}|_{t+\Delta t} = \mathbf{T}|_t + \mathbf{N}\Delta\mathbf{w} = \mathbf{T}|_t + L_e \lambda_f \mathbf{N}(\mathbf{w}|_t) \left.\frac{\partial \Psi}{\partial \boldsymbol{\sigma}}\right|_{t+\Delta t} \tag{4.81}$$

where we have used Eqs. (4.26), (4.42) and (4.70) to obtain (4.81).

As mentioned above, to preserve the quadratic convergence rate at each iteration, it is necessary to use the tangential stiffness matrix (Jacobian matrix). Hence we seek $\hat{\bar{\mathbf{D}}}^{ef}$ such that

$$\dot{\bar{\boldsymbol{\sigma}}} = \hat{\bar{\mathbf{D}}}^{ef} \dot{\bar{\boldsymbol{\epsilon}}} \tag{4.82}$$

where $\dot{\bar{\boldsymbol{\sigma}}} = (\dot{\sigma}_1, \dot{\sigma}_2, \dot{\sigma}_6)^T$, $\dot{\bar{\boldsymbol{\epsilon}}} = (\dot{\epsilon}_1, \dot{\epsilon}_2, \dot{\epsilon}_6)^T$ and $\hat{\bar{\mathbf{D}}}^{ef}$ is the tangential stiffness matrix.

4.3.10 Tangential stiffness components

The consistent stiffness components are given from the following derivation. Differentiation of Eq. (4.71) with respect to time gives

$$\dot{\boldsymbol{\sigma}} = \mathbf{D}\left(\dot{\boldsymbol{\epsilon}} - \dot{\lambda}_f \frac{\partial \Psi}{\partial \boldsymbol{\sigma}} - \lambda_f \frac{\partial^2 \Psi}{\partial \boldsymbol{\sigma}^2} \dot{\boldsymbol{\sigma}}\right) \tag{4.83}$$

Rearrangement of Eq. (4.83) gives

$$\dot{\boldsymbol{\sigma}} = \hat{\mathbf{D}}\left(\dot{\boldsymbol{\epsilon}} - \dot{\lambda}_f \frac{\partial \Psi}{\partial \boldsymbol{\sigma}}\right) \tag{4.84}$$

Tangential stiffness relations
$\dot{\sigma}_1 = \hat{\bar{D}}^{ef}_{11}\dot{\epsilon}^e_1 + \hat{\bar{D}}^{ef}_{12}\dot{\epsilon}^e_2 + \hat{\bar{D}}^{ef}_{16}\dot{\epsilon}^e_6$
$\dot{\sigma}_2 = \hat{\bar{D}}^{ef}_{21}\dot{\epsilon}^e_1 + \hat{\bar{D}}^{ef}_{22}\dot{\epsilon}^e_2 + \hat{\bar{D}}^{ef}_{26}\dot{\epsilon}^e_6$
$\dot{\sigma}_6 = \hat{\bar{D}}^{ef}_{61}\dot{\epsilon}^e_1 + \hat{\bar{D}}^{ef}_{62}\dot{\epsilon}^e_2 + \hat{\bar{D}}^{ef}_{66}\dot{\epsilon}^e_6$
$\hat{\bar{D}}^{ef}_{11} = \hat{D}^{ef}_{11} - \hat{D}^{ef}_{13}\hat{D}^{ef}_{31}/\hat{D}^{ef}_{33}$
$\hat{\bar{D}}^{ef}_{12} = \hat{D}^{ef}_{12} - \hat{D}^{ef}_{13}\hat{D}^{ef}_{32}/\hat{D}^{ef}_{33}$
$\hat{\bar{D}}^{ef}_{16} = \hat{D}^{ef}_{16} - \hat{D}^{ef}_{13}\hat{D}^{ef}_{36}/\hat{D}^{ef}_{33}$
$\hat{\bar{D}}^{ef}_{21} = \hat{D}^{ef}_{21} - \hat{D}^{ef}_{23}\hat{D}^{ef}_{31}/\hat{D}^{ef}_{33}$
$\hat{\bar{D}}^{ef}_{22} = \hat{D}^{ef}_{22} - \hat{D}^{ef}_{23}\hat{D}^{ef}_{32}/\hat{D}^{ef}_{33}$
$\hat{\bar{D}}^{ef}_{26} = \hat{D}^{ef}_{26} - \hat{D}^{ef}_{23}\hat{D}^{ef}_{36}/\hat{D}^{ef}_{33}$
$\hat{\bar{D}}^{ef}_{61} = \hat{D}^{ef}_{61} - \hat{D}^{ef}_{63}\hat{D}^{ef}_{31}/\hat{D}^{ef}_{33}$
$\hat{\bar{D}}^{ef}_{62} = \hat{D}^{ef}_{62} - \hat{D}^{ef}_{63}\hat{D}^{ef}_{32}/\hat{D}^{ef}_{33}$
$\hat{\bar{D}}^{ef}_{66} = \hat{D}^{ef}_{66} - \hat{D}^{ef}_{63}\hat{D}^{ef}_{36}/\hat{D}^{ef}_{33}$

Table 4.3: *Tangential stiffness.*

where

$$\hat{\mathbf{D}} = \left(\frac{\partial \Sigma}{\partial \boldsymbol{\sigma}}\right)^{-1} \mathbf{D} \tag{4.85}$$

The smeared crack multiplier, $\dot{\lambda}_f$, is obtained as in Section 4.3.8 except that $\mathbf{D}$ is replaced with $\hat{\mathbf{D}}$ in Eq. (4.64)

$$\dot{\lambda}_f = \frac{1}{\hat{A}_f}\left(\frac{\partial \Phi}{\partial \boldsymbol{\sigma}}\right)^T \hat{\mathbf{D}}\dot{\boldsymbol{\epsilon}} \tag{4.86}$$

where $\hat{A}_f$ is a positive scalar given by

$$\hat{A}_f = \left(\frac{\partial \Phi}{\partial \boldsymbol{\sigma}}\right)^T \hat{\mathbf{D}}\frac{\partial \Psi}{\partial \boldsymbol{\sigma}} + H_f \tag{4.87}$$

This gives the constitutive relation as

$$\dot{\boldsymbol{\sigma}} = \hat{\mathbf{D}}^{ef}\dot{\boldsymbol{\epsilon}} \tag{4.88}$$

where

$$\hat{\mathbf{D}}^{ef} = \hat{\mathbf{D}} - \frac{1}{\hat{A}_f}\hat{\mathbf{D}}\frac{\partial \Psi}{\partial \boldsymbol{\sigma}}\left(\frac{\partial \Phi}{\partial \boldsymbol{\sigma}}\right)^T \hat{\mathbf{D}} \tag{4.89}$$

It is assumed that the out-of-plane stress is zero, i.e. $\dot{\sigma}_3 = 0$, which means that the out-of-plane strain, $\dot{\epsilon}_3$, in Eq. (4.88) becomes equal to

$$\dot{\epsilon}_3 = \frac{\hat{D}^{ef}_{13}}{\hat{D}^{ef}_{33}}\dot{\epsilon}_1 + \frac{\hat{D}^{ef}_{23}}{\hat{D}^{ef}_{33}}\dot{\epsilon}_2 + \frac{\hat{D}^{ef}_{36}}{\hat{D}^{ef}_{33}}\dot{\epsilon}_6 \tag{4.90}$$

Insertion of Eq. (4.90) into (4.88) gives the tangential stiffness relation

$$\dot{\bar{\boldsymbol{\sigma}}} = \hat{\bar{\mathbf{D}}}^{ef} \dot{\bar{\boldsymbol{\epsilon}}} \tag{4.91}$$

where $\hat{\bar{\mathbf{D}}}^{ef}$ is the tangential stiffness matrix, cf. Table 4.3.

4.3.11 Crack Plane

It was stated above that the smeared crack strain tangential to the crack plane is assumed to be zero, i.e. $\Delta\epsilon_1'^f = 0$, cf. Eq. (4.24). This restriction gives the following relation between the smeared crack strains in the principal material directions, $\Delta\boldsymbol{\epsilon}^f$, and the smeared crack strain in the crack plane, $\Delta\boldsymbol{\epsilon}'^f$, namely

$$\left(0, \Delta\epsilon_2'^f, \Delta\epsilon_3'^f, \Delta\epsilon_6'^f\right)^T = \Delta\boldsymbol{\epsilon}'^f = \mathbf{R}^{-1}\Delta\boldsymbol{\epsilon}^f = \lambda_f \mathbf{R}^{-1}\frac{\partial\Psi}{\partial\boldsymbol{\sigma}} \tag{4.92}$$

cf. Eq. (4.25), where the incremental evolution law has been applied, i.e. Eq. (4.70). Equation (4.92) gives the restriction that during continuous fracture the crack plane shall not change its direction. However, a crack plane perpendicular to the excisting crack plane is allowed to develop. Numerical solution of Eq. (4.92) gives the transformation matrix $\mathbf{R} = \mathbf{R}_o$ which is constant during continuous fracture.

To ensure that the crack plane is fixed, Eq. (4.73) is transformed to the crack plane and reads

$$\boldsymbol{\Sigma}'\left(\boldsymbol{\sigma}, \lambda_f\right) = \boldsymbol{\sigma} - \boldsymbol{\sigma}_T + \lambda_f \mathbf{D}\mathbf{R}_o\left(\mathbf{R}_o^{-1}\frac{\partial\Psi}{\partial\boldsymbol{\sigma}}\right) = 0 \tag{4.93}$$

In Eq. (4.93) the relation $\mathbf{R}_o\mathbf{R}_o^{-1} = \mathbf{I}$ has been used. So, during successive incremental steps in the Gauss point, $\boldsymbol{\Sigma}$ in Eq. (4.75), (4.76) and (4.77) is replaced with $\boldsymbol{\Sigma}'$ and the restriction in Eq. (4.92) with $\mathbf{R} = \mathbf{R}_o$ is used throughout the iteration.

Chapter 5

Numerical calibration

5.1 Introduction

This chapter concerns the calibration of the constitutive models presented in Chapter 4. The numerical implementation of the constitutive stress-strain relations in Chapter 4 as user's material subroutine into the commercial finite element code ABAQUS/Standard, [39], is outlined in general terms in Section 5.2. The calibration of the elastic-plastic constitutive model to experimental data is described in Section 5.3. The calibration of the elastic-cohesive softening constitutive model to experimental data and its mesh restriction is described in Section 5.4, as well as the ability of the model to simulate the transition from immediate rupture to stable fracture. The mixture of the models in the same mesh model is analysed in Section 5.5.

5.2 Numerical implementation of the models

The constitutive relations defined in Sections 4.2 and 4.3 are in suitable form to be implemented into a finite element code. The commercial finite element code ABAQUS/Standard, [39], is used for this purpose. The implementation is made via the user's defined material model option possibility. The advantage of using a commercial code is that we do not have to worry about the overall solutions techniques that are otherwise required, and can concentrate on the material model. The disadvantage is that we are limited by the input and output possibilities defined in the user subroutine.

The constitutive models in ABAQUS/Standard are solved with implicit time integration, and Newton's method is used to solve the equilibrium equations, [39]. To preserve the quadratic convergence rate of Newton's method, the implementation must provide an accurate tangential stiffness matrix for use in forming the Jacobian of the non-linear equilibrium equations, [64]. The continuum stiffness matrix exhibits poor convergence properties in cases were large failure strain increments occur, [64]. If explicit time integration is used to solve the equilibrium equations it

	c [-]	$2k$ [-]	Y_1 [MPa]	Y_{45° [MPa]	Y_2 [MPa]	ν^p_{12} [-]	ν^p_{21} [-]	$\nu^p_{45^\circ}$ [-]
Newsprint	1	6	8.9	4.0	3.0	1.0	0.14	0.14
Paperboard	1	6	12	7.0	6.0	0.27	0.21	0.23

Table 5.1: *Yield parameters.*

is not necessary to use the tangential stiffness matrix since the material behavior is entirely defined in each integration point, [39].

The elastic-plastic constitutive model, [49], in Chapter 4 by Karafillis et al. [50] has been implemented via the user's defined material model option in ABAQUS/ Standard with the continuum stiffness matrix, Eq. (4.21), for use in forming the Jacobian. The solution of the non-linear equilibrium equations is in equilibrium but the convergence rate is slower than if the tangential stiffness matrix is used, [64]. The elastic-plastic constitutive model, [49], will be referred to as the Karafillis-Boyce (KB) model.

The elastic-cohesive softening constitutive model developed in Chapter 4 is implemented with the tangential stiffness matrix defined in Section 4.3.8 for use in forming the Jacobian.

For more information on how to write a user's defined material model via the defined material model option in ABAQUS/Standard, cf. ABAQUS/Standard User's Manual [39].

5.3 Calibration of the elastic-plastic model

5.3.1 Calibration of the Karafillis-Boyce yield criterion

Here the calibration procedure presented in references [49, 50] is used to calibrate the KB model in Section 4.2 to the newsprint material data in Table 5.1. In Table 5.1 c is the mixing factor and k the positive integer in the KB yield function, cf. Section 4.2.3, Y_1, Y_2 and Y_{45° are the yield stresses in the MD, CD and 45° direction, respectively, and ν^p_{12}, ν^p_{21} and $\nu^p_{45^\circ}$ are the plastic Poisson's ratios.

In Table 5.1 the c and k values are taken from reference [50] for both newsprint 45 g/m^2 and paperboard 240 g/m^2. The yield stresses and plastic Poisson's ratios for the paperboard are taken from reference [50], and for the newsprint the data are given by the uniaxial tests shown in Fig. 5.1.

In Fig. 5.1 at least four nominally equal tests are made in the MD and CD of newsprint. The transverse strains, i.e. $\epsilon_2(\sigma_1)$ and $\epsilon_1(\sigma_2)$ shown in Fig. 5.1 as the inverse $\sigma_1(\epsilon_2)$ and $\sigma_2(\epsilon_1)$, were measured in the Instron universal testing instrument (model 4502) together with Instron 2663 series non-contacting video extensometer. The plastic Poisson's ratio ν^p_{12} is defined as $\nu^p_{12} = -d\epsilon^p_2/d\epsilon^p_1$ evaluated for tensile loading in the MD, i.e. $\nu^p_{12} = -H_{y_{11}}/H_{y_{12}}$ where $\dot{\sigma}_1 = H_{y_{11}}\dot{\epsilon}^p_1$ and $\dot{\sigma}_1 = H_{y_{12}}\dot{\epsilon}^p_2$. The plastic Poisson's ratio ν^p_{21} is defined as $\nu^p_{21} = -d\epsilon^p_1/d\epsilon^p_2$ evaluated for tensile loading

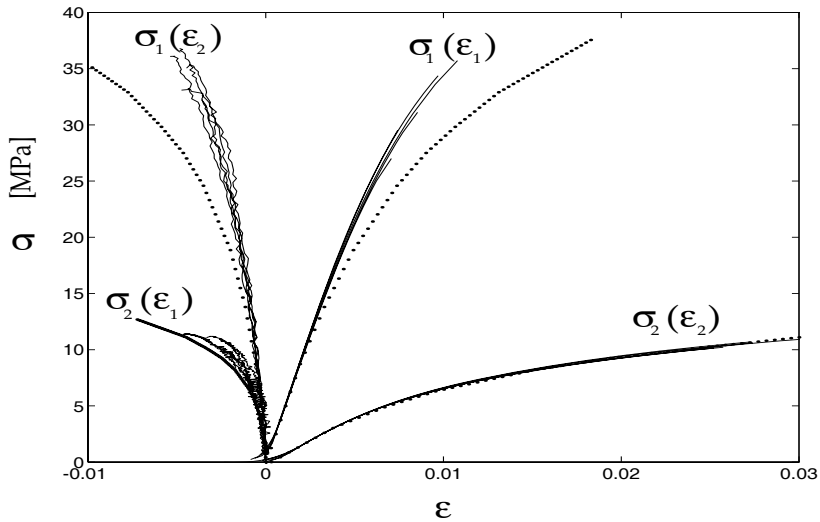

Figure 5.1: *Uniaxial stress-strain curves due to tension loading in the 1- and 2-direction. The solid curves are experimental data from newsprint 45 g/m^2 and the dotted curves are the behavior of the CD calibrated KB model.*

in the CD, i.e. $\nu_{21}^p = -H_{y22}/H_{y21}$ where $\dot{\sigma}_2 = H_{y22}\dot{\epsilon}_2^p$ and $\dot{\sigma}_2 = H_{y21}\dot{\epsilon}_1^p$. The yield stress Y_{45° and Poisson's ratio $\nu_{45^\circ}^p$ in Table 5.1 are assumed.

The newsprint data in Table 5.1 and the piece-wise linear relation between the uniaxial stress-strain curve in the MD (or the CD) from Fig. 5.1 are taken as input to a numerical procedure, cf. [49], which gives as output an anisotropic yield surface, a yield stress-plastic strain curve (cf. Eq. (4.3)) and parameter values to the mapping matrix in Eq. (4.9).

The calibrated yield surface at zero shear stress is shown in Fig. 5.2(a) and the uniaxial yield stress at different material directions is shown in Fig. 5.2(b). The black circles, ●, in Fig. 5.2 denote experimental data taken from Table 5.1.

Figure 5.3 shows two yield stress-plastic strain curves. The σ_y-ϵ_y^p curve denoted 'CD' in the figure is obtained from calibration to the measured uniaxial stress-strain curve in the CD, i.e. $\sigma_2(\epsilon_2)$ in Fig. 5.1. This calibration is referred to as the CD calibration of the KB model. The σ_y-ϵ_y^p curve denoted 'MD' in Fig. 5.3 is obtained from calibration to the measured uniaxial stress-strain curve in the MD, i.e. $\sigma_1(\epsilon_1)$ in Fig. 5.1. This calibration is referred to as the MD calibration of the KB model.

The mapping matrix in Eq. (4.9) for the MD and CD calibration of the KB

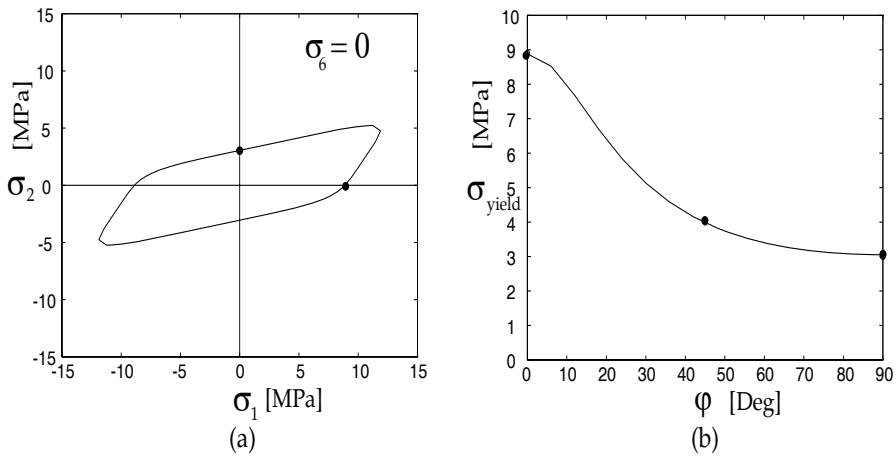

Figure 5.2: *(a) Yield surface at $\sigma_6 = 0$. (b) Yield stress-material direction curve. The circles, ●, are experimental data taken from newsprint 45 g/m^2 in Table 5.1.*

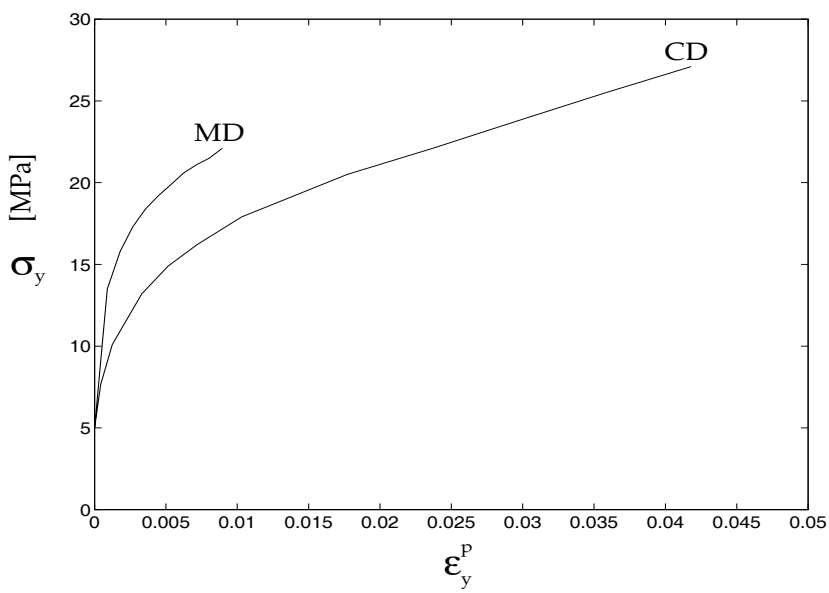

Figure 5.3: *Yield stress-plastic strain curves.*

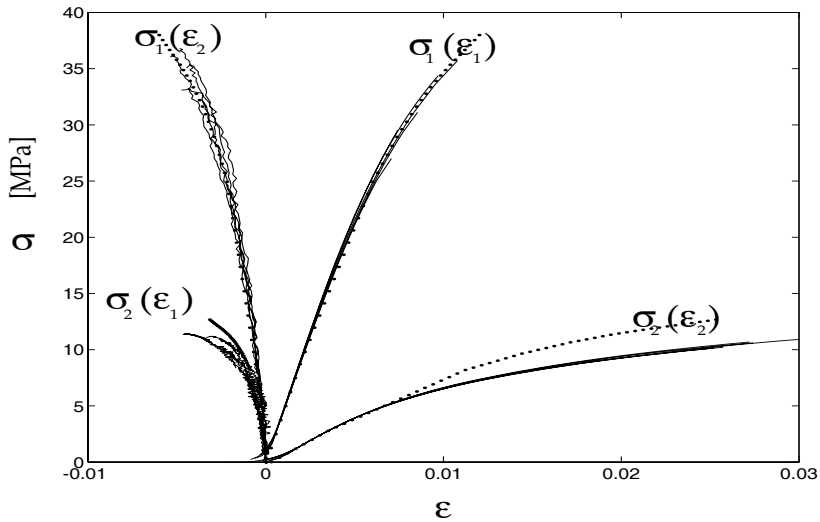

Figure 5.4: *Uniaxial stress-strain curves due to tension loading in the 1- and 2-direction. The solid curves are experimental data from newsprint 45 g/m^2 and the dotted curves are the behavior of the MD calibrated KB model.*

	Newsprint 45 g/m^2	Paperboard 240 g/m^2
E_1, MPa	4560	5420
E_2, MPa	873	1900
ν_{12}	0.31	0.38
G_6, MPa	879	1230

Table 5.2: *Elastic constants.*

model for the newsprint is given as

$$\mathcal{L} = \begin{bmatrix} 0.371 & -0.241 & 0.113 & 0 \\ -0.241 & 1.09 & -0.604 & 0 \\ 0.113 & -0.604 & 0.735 & 0 \\ 0 & 0 & 0 & 1.13 \end{bmatrix} \tag{5.1}$$

The yield parameters in Table 5.1 and one of the yield stress-plastic strain curves in Fig. 5.3 together with the mapping matrix in Eq. (5.1) give a calibrated KB model response of newsprint 45 g/m^2.

5.3.2 Comparison with experiments

The elastic stiffness parameters in Table 5.2 are the constants that determine the relations between the stresses and the elastic strains in Table 4.1 for newsprint 45 g/m^2 and paperboard 240 g/m^2, at plane stress. The experimental data in Table 5.2 for newsprint 45 g/m^2 are taken from Table 3.1 for E_1 and E_2 and the Poisson's ratio, ν_{12}, from Fig. 5.1. The shear elastic modulus for newsprint is given by the relation $G_6 = \sqrt{E_1 E_2}/(1 + \sqrt{\nu_{12}^2 E_2/E_1})/2$, cf. [7, 55]. The paperboard 240 g/m^2 experimental data in Table 5.2 are taken from reference [73].

In Fig. 5.1 the CD calibrated KB model is plotted together with experimental data from newsprint 45 g/m^2, and in Fig. 5.4 the MD calibrated KB model is plotted together with experimental data from newsprint 45 g/m^2. It is shown in Figs. 5.1 and 5.4 that the best agreement between the KB model and the experiments is in the calibration direction. It is here suggested that the KB model be calibrated to the direction that is of main interest for the analysis.

5.4 Calibration of the elastic-cohesive softening model

5.4.1 Calibration of the failure criterion

The calibration of the failure criterion in the elastic-cohesive softening (ECS) model, cf. Eq. (4.44), to material parameters measured from paper strips that suddenly rupture is here outlined.

The material parameters needed to calibrate the failure criterion for paper are given in reference [100]. The parameters are the uniaxial tensile and compression strengths in the MD and CD together with the shear and equibiaxial tensile strength and the failure Poisson's ratios, i.e. $\{T_1, T_2, C_1, C_2, T_6, P, \nu_{12}^f, \nu_{21}^f\}$, cf. Section 4.3.5 or [100].

The uniaxial tensile strengths and failure Poisson's ratios were measured in the Instron universal testing instrument (model 4502) together with Instron 2663 series non-contacting video extensometer. The compressive strengths were measured by a Lorentzen & Wettre compression tester. The equibiaxial strength, P, was obtained by enforcing the derivative of the failure criterion $\partial\Phi/\partial\sigma_1$ at $(\sigma_1, \sigma_2) = (-C_1, 0)$ to be zero. This restriction is made from observation of experimental measurements on the failure envelope for different compressive stress states for paper sheets that confirm the assumption, cf. [34, 79]. The shear strength, T_6, is obtained from fitting the failure criterion to uniaxial tensile strength values obtained from test specimens cut out at a 45 degree angle from the MD.

In Table 5.3 the parameters are given that completely describe the failure criterion for newsprint 45 g/m^2 and paperboard 240 g/m^2. The uniaxial tensile strength values T_1^o and T_2^o are taken from Table 3.1 for newsprint and from reference [73] for paperboard. The compressive strengths, C_1^o and C_2^o, for the newsprint and paper-

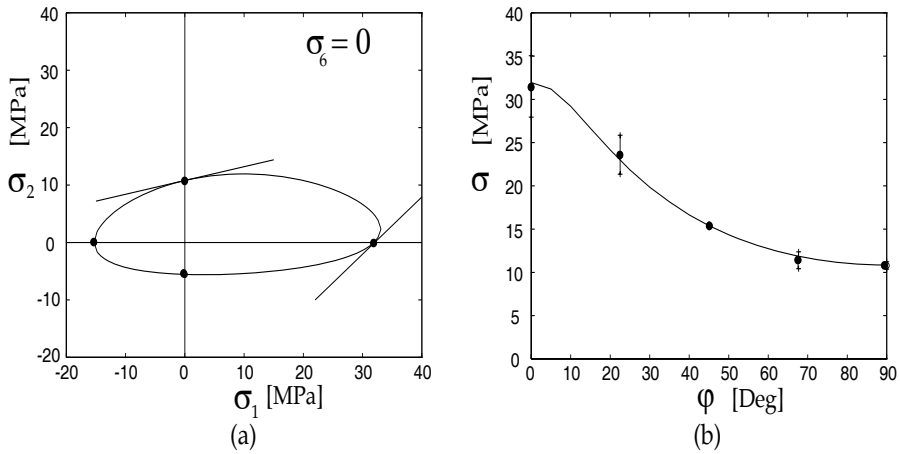

Figure 5.5: *(a) In-plane failure surface at $\sigma_6 = 0$. (b) failure stress-material direction curve. The circles, ●, are experimental data taken from newsprint 45 g/m^2.*

	T_1^o [MPa]	C_1^o [MPa]	T_2^o [MPa]	C_2^o [MPa]	T_6^o [MPa]	P^o [MPa]	ν_{12}^{fo} [-]	ν_{21}^{fo} [-]	k [-]
Newsprint	31.9	15.3	10.8	5.56	7.8	11.9	1.0	0.24	2.0
Paperboard	45.0	21.6	22.0	7.84	11.0	24.3	1.0	0.24	2.0
	γ_{11}	γ_{12}	γ_{13}	γ_{21}	γ_{22}	γ_{23}	γ_{31}	γ_{32}	γ_{33}
Newsprint	-0.273	0.135	0.864	27.8	4.40	3.58	0.668	0.444	0.01
Paperboard	-0.273	0.135	0.864	27.8	4.40	3.58	0.668	0.444	0.01

Table 5.3: *Cohesive softening parameters.*

board are obtained from measurements of five nominally equal tests made in the MD and CD. The failure Poisson's ratio in Table 5.3 is obtained from the plastic Poisson's ratios at failure in Fig. 5.4. The failure Poisson's ratio for paperboard 240 g/m^2 is assumed to be the same as for newsprint 45 g/m^2.

Figure 5.5(a) shows the failure criterion for newsprint plotted with the strength parameters in Table 5.3, at zero shear stress. In Fig. 5.5(b) the uniaxial tensile strength values are plotted as a function of the material direction. It is shown in Fig. 5.5(b) that uniaxial tensile strength values obtained from specimens cut in 22.5 and 67.5 degree angles against the MD fit the failure criterion very well. The error bars in Fig. 5.5(b) denote the standard deviation.

As was discussed in Section 4.3.5, during anisotropic softening the failure criterion must be convex throughout the softening. The anisotropic failure constants γ_{ij} where $i = 1, 2, 3$ and $j = 1, 2, 3$ given in Table 5.3 for the newsprint and paperboard fulfill this requirement. The anisotropic failure constants were obtained by trial and error with the requirement that the failure criterion must be convex throughout the anisotropic softening.

	Newsprint	k=1	k=2	k=15
φ	α	α	α	α
0°	0°	0°	0°	0°
22.5°	19° to 32°	8°	18°	22.5°
45°	30° to 42°	17°	30°	45°
67.5°	−25° to −11°	−47°	−25.5°	−22.5°
90°	0°	0°	0°	0°

Table 5.4: *The directional orientation of the damage band. The definitions of the angles α and φ are found in Fig. 4.9*

The slope of the descending stress-crack widening curve during anisotropic softening in the MD and CD is given as piece-wise linear relations in the elastic-cohesive softening model. In Fig. 5.6 thirty piece-wise linear relations are shown as solid lines between the dots. The cohesive shear modulus is obtained from the descending stress-crack widening curve in the MD and CD as $N_{66} = -\sqrt{N_{11}N_{22}}/2$, cf. Eq. (4.39), for each piece-wise linear part.

5.4.2 Calibration of the failure potential

The crack plane develops according to the evolution laws in Eq. (4.52) and the failure potential in Eq. (4.53). For calibration of the failure potential in Eq. (4.53) the uniaxial tension strengths in the MD and CD together with the shear strength for the material have to be given. It is also required that the positive integer, k, in Eq. (4.53) is given. Figure 4.8 shows the failure potential for k =1, 2 and 15.

In Table 5.3 the uniaxial tension strength in the MD and CD together with the shear strength is given for newsprint 45 g/m^2 and paperboard 240 g/m^2. The positive integer, k, in Table 5.3 is found from one element simulation with the material parameters in Table 5.3. Table 5.4 shows the simulation results for $k = 1, 2$ and 15 together with experimental data for newsprint. Here the value $k = 2$ is chosen for newsprint and paperboard, and it is seen in Table 5.4 that the simulated results of the direction of the damage band are within the experimental range of newsprint.

5.4.3 Comparison with experiments

Figure 5.7 shows some of the experimental results obtained in Chapter 3 for the newsprint from uniaxial in-plane tension of specimens 72 μm thick, 5 mm long between the grips and 15 mm wide in the MD and CD. The thickness was measured by a Lorentzen & Wettre thickness tester.

The specimen is considered in a plane stress finite element analysis. It is assumed that the localized damage is initiated by letting the element thickness in a row perpendicular against the load be 4 % less than the rest of the mesh thickness

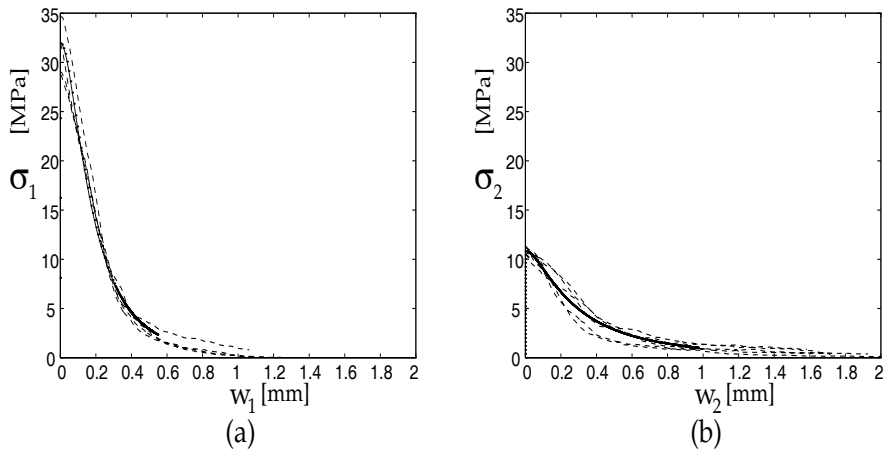

Figure 5.6: *The measured (dashed lines) and simulated (solid line) uniaxial load-crack widening curve for the short newsprint strip. (a) Loading in the MD. (b) Loading in the CD.*

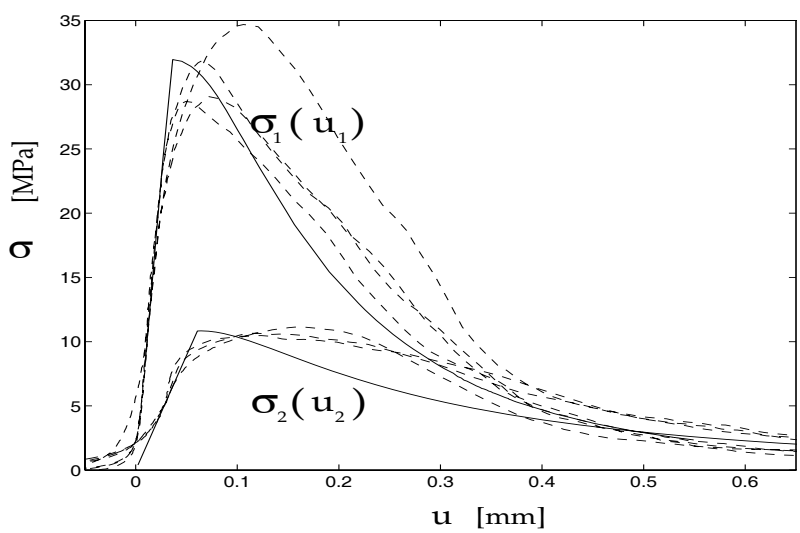

Figure 5.7: *The measured (dashed lines) and simulated (solid line) uniaxial load-elongation curve for the short newsprint strip.*

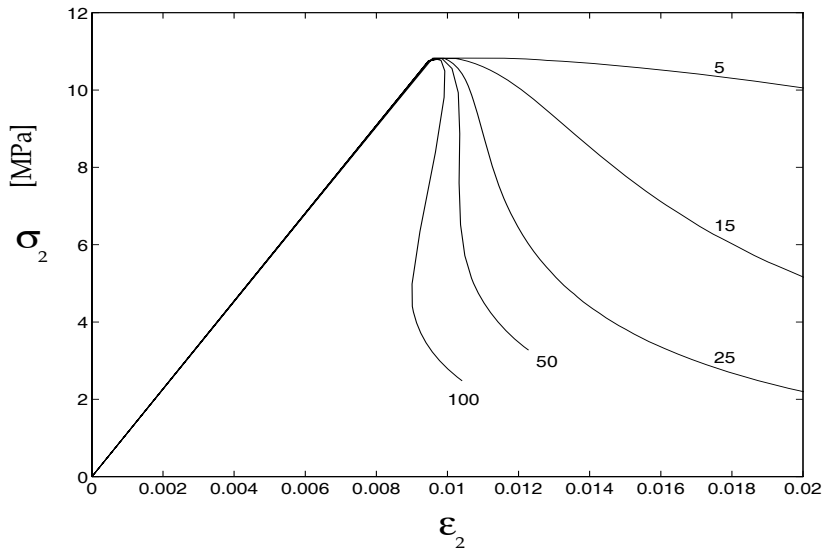

Figure 5.8: *The simulated stress-strain curve for different newsprint strip lengths, i.e.* $L = 100, 50, 25, 15$ *and* 5 *mm. The mesh consisted of 8x24 elements for the length* $L = 100, 50, 25$ *mm, 8x12 for* $L = 15$ *mm and 24x8 for* $L = 5$ *mm.*

in the specimen. The results from the simulation, with 24x8 four node elements with reduced integration, are shown in Figs. 5.6 and 5.7 together with experimental results from Chapter 3. Agreements with experiments in the MD and CD are obtained, which is no surprise since the slope from the experiment is taken as an input to the constitutive model. However, the agreement with the ascending part of the stress-elongation in the CD, Fig. 5.7, is not so good since the influence of the plastic part in the CD is not taken into consideration.

It has been reported in the literature that the tension failure mechanism in paper is related to the length of uniaxially tested paper strips, cf. [19, 21, 32, 43, 93]. Goldschmidt and Wahren [32] reported that if the paper strip is of sufficient length the paper will rupture immediately under uniaxial loading. However, if the paper strip is shortened to a critical paper strip length, the paper will exhibit a non-immediate rupture. Further shortening of the paper strip will give a stable localized damage failure, cf. Chapter 2 or [19, 21]. The elastic-cohesive softening (ECS) model developed above in Chapter 4 is able to predict the observations made in [19, 21, 32, 43, 93]. In Fig. 5.8 the simulation is made for the paper strip lengths 100, 50, 25, 15 and 5 mm, with a width of 15 mm. It is shown in Fig. 5.8 that for the paper strip length 100 mm the paper ruptures immediately, and the snap-back phenomenon is observed. Further shortening of the paper strip length will give a stable evolution of the failure zone, cf. Fig. 5.8. The strain, ϵ_2, in Fig. 5.8 is defined

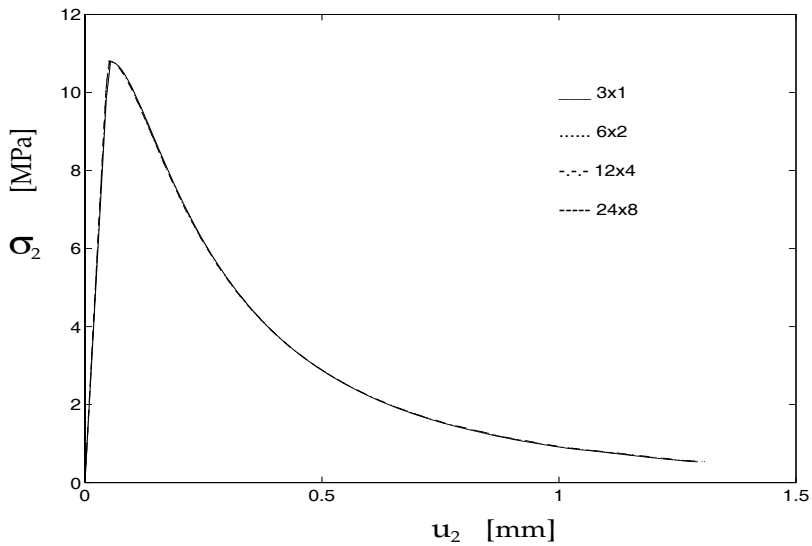

Figure 5.9: *The simulated stress-elongation curve for the specimen with different mesh refinements. The numbers of four node square elements with reduced integration used in the mesh were 3x1, 6x2, 12x4 and 24x8.*

as the total elongation, u_2, divided by the length between the grips, L, i.e. u_2/L.

5.4.4 Mesh objectivity

A specimen 15 mm wide and 5 mm long and uniaxially loaded in the CD is investigated. The simulated stress-elongation curves in Fig. 5.9 are obtained from four different mesh refinements of the specimen. The numbers of square elements used in the four meshes are 3x1, 6x2, 12x4 and 24x8. Figure 5.9 shows that the solution for the simulated specimen is independent of the mesh. Figure 5.9 illustrates the mesh objectivity for the elastic-cohesive softening model, which was one of the requirements of the model, cf. Chapter 4. Four-node elements with different Gauss point integration were used in the simulation, i.e. one Gauss point integration and 2x2 Gauss point integration rule. The simulation with the one point integration rule used the hourglass stiffness control recommended in ABAQUS/Standard [39].

5.4.5 Restrictions on the mesh

As mentioned above, the definition used of the equivalent length, L_e, (i.e. L_e is the square root of the integration point area in the element) gives the restriction on the shape and aspect ratio, i.e. the element in the model must be close to

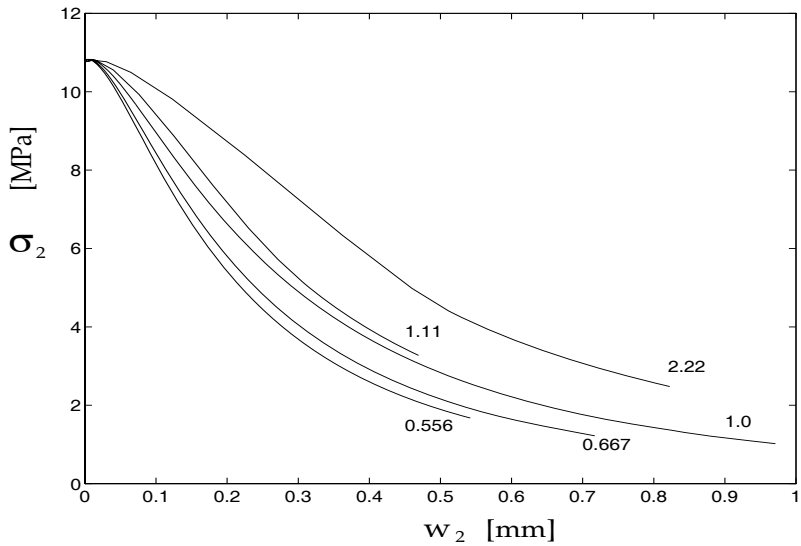

Figure 5.10: *The simulated stress-crack widening curve for the newsprint strip length from Fig 5.8 with different element aspect ratios.*

rectangular shape and have a low aspect ratio. For a ratio > 1 the length in the loading direction is greater than the length perpendicular to the loading direction. Figure 5.10 shows the importance of this rule where rectangular element shapes with different aspect ratios, namely 2.22, 1.11, 0.556, 0.667 and 1.0, are used in the simulation for different paper strip lengths, 100, 50, 25, 15 and 5 mm, respectively. The deviation from stress-crack widening curve for the element aspect ratio of 1 is large for the elements with the aspect ratio of 2.22, 0.556 and 0.667, cf. Fig. 5.10. The calibration in Fig. 5.6 is made with the element aspect ratio equal to 1.

However, other definitions of the equivalent lengths exist that are less sensitive to elements of different aspect ratios, cf. [25].

5.5 Combination of the KB and ECS models

The combination of the KB model and the ECS model in a finite element mesh is here studied under a prescribed displacement, u. The KB model is assigned to elements expected to behave elastic-plastic, and the ECS model is assigned to elements expected to behave in an elastic-softening manner.

Figure 5.11 shows the finite element model, which consists of three square four node elements of a length of 5 mm and a width of 5 mm. The elements are referred to as I, II and III. The Gauss points in the elements are denoted with 'x'.

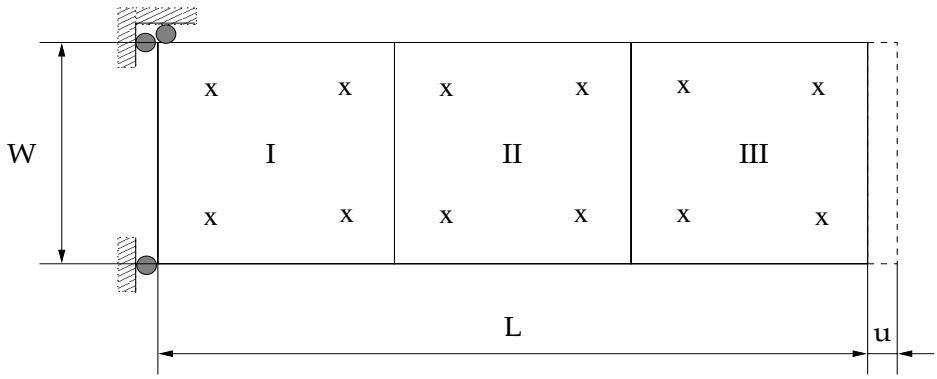

Figure 5.11: *Three element mesh of a specimen L=15 mm and W=5 mm.*

Firstly the behavior of the model is studied when the CD of the material in the elements is orientated in the loading direction, and secondly when the MD of the material in the elements is orientated in the loading direction.

5.5.1 Loading in the CD

Here the behavior of the finite element model in Fig. 5.11 is analysed under a prescribed displacement, u. The CD of the material in the elements is orientated in the loading direction. All elements in the model are given either the KB model, the ECS model or a combination of the models. In the combined model, elements I and III in Fig. 5.11 are given the KB model material property and element II is given the ECS model material property. The KB model and the ECS model are calibrated against newsprint 45 g/m^2.

In Fig. 5.12 the stress-strain curve is shown for the finite element model. The stress, Σ_2, in Fig. 5.12 is defined as the reaction load divided by the cross section area and the strain, E_2, is defined as the prescribed displacement, u, divided by the length, L. These new notations for the stress and strain for uniaxial loading are made in order to make a distinction between the stress, σ, and strain, ϵ, in the integration points of the elements. For the cases where all elements in the model are assigned to either the KB model or the ECS model, then the stress, Σ_2, and the strain, E_2, are equal to the stress, σ_2, and the strain, ϵ_2, in the integration points, i.e. $\Sigma_2 = \sigma_2$ and $E_2 = \epsilon_2$, due to homogenous loading, cf. Fig. 5.14(a)-(d). This is not the case for the combined model where the stress, Σ_2, and strain, E_2, differ from the stress, σ_2, and strain, ϵ_2, in the integration points of the finite element model, cf. Fig. 5.14(e)-(f).

In Fig. 5.12 'x' denotes the prescribed displacement at different displacement increments. The increase in the displacement is given a number ranging from 1 to 8. The displacement increments are connected in the figure with lines in order to make the figure easier to read. The stress, Σ_2, due to the prescribed strain, E_2, is shown

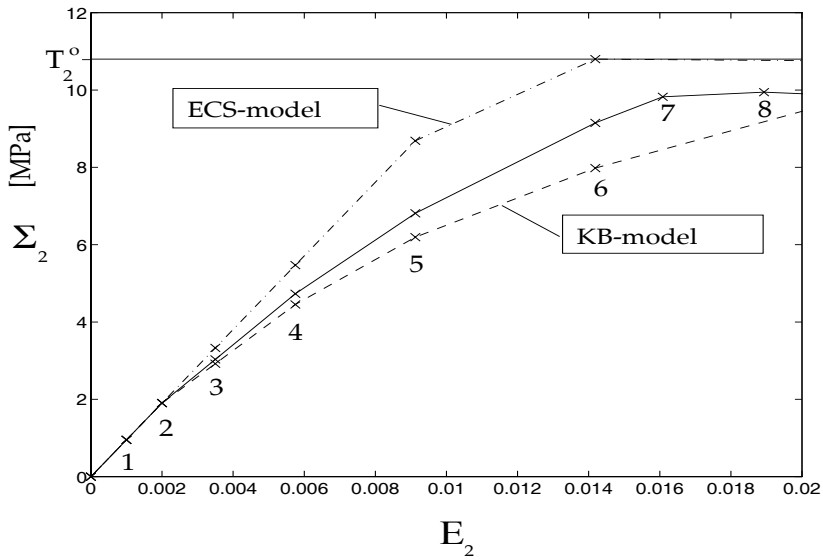

Figure 5.12: *Stress-strain curves.*

in Fig. 5.12 for all elements given the KB material properties (dashed line) and all elements given the ECS material properties (dashed-dotted line) together with the combined model (solid line). The figure shows that the specimen for the case where all elements are given the KB material properties yields at the displacement increment number 3. The specimen for the case where all elements are given the ECS material properties is linear up to the failure stress, and failure occurs at increment number 6. The combined model is shown to yield at increment number 3 and soften at number 8. It is further seen that element II with the ECS material model in the combined model makes the stress-strain behavior stiffer than the case where all elements are given the KB material properties. It is also noted that the combined model softens at 8 % lower failure stress than is the case where all elements are given the ECS material properties.

In Fig. 5.13 the deformed shape of the combined model is shown for increment number 6, and it is clearly seen that the contraction of the elements in the transverse direction is heterogeneous. In Fig. 5.14(e)-(f) it is seen that for increment number 5 the stresses in the elements begin to differ as compared to each other, i.e. heterogeneous deformations arise, and for increments thereafter this effect is amplified. This is due to different contraction in the transverse direction for elements I and III as compared to element II. For the combined model Fig. 5.14(e)-(f) shows that in elements I and III positive and negative stresses arise in the transverse direction whereas in element II negative stresses arise. However, summation of the transverse stresses, σ_1, in the integration points gives zero transverse stress, Σ_1, for the finite

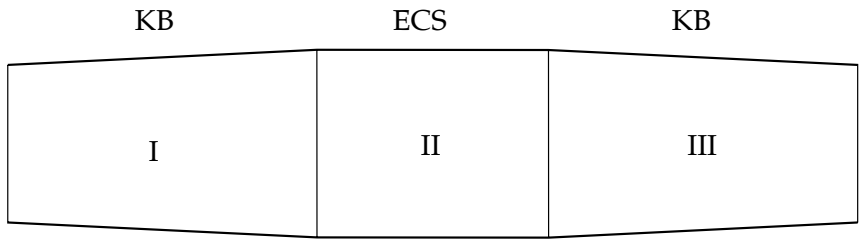

Figure 5.13: *Enlarged displacement at increment number 6 of the combined model.*

element model, i.e. $\Sigma_1 = 0$. The shear stress is equal to zero during the prescribed deformation.

The lower failure stress for the combined model shown in Fig. 5.12 is due to the reason that stresses in the loading and transverse direction enter into the failure criterion. In Fig. 5.5 it is seen that the combinations of $\sigma_1/T_1^o < 0$ and $\sigma_2/T_2^o > 0$ in Fig. 5.12 give a lower failure stress than if $\sigma_1/T_1^o = 0$, which is the case during homogenous deformation.

To conclude, it has been found that the combined model will predict a lower failure stress due to the heterogeneous deformation occurring in the element when different elements in the model are assigned to either the KB model or the ECS model.

5.5.2 Loading in the MD

Here the MD of the material is orientated in loading direction. This will also give different contraction in the transverse direction and stresses in the transverse direction arise, cf. Fig. 5.15. For the combined model Fig. 5.15 shows that in elements I and III positive stresses arise in the transverse direction whereas in element II negative stresses arise. So, even if the material direction is changed the combined model will predict a lower failure stress due to the heterogeneous deformation occurring when different elements in the model are assigned to either the KB model or the ECS model.

5.6 Comments

This chapter has shown that the ascending load-elongation behavior of paper is well described by an elastic-plastic constitutive relation, [49], cf. Fig. 5.4. The descending part of the load-elongation of paper is well described by the cohesive softening model developed in Sections 4.3.4 and 4.3.5, cf. Fig 5.6. A model that combines the KB model and the ECS model into an elastic-plastic-cohesive softening

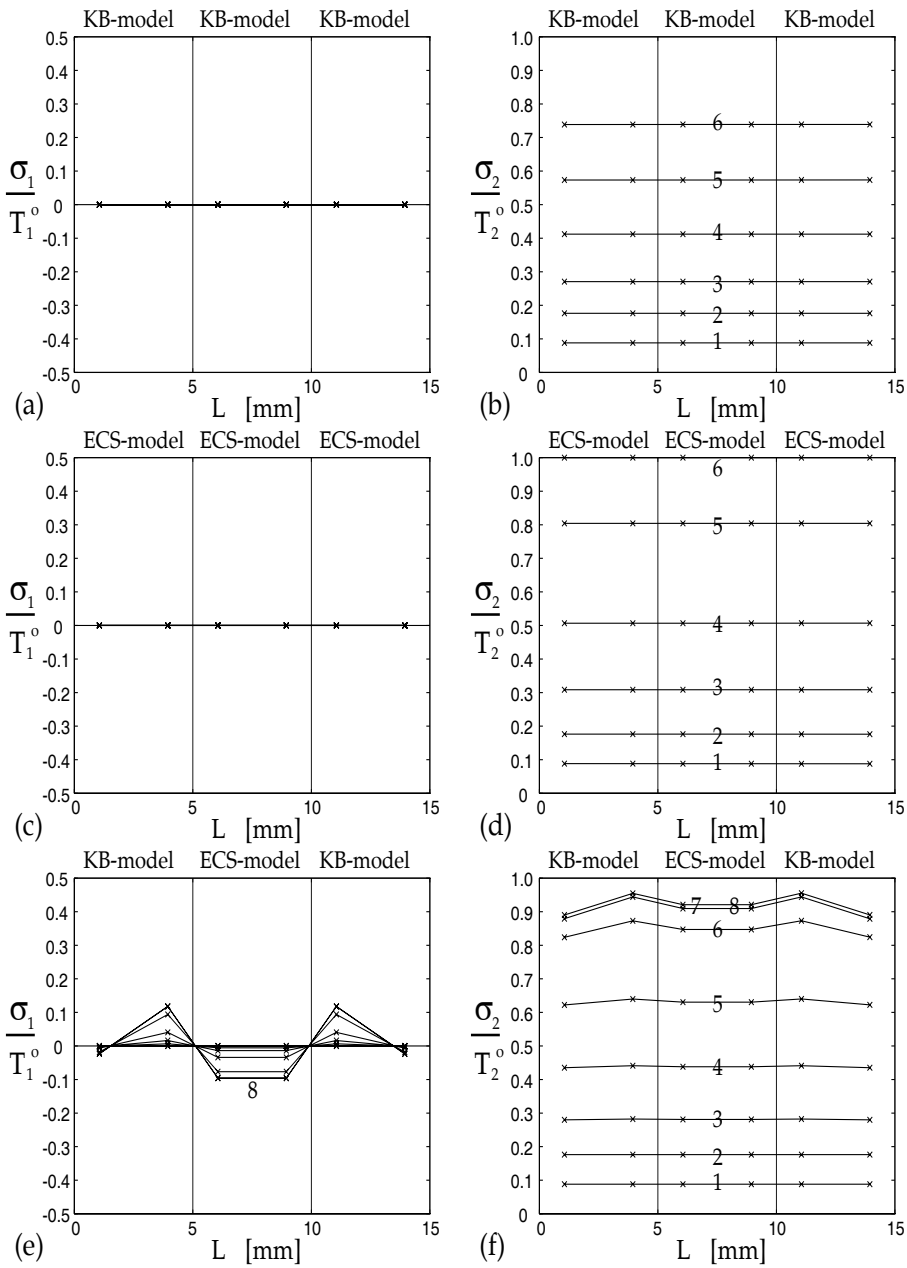

Figure 5.14: *The stresses, σ_1/T_1^o and σ_2/T_2^o, versus the Gauss point positions in the finite element mesh. (a)-(b) KB model, (c)-(d) ECS model and (e)-(f) combined model.*

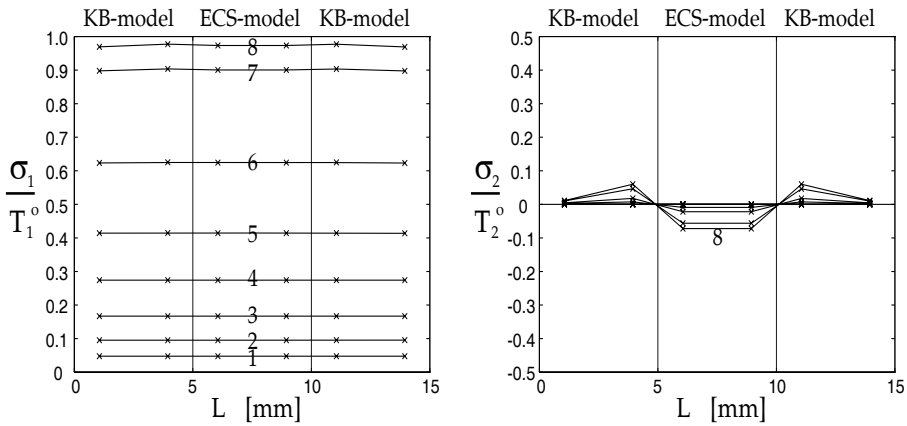

Figure 5.15: *The stresses, σ_1/T_1^o and σ_2/T_2^o, versus the Gauss point positions in the finite element mesh.*

model would presumably very well describe the entire load-elongation behavior. The limitation of this work is to study the descending part of the load-elongation relation for paper and to review the ascending load-elongation behavior of paper. An elastic-plastic-cohesive softening model is therefore left open for further studies and analysis.

A finite element model with the KB model or the ECS model applied in adjacent elements is found to predict a lower failure stress due to the heterogeneous deformation. So, it is recommended that finite element analysis where the KB model and the ECS model are used in adjacent elements should in general be avoided since more or less incorrect results may occur.

Chapter 6

Analysis of notch specimen

6.1 Introduction

This chapter concerns the analysis of a rectangular sheet $2W$ wide and $2H$ high containing a central crack $2a$ long where the ends of the sheet are subjected to uniform displacement perpendicular to the crack line and zero displacement parallel to the crack line, cf. Fig. 6.1. Experimental observations of the central cracked rectangular sheet (CCS) are discussed in Section 6.3. Experiments and simulations of the CCS are compared in Section 6.4, when the MD is perpendicular to the crack line as well as when the CD is perpendicular to the crack line. Newsprint 45 g/m^2 is used in the experiments and the ECS model calibrated to the newsprint is used in the simulations. The process region just ahead of the crack tip and its influence on the overall load-deformation relation are analysed in Sections 6.5 and 6.6.

In the literature a considerable amount of work is presented on experiments, theories and analysis of notched paper specimen, see for example [2, 20, 28, 30, 37, 86, 87, 90, 92, 96]. Analysis of notched paper specimens by any cohesive crack model such as the model presented in Chapter 4 has, however, not been found. Several experimentally observed stable load-displacement performances of notched paper specimens have however been reported, cf. [85, 86, 87, 88, 92].

6.2 Central cracked sheet in mode I

Two heights of the central cracked rectangular sheet (CCS) are chosen in this investigation, one of a height shorter than the stable paper strip length, i.e. $2H = 10$ mm, and one of a height greater than the critical length, i.e. $2H = 100$ mm. The width is equal to $2W = 50$ mm and the crack length $2a = 20$ mm.

Both experiments and simulations are used in this investigation. The experimental setup, humidity and temperature are the same as reported in Chapter 3. The crack in the CCS was obtained by a scalpel. The material used in the experiments is newsprint 45 g/m^2. At least six nominally equal tests were made in each direction and for each height.

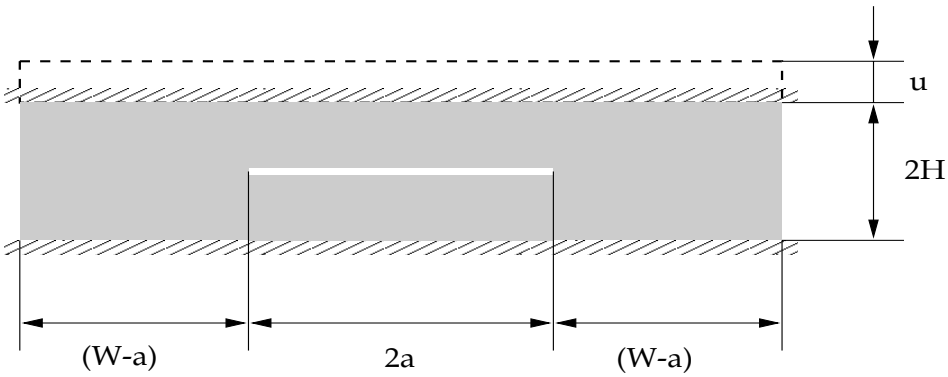

Figure 6.1: *The CCS geometry.*

6.3 Experimental observations

The experimentally obtained load-deformation curves for the CCS specimens of heights 100 mm and 10 mm loaded in the MD are shown in Figs. 6.2 and 6.3, respectively. Figure 6.4 shows the CCS specimens of heights 100 mm and 10 mm loaded in the CD. In Figs. 6.2, 6.3 and 6.4 the compliance of the loadcell has been subtracted from the recorded elongations. It is seen from comparison of Figs. 6.2 and 6.3 that the shorter CCS specimen ($2H = 10$ mm) exhibits a stable descending load-displacement curve, which is a measure of a stable process region (localized damage) growth throughout the ligament length. The long CCS specimen ($2H = 10$ mm) exhibits immediate rupture, i.e. unstable process region growth.

Different limit loads (maximum load) are observed for the long and short CCS specimens, cf. Figs. 6.2 - 6.4. For the long CCS in Fig. 6.2 the limit load ranges from 43 N to 47 N, and for the short CCS in Fig. 6.3 the limit load ranges from 54 N to 64 N (if the lowest curve is excluded in Fig. 6.3), i.e. the limit load for the short CCS is larger than for the long CCS. Comparison between Figs. 6.2 and 6.3 shows that the initial stiffness for the long CCS is less than for the short CCS. However, if the initial stiffness is divided by the cross section area, $A = (2W - 2a)t$, and multiplied by the length of the specimen, $2H$, i.e. $(F/A)/(u/2H)$, then it is found that $(F/A)/(u/2H)$ for the long CCS ($\sim$ 6.3 GPa) is greater than for the short CCS ($\sim$ 4.8 GPa). It is also seen in Fig. 6.4 that for the CD loaded CCS specimens the initial stiffness for the long CCS is less than for the short CCS, and the limit load for the long CCS is less than for the short CCS. Also for the CD loaded CCS specimens it is found that $(F/A)/(u/2H)$ for the long CCS ($\sim$ 1.35 GPa) is greater than for the short CCS ($\sim$ 0.95 GPa). The limit load for the long CCS ranges from 13.9 N to 15.5 N, and for the short CCS the limit load ranges from 19.6 N to 24 N. So, the limit load decreases and the initial stiffness defined as $(F/A)/(u/2H)$ increases with increasing height for loading in both the MD and the CD.

In Figs. 6.5 and 6.6 the crack path direction is shown for the long and short CCS

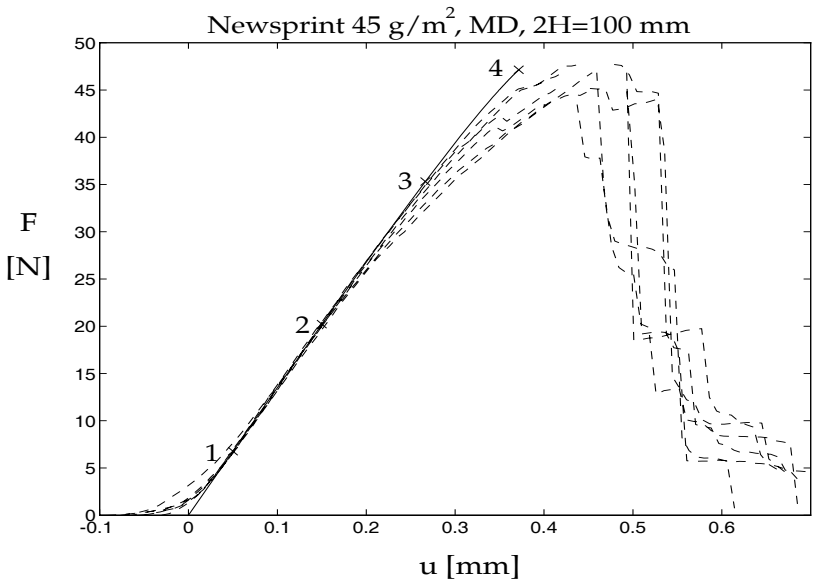

Figure 6.2: *The load-elongation curves from experiments (dashed lines) and simulation with the ECS model (solid line) for the long CCS loaded in the MD.*

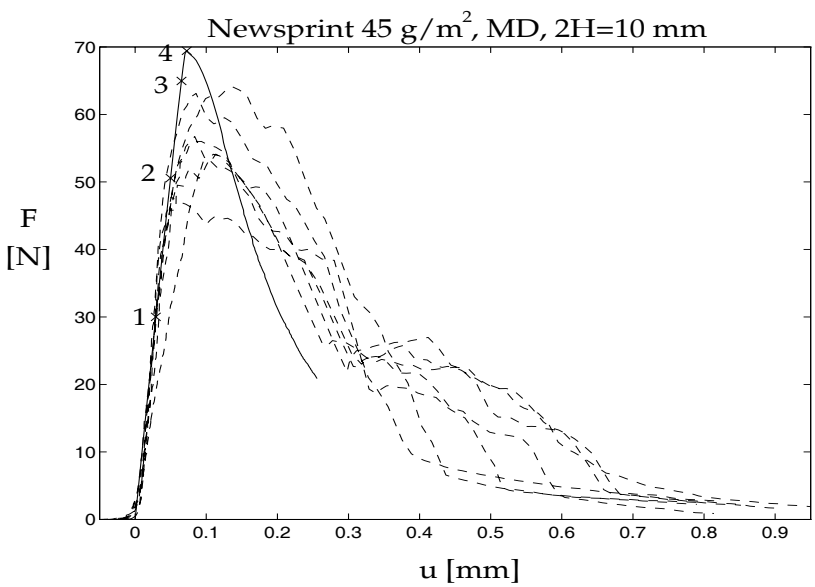

Figure 6.3: *The load-elongation curves from experiments (dashed lines) and simulation with the ECS model (solid line) for the short CCS loaded in the MD.*

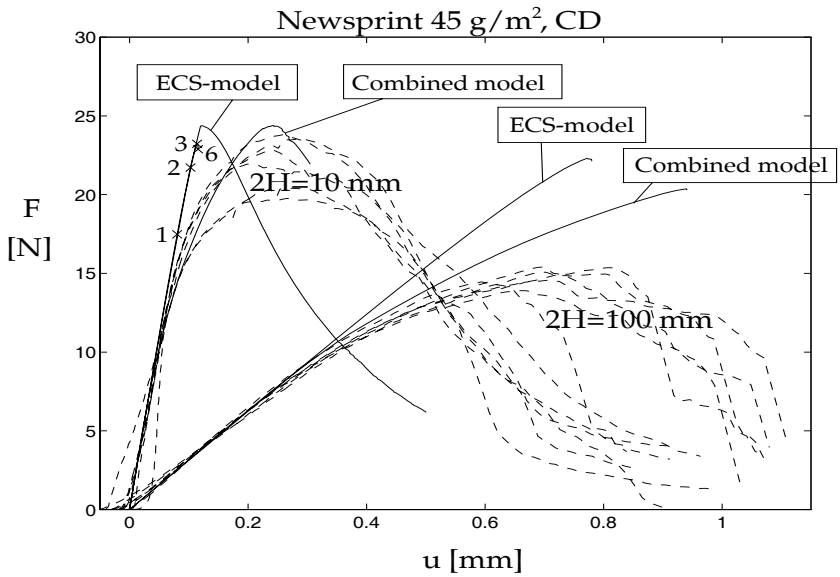

Figure 6.4: *The load-elongation curves from experiments (dashed lines) and simulation (solid line) for the long and short CCS loaded in the CD.*

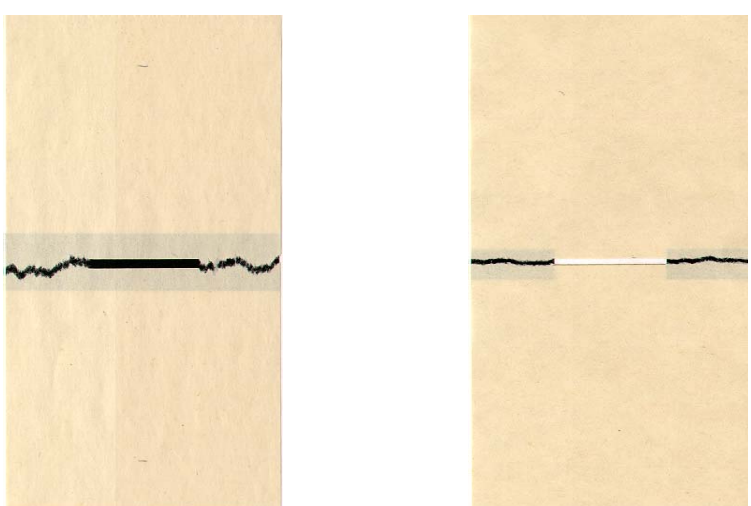

Figure 6.5: *Typical long CCS specimens loaded in the MD (left figure) and in the CD (right figure).*

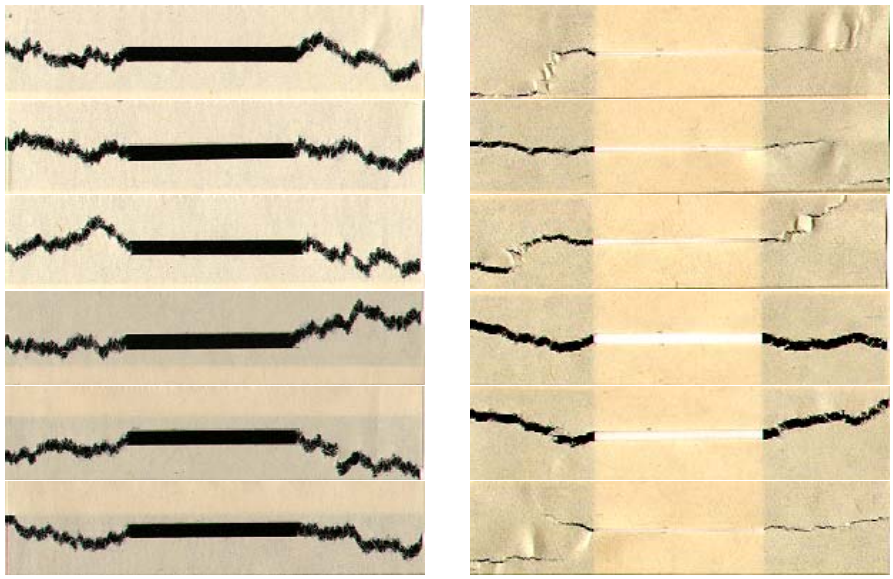

Figure 6.6: *The short CCS specimens loaded in the MD (left figure) and in the CD (right figure).*

loaded in the MD and CD. It is seen in Fig. 6.5 that the crack paths for a typical long CCS are approximately parallel with the pre-existing crack. For the short CCS loaded in the CD the crack paths ahead of the crack for the tested specimen are shown in Fig. 6.6 (right figure). It is seen in the right figure that the crack paths ahead of the crack edge are initially parallel to the pre-existing crack and thereafter they either continue to be parallel to the pre-existing crack or divert at an angle against the crack plane. The left figure in Fig. 6.6 shows the crack paths for the short CCS loaded in the MD. It is seen that some crack paths are parallel to the pre-existing crack, whereas some divert considerably from a plane parallel to the pre-existing crack.

The scatter in the limit load for the short CCS as compared to the long CCS for loading in the MD and the CD, cf. Figs. 6.2 - 6.4, is assumed to depend on the scatter in the crack path observed in Fig. 6.6 for the short CCS.

6.4 Comparison with finite element simulations

6.4.1 Comparison with simulations in the MD

The finite element mesh used in the simulations of the CCS specimens is shown in Fig. 6.7 ($2H = 100$ mm) and Fig. 6.8 ($2H = 10$ mm). In the simulations half of the geometry is used, due to symmetry reasons, for both the long and short CCS.

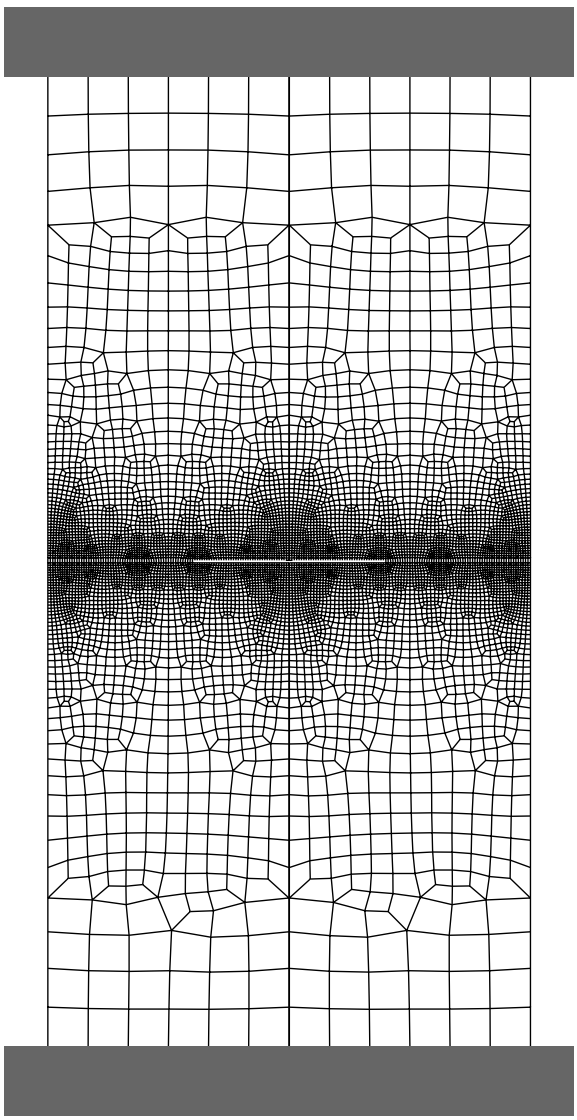

Figure 6.7: *The numbers of elements and nodes in half of the mesh are 4195 and 4341, respectively. The elements ahead of the crack edge are quadratic with a side length of 0.25 mm.*

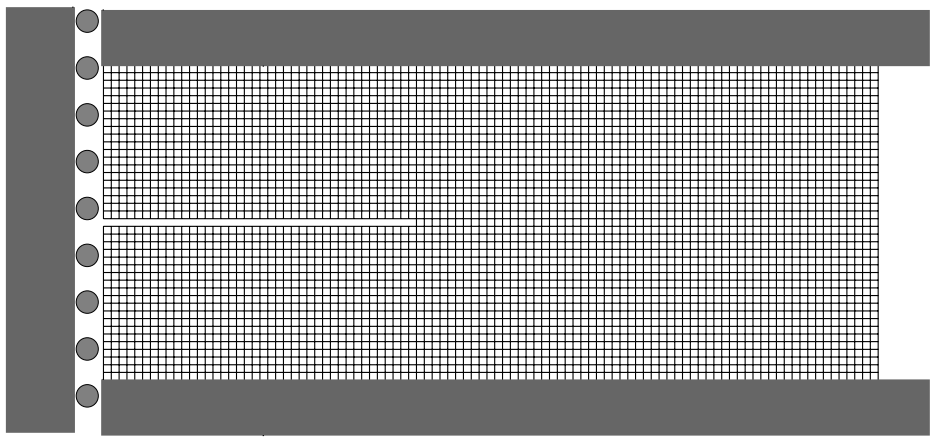

Figure 6.8: *The numbers of elements and nodes in the mesh are 4019 and 4200, respectively. The elements ahead of the crack edge are quadratic with a side length of 0.2439 mm.*

The boundary conditions on the geometries are the ones shown in Figs. 6.7 and 6.8. The mesh in Figs. 6.7 and 6.8 consists of four node plane stress elements. It is assumed in the simulations that the process region ahead of the crack tip grows in the direction of the pre-existing crack. The elements in the ligament length (the distance from the crack tip to the outer boundary in the crack growth direction) are given the ECS model material property, and all other elements in the mesh are given orthotropic elastic material properties. The material models are calibrated to newsprint 45 g/m^2, cf. Chapter 5. Reduced integration is used for the four node element row straight ahead of the pre-existing crack.

Simulations of the CCS specimens loaded in the MD are shown in Figs. 6.2 and 6.3, where the simulation of the CCS specimen is plotted together with the experiments. It is seen that good agreement is obtained between the simulations and experiments. From this it can be assumed that the plastic effects in MD are small in comparison with the elastic and cohesive softening effects, which justifies the choice of the ECS model in the simulations. The prediction of the limit load for the long CCS specimen is in good agreement with the measured results, whereas the short CCS specimen over-predicts the limit load in the range of 9% - 22%, cf. Figs. 6.2 and 6.3.

Figures 6.9 and 6.11 show the stress in the loading direction (MD) normalized with the failure stress in the MD, σ_1/T_1^o, ahead of the crack tips for the long and short CCS specimens, respectively, plotted against the width, $2W$, of the CCS geometry. Figures 6.10 and 6.12 show the stress in the transverse loading direction normalized with the failure stress in the CD, σ_2/T_2^o, ahead of the crack tips for the long and short CCS specimens, respectively, plotted against the width, $2W$, of the CCS geometry. The stress curves in Figs. 6.9 - 6.12 are obtained from the loads referred to as 1, 2,

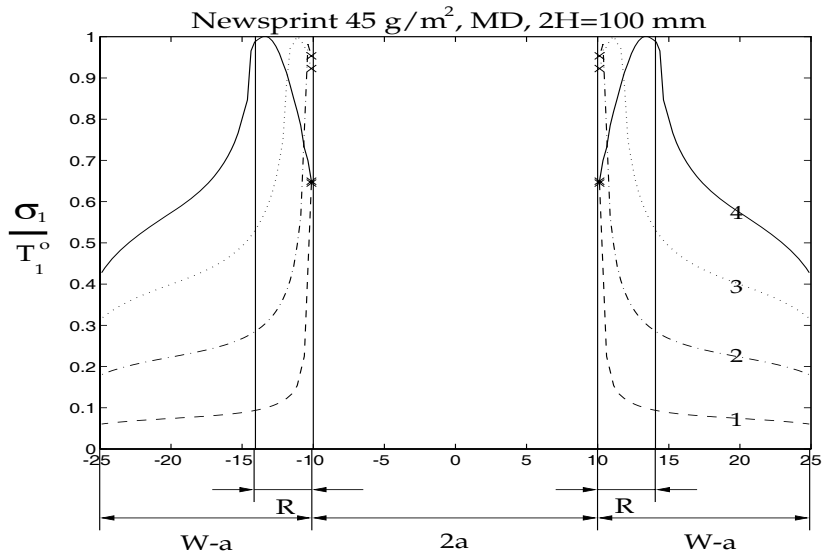

Figure 6.9: *The normalized stress, σ_1/T_1^o, versus the width, $2W$, of the CCS geometry.*

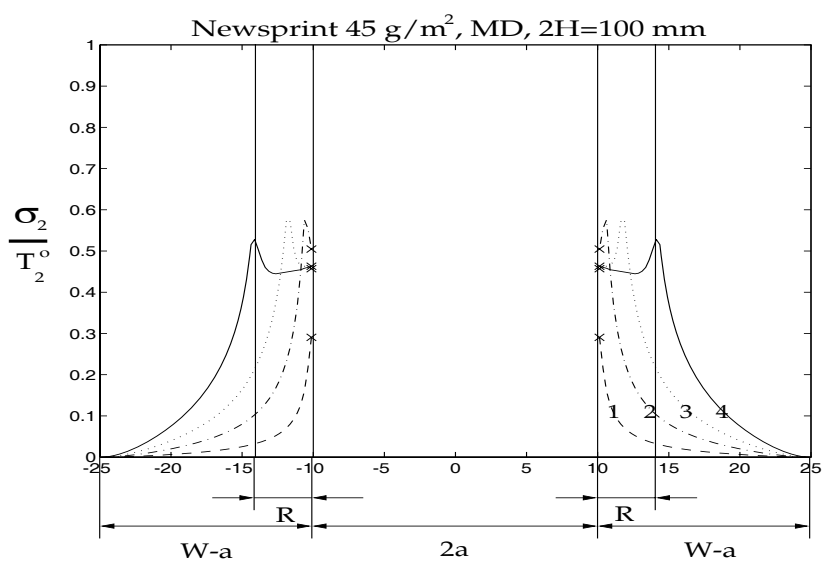

Figure 6.10: *The normalized stress, σ_2/T_2^o, versus the width, $2W$, of the CCS geometry.*

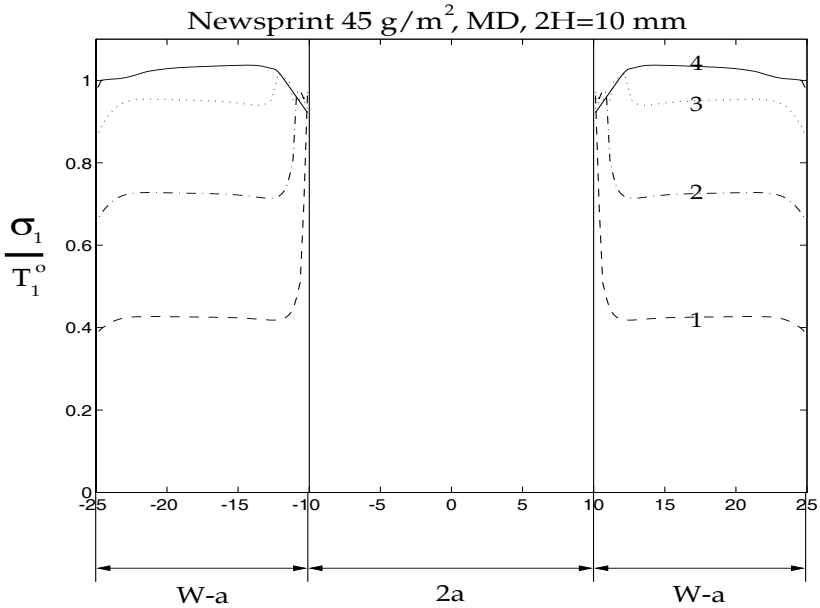

Figure 6.11: *The normalized stress, σ_1/T_1^o, versus the width, $2W$, of the CCS geometry.*

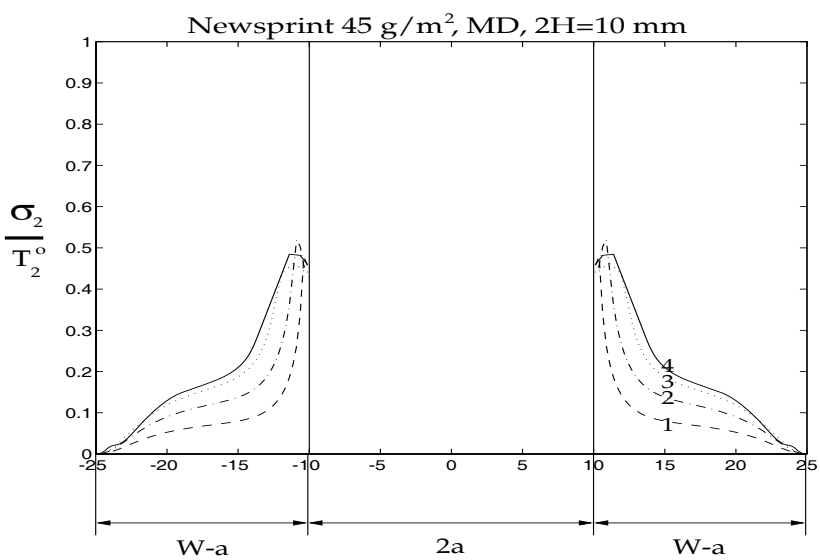

Figure 6.12: *The normalized stress, σ_2/T_2^o, versus the width, $2W$, of the CCS geometry.*

3 and 4 in Figs. 6.2 and 6.3. The 'x' in Figs. 6.9 and 6.10 denotes the stresses at the Gauss point in the element at the crack tip for the stress curves referred to as 1, 2, 3 and 4. The shear stress is equal to zero in the ligament length ahead of the crack tip, so the stresses, σ_1 and σ_2, are equal to the principal stresses.

For the long CCS specimen the extent of the process region ahead of the crack tip is given at the maximum normalized stress, σ_2/T_2^o in Fig. 6.10, for the loads referred to numbers 1 to 4 in Fig. 6.2. This is illustrated by R in Figs. 6.9 and 6.10 for the stresses referred to number 4.

The numbered loads are denoted as F_i, where i is equal to numbers 1, 2, 3 and 4 in Fig. 6.2. It is seen from Fig. 6.10 that the growth of the process region from the load, $F = 0$ to $F_3 \approx 0.73F_{limit}$, where $F_{limit} = 47.1$ N is limit load, is approximately the same as the growth of the process region from $F_3 \approx 0.73F_{limit}$ to $F_4 = F_{limit}$. The normalized stress, σ_1/T_1^o, at the crack tip is non-zero during the ascending part of the load-elongation curve, cf. Figs. 6.2 and 6.9. This implies that the process region grows during the ascending part, i.e. no crack growth occurs during the ascending part. After the limit load is reached the process region grows unstable until the end of the ligament is reached, i.e. $R = (W - a) = 15$ mm.

For the short CCS specimen the process region is $R \approx 2.1$ mm at the load, $F_3 \approx 0.94F_{limit}$, where $F_{limit} = 69.5$ N, and at the limit load $F_4 = F_{limit}$ the process region is $R \lessapprox 15$ mm, i.e. the process region near the limit load grows stable from a process region of $R \approx 2.1$ mm to $R \lessapprox 15$ mm.

The simulations in Figs. 6.9 - 6.12 reveal that, at the same reaction force, the extent of the process region ahead of the crack tip, R, for the long CCS has extended much more into the ligament length as compared to the short CCS specimen. This observation reveals the fact that the concentration of the stresses at the crack tip, at the same remote loading, is more pronounced for the long CCS than for the short CCS. From comparison at loads near the limit load in Figs. 6.9 and 6.11 it is seen that the stress curve in the loading direction for the long CCS is more concentrated to the process region, whereas for the short CCS the stress curve is more or less the same over the ligament length, $(W - a)$. It should further be noted that in the end of the process region the stresses in the loading direction and the stresses in the transverse loading direction have the following relation $\sigma_2/T_2^o \approx 0.5\sigma_1/T_1^o$; this can also be seen from the failure surface at zero shear stress, cf. Fig. 5.5.

In Fig. 6.13 are shown the principal stresses close to the limit load for the long CCS specimen. It is seen in the lower figure that the principal compressive stresses arise at the boundary of the pre-existing crack and that the principal compressive stresses surround the ligament length. The principal compression stresses may give out-of-plane movements; this implies that anti-buckling guides should be used in the experiments to get a better agreement between the experiments and the simulations. It is further seen in Fig. 6.13 (upper figure) that the stresses are concentrated around the process region tip and the stresses decrease in the process region, see also Figs. 6.9 - 6.12.

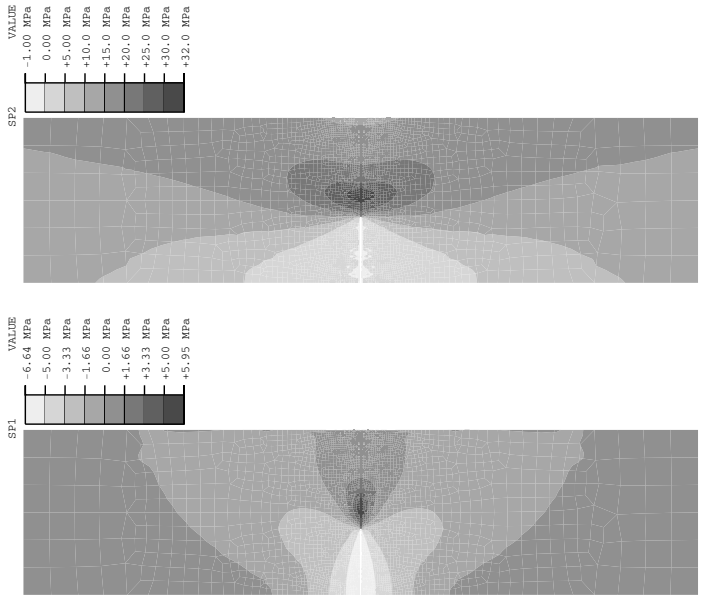

Figure 6.13: *The principal stresses for the long CCS loaded in the MD.*

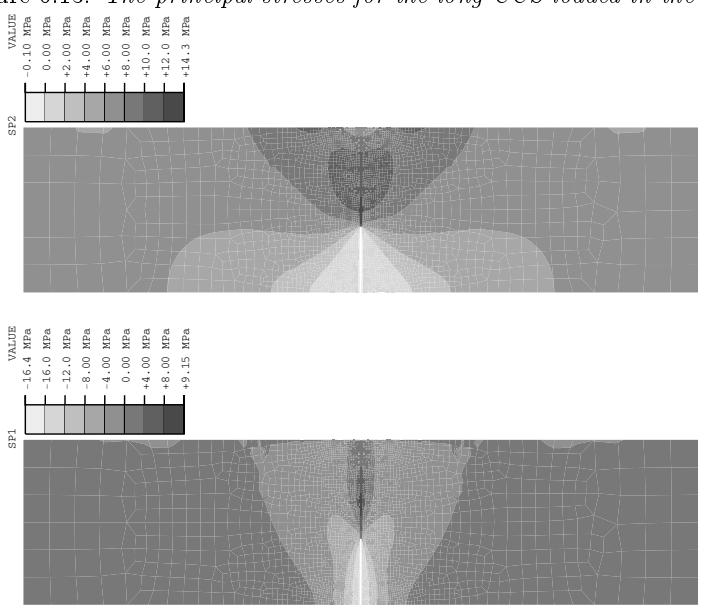

Figure 6.14: *The principal stresses for the long CCS loaded in the CD.*

6.4.2 Comparison with simulations in the CD

Simulations of the CCS specimens loaded in the CD are shown in Fig. 6.4, where the simulation of the CCS specimen is plotted together with the experiments. It is seen that poor agreement is obtained between the experiments and simulations with the ECS model, whereas agreement is obtained between the experiments and simulations with a combination of the KB model and the ECS model. In the combined model used here the element row ahead of the crack tip in Figs. 6.7 and 6.8 was given the ECS model material property, and the rest of the elements in the CCS specimens were given the KB model material property. The combined model should be used with care, as concluded in Chapter 5. The reason for using it here is to show that the plastic part in general must be taken into consideration if agreement is to be obtained between the simulations and the experiments with respect to the shape of the ascending part of the load-elongation curve. So, for the loading in the CD the plastic effects are large in comparison with the elastic and cohesive softening effects, and use of a model which includes all effects is vital.

The prediction with the ECS model of the limit load for the short CCS specimen is in agreement with the measured results, whereas the long CCS specimen over-predicts the limit load by approximately 35 %, cf. Fig. 6.3. The simulation with the ECS model of the long CCS gave the limit load $F_{limit} = 22.3$ N and the experiments gave the limit load $F_{limit} \approx 14.5$ N. In Fig. 6.14 (lower figure) it is seen that the maximum principal compressive stresses are approximately a factor of 3 larger than for the maximum principal compressive stress in Fig. 6.13 (lower figure). So the compression stresses in Fig. 6.14 (lower figure) may give out-of-plane movements; this implies that anti-buckling guides should be used in the experiments. The long CCS specimens have been measured with and without anti-buckling guides in the Lorentzen & Wettre fracture toughness tester at STFI by C. Fellers, at the request of the author. It was found that the limit load with anti-buckling guides gave $F_{limit} \approx 22.7$ N and without $F_{limit} \approx 15.7$ N. So, if anti-buckling guides are used, the prediction of the limit load for the long CCS specimen is in agreement with experimental results.

As was seen in Fig. 6.6, for the short CCS the observed crack path is scattered. To simulate this scatter in the crack paths, the equibiaxial failure stress, σ_f, in the different finite elements was assigned random values in the interval of $\pm 1\%$ from the average value of the equibiaxial failure stress. The mesh in Fig. 6.8 was given four node plane stress elements with reduced integration together with the ECS model in all elements. In Fig. 6.4 the simulated load-elongation curve is shown together with 'x' marks referring to loads, numbered from 1 to 6, at which the crack paths are shown in Fig. 6.15. Note that at number 3 the limit load is reached, and thereafter the load decreases down to number 6, where the simulations were terminated. The loads referring to numbers 4 and 5 are not marked in Fig. 6.4 since they are very close to the limit load at number 3. The relative displacement between load numbers 3 to 5 is 0.6μm. The simulated crack path at loads number 1 and 2 in Fig. 6.15 shows that the crack path begins to localize straight ahead of the crack tip. Between

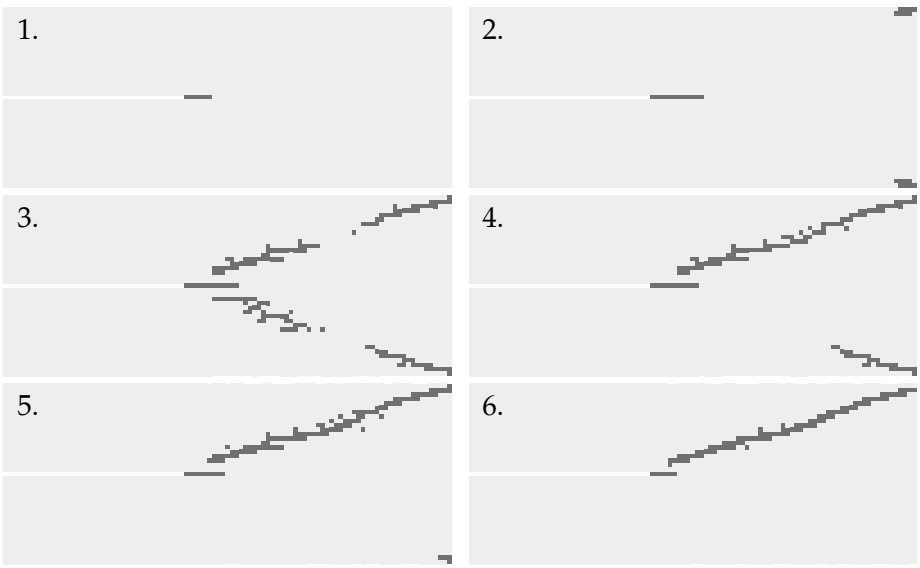

Figure 6.15: *Simulation of the crack path for the right half of the short CCS at loads given at numbers 1 to 6 in Fig. 6.4.*

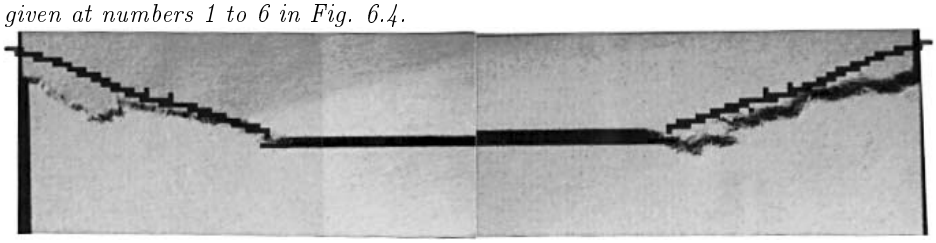

Figure 6.16: *Photo of the crack path for the short CCS specimen together with the simulated crack path in Fig. 6.15 at stage 6.*

the loads numbered 2 and 3, i.e. before the limit load is reached, the crack path begins to localize at approximately ±20 degree angle against the crack plane, cf. Fig. 6.15. After the limit load is reached, one of the crack paths is chosen more or less directly, and consequently the concurrent crack path unloads, cf. stages 3 to 5 in Fig. 6.15. The crack path is chosen from the decrease in the loads from number 5 to number 6, cf. Fig. 6.15.

Experiments on the short CCS specimens reveal, see Section 6.3, that the crack path for some of the tested CCS initially grows directly ahead of the crack tip, and thereafter it begins to be localized at an angle against the initial crack plane, cf. Fig. 6.6. In Fig. 6.16 the simulated results of the crack path are also shown together with one of the experimentally obtained crack paths. It is observed in Fig. 6.16 that the agreement between the simulated and experimental crack paths is satisfactory.

It should be noted that the simulated limit load in Fig. 6.4 for the assumption of a crack path ahead of crack tip is 4.7 % higher than the simulated limit load for the case when all elements were allowed to fail. The reason for this diversity might be that constraints on a crack path generally result in higher load capacity. However, it may also be assumed that the diversity is due to the different crack path observed in the simulations, or that the defined equivalent length in the element at inclined crack path does not give the correct amount of fracture energy, cf. Section 5.4.5.

6.5 Process region ahead of the crack tip

From the simulations of the short and the long CCS specimens loaded in the MD, it is interesting to notice that the crack opening displacement (COD), δ_t, versus the extent of the process region ahead of the crack tip, R, is initially the same, cf. Fig. 6.17. So initially the same fracture process occurs at the crack tip independently of body geometry, i.e. we have the concept of near-edge autonomy. The definition of near-edge autonomy is that the same events occur near the crack edge in the material, irrespective of structure geometry and load configuration, [5, 13]. It should be pointed out that current methods in fracture mechanics rest on the assumption of autonomy in the region near the crack tip, [15]. So the process region can uniquely be described by one parameter only, irrespective of structure geometry and load configuration. Often the J-integral is chosen for this purpose, i.e. the measure of the fracture energy dissipation to the crack tip. However, it is shown from Fig. 6.17 that when the localized damage zone ahead of the crack tip has extended approximately 3% into the total ligament length $(W-a)$=15 mm, i.e. $R/(W-a) = 0.03$, the short and long specimens give different δ_t vs. R response. This means that the concept of autonomy in a region near the crack edge no longer prevails, and the process region near the crack edge can therefore not generally be described by one unique parameter.

It should be noted that at peak load for the long and short CCS the deviation from autonomy is considerable. At peak load for $2H = 100$ mm the opening displacement is $\delta_t \approx 0.1$ mm, and the extent of the process region of the crack tip, $R \approx 4.1$ mm. And at peak load for $2H = 10$ mm $\delta_t \approx 0.04$ mm and $R \approx 15$ mm.

The simulated results of the process region just ahead of the crack tip are compared with the analytical solution of an infinite cracked plate in tension, i.e. the Barenblatt-Dugdale crack model. The infinite cracked plate problem has been solved and discussed in detail by Andersson and Bergkvist [1] and Rice, [76]. They investigate an infinite cracked plate loaded with a uniform remote stress, σ_∞, under plane stress condition with a crack $2a$ long. Andersson and Bergkvist, [1], studied an isotropic linear elastic material with a descending stress-elongation curve. Rice, [76], used an isotropic linear elastic material with non-hardening plasticity. The solution of the non-hardening model for large scale yielding (LSY) gives the crack opening displacement, δ_t, and the maximal extent of the yielding ahead of the crack

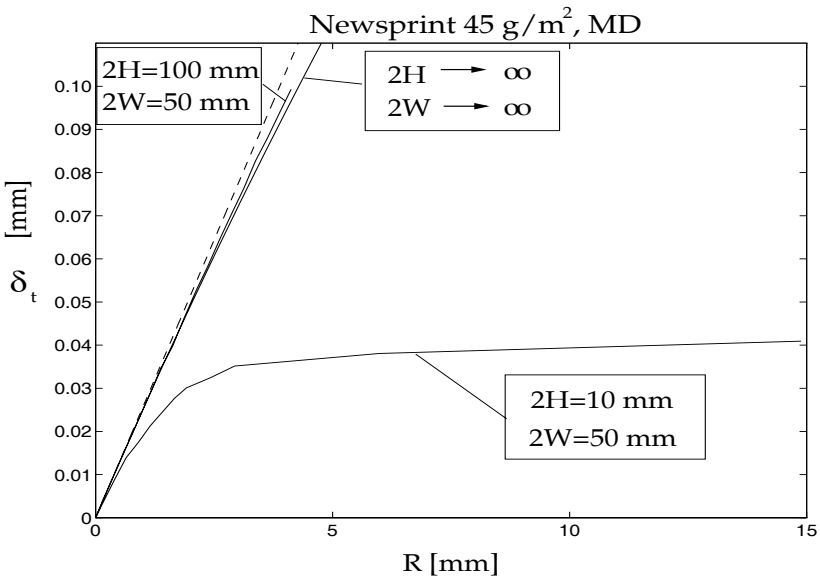

Figure 6.17: *The crack opening displacement (COD), δ_t, versus the extent of the process region of the crack tip, R, into the ligament length.*

tip, R, cf. [76] as,

$$\delta_t = \frac{8\sigma_y a}{\pi E} \ln\left[\sec\left(\frac{\pi\sigma_\infty}{2\sigma_y}\right)\right] = \frac{\pi\sigma_\infty^2 a}{E\sigma_y} + \cdots \tag{6.1}$$

$$R = a\left[\sec\left(\frac{\pi\sigma_\infty}{2\sigma_y}\right) - 1\right] = \frac{\pi^2}{8}\left(\frac{\sigma_\infty}{\sigma_y}\right)^2 a + \cdots \tag{6.2}$$

where σ_y is the yield stress and E is the elastic modules in an anisotropic material.

Combination of Eqs. (6.1) and (6.2) gives the relation between the crack opening displacement, δ_t, and the extent of the yielding zone ahead of the crack tip, R, as

$$\delta_t = \kappa a \ln\left[\frac{R}{a} + 1\right] = \kappa R + \cdots \tag{6.3}$$

where κ is equal to $8/\pi \cdot \sigma_y/E$. The first terms in the Taylor expansion in Eqs. (6.1), (6.2) and (6.3) are the results obtained at small-scale yielding (SSY) for plane stress condition.

The relation between the crack opening displacement, δ_t, and the extent of the yielding zone ahead of the crack tip, R, in Eq. (6.3) is plotted in Fig. 6.17 for both LSY ($2H \to \infty$ and $2W \to \infty$) and SSY (dashed line), for $\kappa = 0.0257$. The value of κ was obtained from simulations of large CCS specimens loaded in the MD. In Fig. 6.17 it is shown that the simulated δ_t-R curve for the long CCS specimen and the

		LEFM	Failure stress	Simulations	Experiments
	$2H$	F_{limit}	F_{limit}	F_{limit}	F_{limit}
	[mm]	[N]	[N]	[N]	[N]
MD	10	177	68.9	69.5	54 - 64
MD	100	83	68.9	47.1	43 - 47
CD	10	64	23.3	23.3 - 24.4	20 - 24
CD	100	44	23.3	22.3	22.7

Table 6.1: *Limit loads.*

LSY relation in Eq. (6.3) with $\kappa = 0.0257$ gives nearly the same result. It is further seen that the SSY solution deviates only slightly from the LSY solution in Fig. 6.17 before instability occurs.

6.6 Limit load estimation

The limit loads derived from the simulations above are shown in Table 6.1 together with the experiments. If it is assumed that the length of the process region at the limit load is either zero, i.e. a point, or equal to the ligament length, $(W - a)$, then a simple estimate of the limit load can be made.

Let us first assume that the process region is point sized at the crack tip. Then linear elastic fracture mechanic (LEFM) methods can be used to establish an estimate of the limit load. The CCS specimens are subjected to uniform displacement perpendicular to the crack line, u. The constitutive relation between the reaction force, F, and the displacement, u, is

$$u = S(A)F \tag{6.4}$$

where $S(A)$ is the compliance stiffness (inverse elastic stiffness) given in Figs. 6.2 - 6.4 and $A = (2W - 2a)t$ is the CCS cross section area. The potential elastic-strain energy under the prescribed displacement, u, is

$$U = \frac{1}{2}Fu = \frac{1}{2}S(A)F^2 \tag{6.5}$$

where Eq. (6.4) has been applied.

Assume next that the crack grows from its initial length, $2a$, to a new crack length, $2(a + \delta a)$. This means that fracture energy has been dissipated in the point sized process region with the result that new crack surfaces have been generated, i.e. $t2\delta a$, where t is the CCS thickness. The loss of potential elastic-strain energy per unit area due to generated fracture surface was assumed by Griffith to be equal to the released elastic energy, [33]. However, much larger energy is dissipated and Orowan, [67], extended Griffith's theory to include the whole energy dissipation, i.e.

$$\frac{dU}{dA} \equiv G_f \tag{6.6}$$

where G_f is the fracture energy discussed in the above chapters. The results in Eq. (6.6) hold only for SSY, [14]. Differentiation of Eq. (6.5) with respect to the area, A, gives the loss of potential elastic-strain energy per unit area as

$$\frac{dU}{dA} = \frac{1}{2}F^2\frac{dS(A)}{dA} \tag{6.7}$$

The LEFM estimate of the limit load is then given by insertion of Eq. (6.6) into Eq. (6.7) and, after some rearrangements, gives, [36],

$$F_{limit} = \sqrt{2G_f\left(\frac{dS}{dA}\right)^{-1}} \tag{6.8}$$

where the changes in the compliance stiffness with respect to creation of new crack surface, dS/dA, are obtained from linear orthotropic elastic finite elemet simulations of the long and short CCS with different crack length 2a, i.e. $2a = 20$ mm, 21 mm and 22 mm. In Table 6.1 the LEFM limit loads are given for the short and long CCS specimens loaded in the MD and the CD. The fracture energy values for newsprint 45 g/m^2 are given in Table 1.1.

If the process region is equal to the ligament length, $(W - a)$, and it is assumed that the stress in the loading direction over the ligament length is equal to the failure stress, T^o, then a simple estimate of the limit load can be made as

$$F_{limit} = T^o(2W - 2a)t \tag{6.9}$$

In Table 6.1 the failure stress limit loads are given for the short and long CCS specimens loaded in the MD and the CD. The failure stress values for newsprint 45 g/m^2 are given in Table 1.1.

All estimates of the limit load in Table 6.1 are shown to overestimate the experimental results. It is seen that the simulations with the cohesive softening model give good or reasonable predictions of the experimentally obtained limit loads. The prediction by the estimated form the failures stress in Eq. (6.9) is shown to be in agreement for the short CCS, whereas it overestimates the long CCS loaded in the MD by approximately 50%. The good estimate for the short CCS may be due to the reason that the principal stresses are more or less constant in the loading direction along the ligament length at the limit load, cf. Fig. 6.11. The LEFM limit load estimates are shown in Table 6.1 to overestimate all of the experimentally obtained limit loads considerably.

Chapter 7

Analysis of perforated opening in a package

7.1 Introduction

The continual demand from the market to have functional opening devices on paperboard-based packages leads to a continual development of new opening devices that fulfill the market request. The technical problem is to fulfill the market request regarding design and functionality and also make sure that the package material preserves the quality of the liquid product inside the package. Damage to the package material that reduces the package's ability to ensure the quality of the liquid product can occur in production or during transportation.

This investigation is focused on the risk of damage in the package material with an opening due to the in-plane web tension in the converting process. The opening in the package material is manufactured by punching out a spline of an arbitrary geometry; unpunched segments on the spline are here called paperboard bridges. Thereafter polymer films and an aluminum foil are laminated onto the paperboard to form the package material. The package material is loaded with a constant web tension of 1000 - 2500 N/m during the converting process.

The resulting laminated package material consists of paper/metal/plastic layers (see Fig. 7.1), which is required to preserve the quality of the liquid product in the package. The individual layers in the laminated package wall have their own advantages and disadvantages [54, 68]. The inner plastic film is used for heat sealability and to prevent chemical interaction with the liquid product, whereas the metal foil is required to retain the aroma of the product, and the paper layer's function is to give the package its strength and stability.

It is important to design the opening in such manner that the package laminate's ability to preserve the quality of the product in the package is preserved. It is therefore important to analyse how the three main layers behave mechanically at a punched opening in the converting process during constant web tension.

This investigation is outlined as follows. The theoretical models of the mechanical properties of the three main layers in the laminated package material are

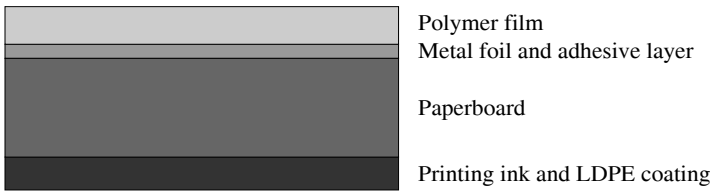

Figure 7.1: *A laminated material for packaging liquid products.*

individually calibrated to experimentally obtained uniaxial tensile tests. The commercial finite element (FE) code ABAQUS/Standard, [39], is used for this purpose. To account for geometric non-linearity, the option NLGEOM is switched on in the analysis. Two constitutive models for the paperboard are used in the evaluation. These are the in-plane elastic cohesive softening (ECS) model and the anisotropic elastic-plastic model by Karafillis and Boyce [49]. A punched paperboard with a U-shaped geometry containing four bridges is experimentally investigated at in-plane tension loading and compared with the FE simulations. Thereafter the laminated package material with a designed punched geometry with bridges is analysed at the web tension of 2100 N/m.

7.2 Calibrations of the constitutive models

The in-plane uniaxial behavior of the individual main layers in tension has been measured for the metal, plastic and paperboard by Magnusson and Östensson [57], Lau [54] and Persson [73], respectively. The experimentally obtained load-elongation curves on the three main layers are numerically calibrated to the Ducker-Prager, [103], and the Gurson material models, [101], for the inner plastic layer and the metal layer, respectively. The Persson experimental paperboard 240 g/m^2 data, [73], and tests by the writer are calibrated to the Karafillis-Boyce (KB) model, [49], and the ECS model, respectively, according to the procedure described in Chapter 5.

7.2.1 Calibrations of the metal foil model

The use of the aluminum foil in the package material is due to its good barrier properties for retaining the aroma of the product. However, due to outer loads, the pinholes (1-200 per m^2) in the aluminum foil may grow and nucleate and then reduce the ability of being a good barrier. To account for this effect in the simulations, a porous metal plasticity model is chosen, i.e. the Gurson porous plasticity model, [101]. The dependent field variables and the void nucleation parameters are listed in Table 7.1, cf. [77, 101]. The material model is calibrated against the uniaxial tensile data by Magnusson and Östensson, [57], in Fig. 7.2. Figure 7.2 shows the nominal uniaxial tensile stress-strain curve for the 6.8 μm thick aluminum foil, cf.

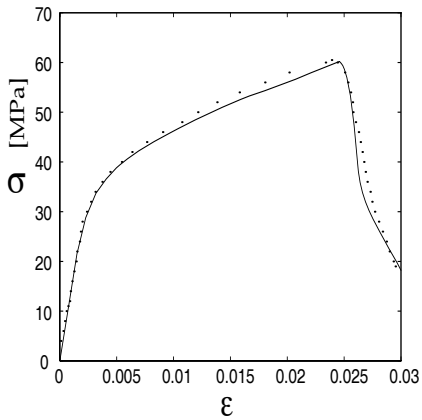

Figure 7.2: *Uniaxial stress-strain curve for the metal foil. The solid line is data from Magnusson and Östensson and the dotted line is the calibrated Gurson material model.*

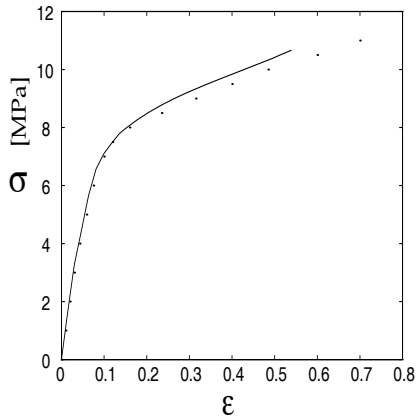

Figure 7.3: *Uniaxial stress-strain curve for the PE film. The solid line is data from Lau and the dotted line is the calibrated Drucker-Prager material model.*

[57]. The specimen used was 15 mm wide and the elongation was measured by a strain gage extensometer with a gage length of 50 mm. The measured value on the elastic modulus is 13 GPa, and the yield and ultimate stress are 23 MPa and 59 MPa, respectively. Note that these data deviate from what is normally obtained from tests using round tensile bars of aluminum. This may be explained from the observation that nonhomogenous deformation and buckles are present on the thin specimen, and that during the tensile test out-of-plane movement is allowed, which allows both in-plane and shear mode failure to occur. However, any thorough investigation of this phenomenon that explains the discrepancy in detail between the aluminum foil and round bar is not known to the author. It is observed from photos, cf. [57], of the ascending part of the nominal stress-strain curve in Fig. 7.2 that slip planes are visible. The descending part of the nominal stress-strain curve is supposed to be due to separation of the gains and matrix in the foil, see e.g. [18]. The free edges in each sample are cut, which causes the edges to deform plastically. This procedure increases the possibility of initiation of micro-cracks at the edges during the test.

It is well known that the fracture energy dissipation is affected by the finite element size if the material softening is characterized by the descending part of the stress-strain curve [42]. So, the element size in the calibration of the Gurson material model will affect the descending part of the simulated nominal stress-strain curve in Fig. 7.2. Hence it is important, indeed crucial, that the element size used in the calibration of the simulated descending part of the nominal stress-strain curve is the same as in the localized zone in the finite element simulations in Section 7.4.

E, GPa	13.0
ν	0.30
σ_y, MPa	23.0
σ_u, MPa	59.0
q_1	1.5
q_2	0.82
q_3	2.25
ϵ_N	0.1
s_N	0.05
f_N	0.4

Table 7.1: *The parameters to the Gurson material model.*

E, MPa	102.0
ν	0.30
σ_y, MPa	3.17
Friction angle	35°
Dilation angle	0.0^o

Table 7.2: *The Drucker-Prager parameters for the LDPE material.*

7.2.2 Calibration of the PE-type model

Figure 7.3 shows the experimentally measured uniaxial tensile stress-strain curve (solid curve) for the low density polyethylene (LDPE) specimen, cf. [54]. The specimen used in the experiments was 15 mm wide and 35 μm thick, and the elongation was measured by a strain gage extensometer with a gage length of 60 mm, [54]. The Drucker-Prager constitutive model is used to describe the measured stress-strain curve in Fig. 7.3, cf. [103]. The parameters required for the Drucker-Prager model are listed in Table 7.2, and are the elastic modulus, E, the Poisson's ratio, ν, the yield stress, σ_y, the friction angle and the dilation angle, cf. [39]. The numerical value of the parameters in Table 7.2 are chosen such that uniaxial tension simulation of the LDPE specimen by the Drucker-Prager model fits the measured stress-strain curve in Fig. 7.3. Figure 7.3 shows the simulated stress-strain curve (dotted curve), together with the measured stress-strain curve (solid curve) and it is seen that the curves are very similar.

7.2.3 Calibration of the paperboard models

Calibration of the KB model

The experimental investigation of paperboard 240 g/m^2 by Persson [73] can be used as a basis for developing a constitutive model. The experimental data in [73] were measured on strips that exhibit immediate rupture at the failure load and include both the in-plane and out-of-plane paperboard properties. Figure 7.4 shows the in-plane tensile data reported by Persson [73] as solid lines. From uniaxial tension tests in the MD, $\sigma_1(\epsilon_1)$ and $\sigma_1(\epsilon_2)$ are recorded and from uniaxial tension tests in the CD, $\sigma_2(\epsilon_1)$ and $\sigma_2(\epsilon_2)$ are recorded. In Fig. 7.4 the experimental in-plane shear stress-shear strain curve, $\sigma_6(\epsilon_6)$, is obtained from in-plane loading at 45 degrees to the MD, cf. [73].

The KB model, [49], is calibrated to Persson's experimental data by following the procedure presented in Chapter 5. The dotted curves in Fig. 7.4 are the stress-

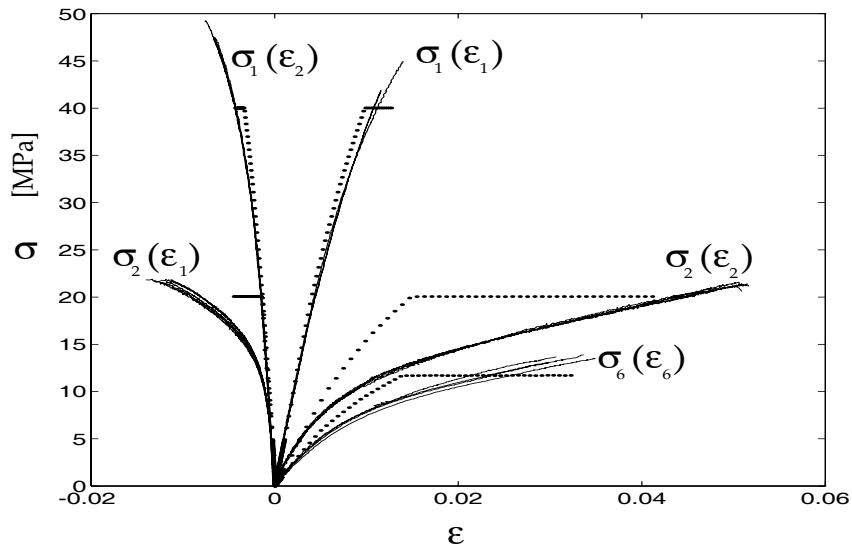

Figure 7.4: *The in-plane response of the paperboard 240 g/m^2; the solid lines represent the experimental recorded curves and the dotted lines are the KB model.*

strain curves from simulations with the KB model of a strip uniaxially loaded in the MD and CD and also shear loaded. It is seen in Fig. 7.4 that the KB model is able to capture some of the overall behavior of the paperboard. After the failure stress is reached, the KB model assumes the material to behave as an anisotropic plastic material with the hardening equal to zero.

Calibration of the ECS model

If the paper strips tested are shortened, the paper will show a "non-immediate" rupture and eventually the paper strip will give a stable evolution of the failure zone, cf. Chapter 2. This gives an ascending and a descending part of the load-elongation curve, where the ascending part has an elastic-plastic hardening behavior and the descending part an elastic-plastic-damage softening behavior, cf. Chapter 2. The fracture energy obtained from the stress-crack widening curve is then a measure of the resistance to fracture, i.e. a high fracture energy value gives a higher resistance for crack propagation. The in-plane stress-widening curves due to uniaxial tension loading of the paperboard 240 g/m^2 in the MD and CD are shown in Fig. 7.5. The tests followed the procedure described in Chapter 3.

A constitutive model that captures the elastic and crack widening behavior is the ECS model. The ECS model is an in-plane anisotropic elastic cohesive softening model and is discussed in detail in Chapters 4 and 5. The failure criterion and

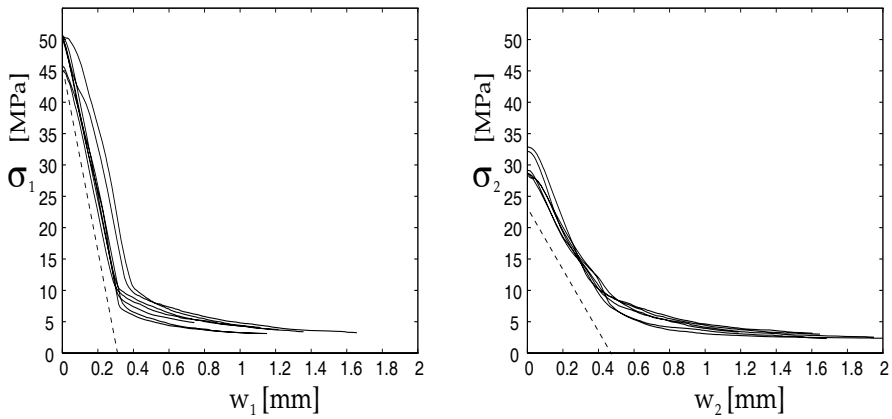

Figure 7.5: *The in-plane stress-crack widening curve of paperboard 240 g/m^2, uniaxially loaded in the MD (left figure) and CD (right figure). The solid lines represent the experimentally recorded curves, and the dashed lines are the ECS model.*

the failure potential are uniquely given from the failure strength of paper strips that immediately rupture. The failure strength parameters needed are the values from uniaxial tensile and compression tests in the MD and CD together with the shear and equibiaxial tensile strength and the plastic Poisson's ratio at failure. The cohesive modulus of the descending stress-crack widening curve in the MD and CD is implemented in the smeared crack constitutive model as linear descending curves in the same manner as is shown in Fig. 2.11. Figure 7.5 shows the linear descending curves in the ECS model as dashed lines. The cohesive shear modulus is estimated from the cohesive moduli in the MD and CD, cf. Eq. (4.39). In Tables 5.2 and 5.3 the calibrated elastic and strength parameters are listed. For further discussions regarding the calibration see Chapter 5.

7.3 Experiments and simulations of a board in tension

A paperboard sheet in tension with a U-shaped opening geometry with four paperboard bridges, Fig. 7.6, is studied in order to compare the agreement between the experimental observations and the finite element simulations. The paperboard tested had no metal foil nor any plastic film. In Fig. 7.7 the U-shaped opening geometry is shown together with the four paperboard bridges denoted I, II, III and IV. The paperboard sheet is $W = 167$ mm wide, $L = 200$ mm long and 390 μm thick, with the punched U-shaped opening in the center, cf. Fig. 7.6. The U-shaped opening slit in Fig. 7.6 is 0.2 mm wide and the four paperboard bridges are 0.7 mm wide, [24]. The paperboard sheet in Fig. 7.6 is subjected to a uniform elongation, u,

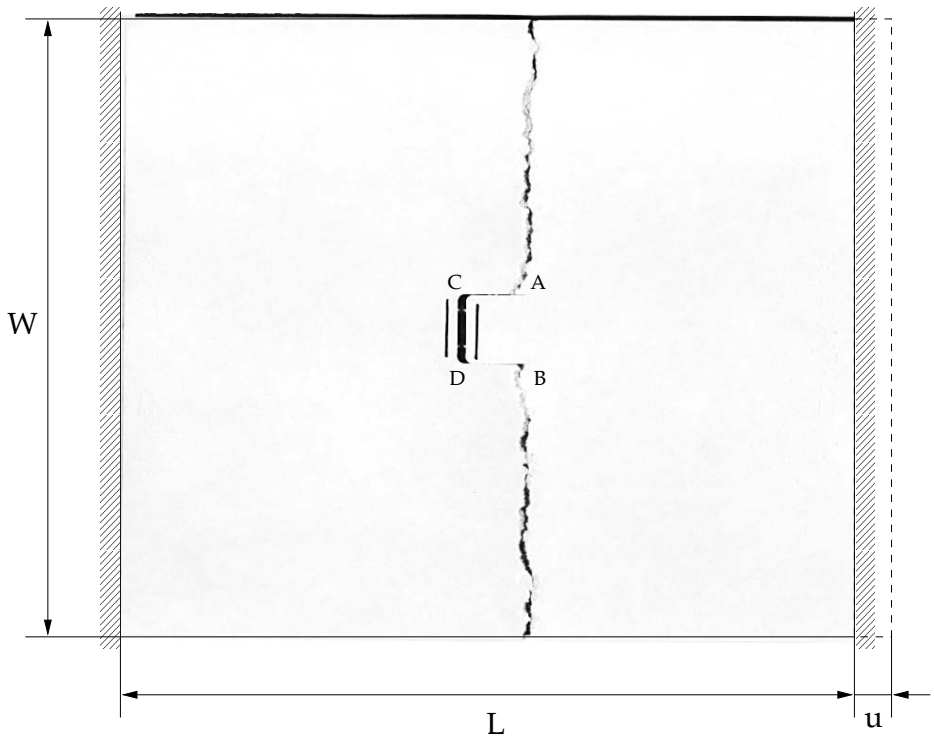

Figure 7.6: *Photo of the specimen with the U-shaped opening.*

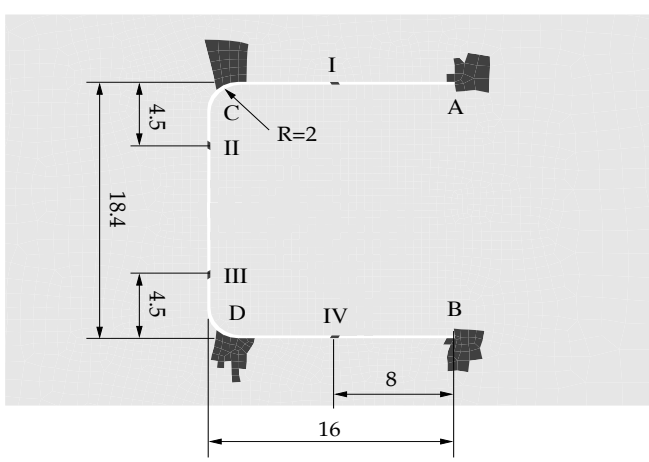

Figure 7.7: *The U-shaped opening. The black regions indicate which elements in Fig. 7.13 have the ECS material properties. The measures are given in millimetres.*

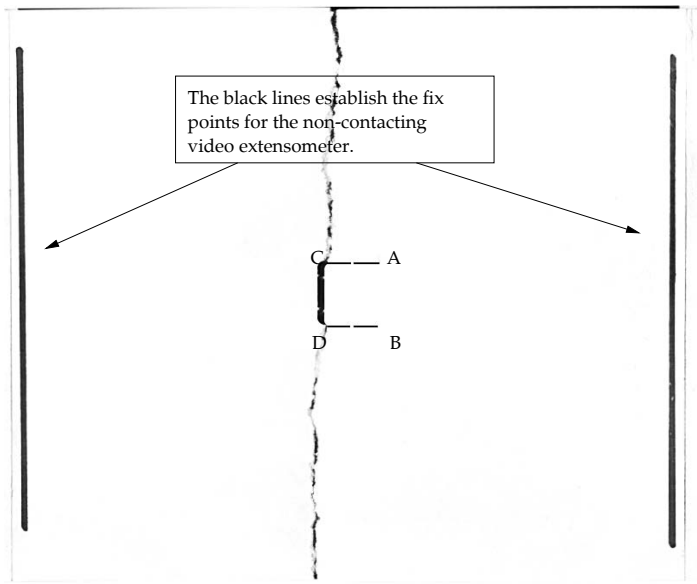

Figure 7.8: *Photo of the specimen with the U-shaped opening.*

in the MD. The paperboard samples were held between two parallel steel plates. To obtain good adhesion a tape with glue on both sides was placed between the steel plates and the paperboard samples.

7.3.1 Experimental setup

The tension tests were carried out in the Instron universal testing instrument (model 4502) with a 10 kN tension-compression load cell. The load was recorded by the load cell, and the displacement by an Instron 2663 series non-contacting video extensometer. The displacement curves were recorded between the black lines at the grips and at the U-shaped opening as shown in Fig. 7.8 and in Fig. 7.9. The video extensometer established two points from the black lines at the symmetry line, i.e. $W/2$, from which the elongation is recorded. The crosshead speed used throughout the tests was 20 mm/min. The tests were made at $50 \pm 2\%$ relative humidity and at $23 \pm 1°$ C.

7.3.2 Experimental observations

The specimens with the U-shaped slits were loaded until ultimate failure occurred. It is observed from the experiment that fracture first occurs at the paperboard bridges and, secondly, fracture develops either at the end of the slits A or B and/or at the slits' radius C or D, cf. Figs. 7.6, 7.8 and 7.9.

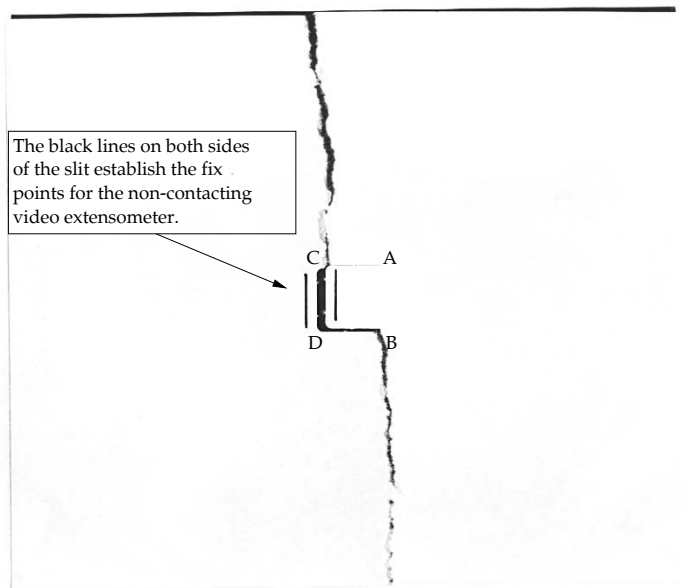

Figure 7.9: *Photo of the specimen with the U-shaped opening.*

The experimental result for the web tension, T_w, vs. elongation, u, curve is shown in Fig. 7.10. The elongation shown is measured between the black lines in Fig. 7.8. The web tension vs. elongation curve is linear up to $\sim$ 7500 N/m and thereafter the relation becomes more and more non-linear until unstable fracture occurs at $\sim$ 11 000 N/m. Note that the web tension vs. elongation curve has a shape similar to that of the uniaxial stress-strain curve in the MD in Fig. 7.4. However, due to the U-shaped slits the failure load is approximately 30% less than is predicted from the uniaxial stress-strain curve in the MD, cf. Fig. 7.4.

One curve representative of four experimentally obtained web tension vs. slit opening displacements, u_s, is shown in Fig. 7.11 as solid curves, and the displacement is measured between the black lines in Fig. 7.9. From the web tension vs. slit opening displacement curves, the linear part (not easily seen due to the quality of the solid curves) ends at the web tension of $\sim$ 2000 N/m, and thereafter the curve becomes more and more non-linear. The non-linear part of the curve is primarily due to the fracturing in bridges I-IV and at the end of the slits, A and B, and/or at the slits' radius, C and D, cf. Fig. 7.7.

7.3.3 Comparison with finite element simulations

The mesh used in the simulation is shown in Fig. 7.12, and consists of four node elements with 2x2 Gauss point integration rule if the KB model is used or with reduced integration if the ECS model is used. Figure 7.13 shows a zoom of the

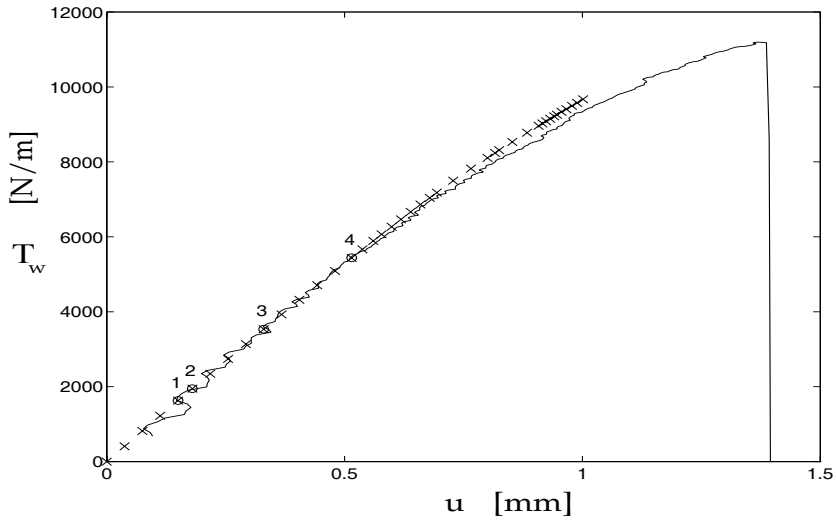

Figure 7.10: *The web tension vs. elongation curve obtained from experimental setup of the specimen in Fig. 7.6. The 'x' dotted line is from the simulations with the combined model.*

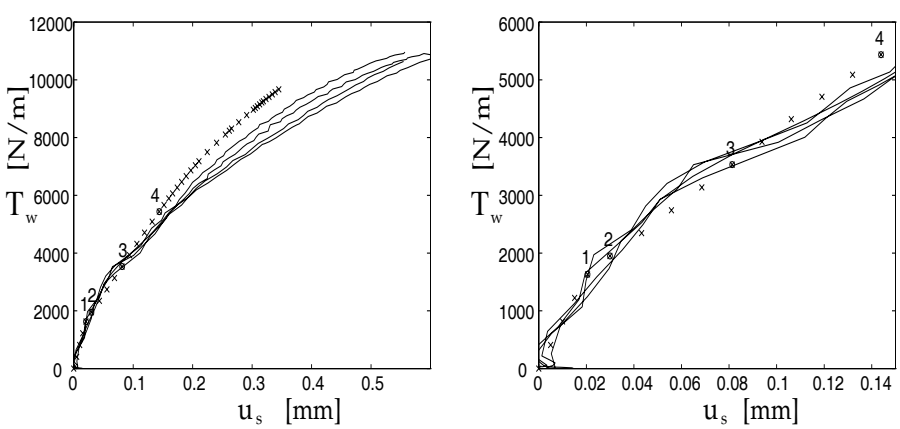

Figure 7.11: *The web tension vs. slit opening deformation is shown. The solid lines are from the experiments. The 'x' dotted line is from the simulations with the combined model. The right-hand diagram shows an enlargement of the left diagram.*

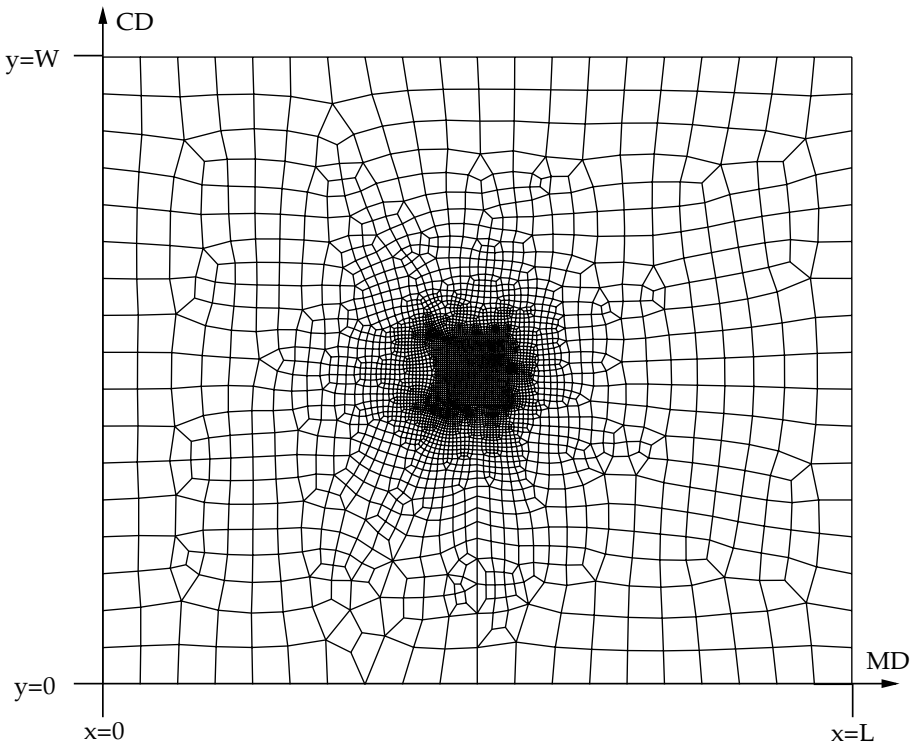

Figure 7.12: *The mesh of the specimen in Fig. 7.6.*

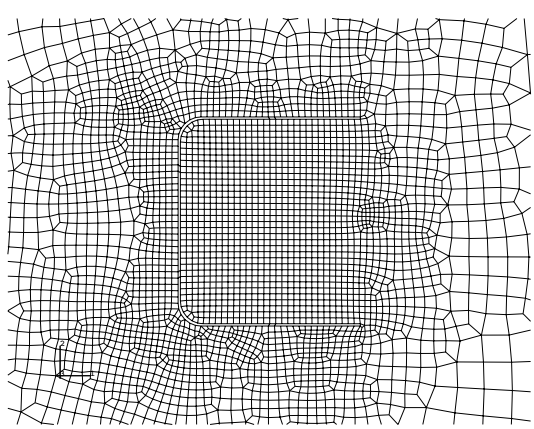

Figure 7.13: *Mesh zoom of the specimen in Fig. 7.12.*

elements around the U-shaped opening in Fig. 7.12.

Numerical simulations of the experiments, either with the ECS model assigned to all elements in the mesh or with the KB model assigned to all elements in the mesh, reveal that both the models initially give the same results, i.e. in the elastic region. Thereafter in the web tension interval of 2500 - 3500 N/m the simulation with the KB model assigned to all elements in the mesh follows the experimental T_w-u_s curve better than the simulation with the ECS model assigned to all elements in the mesh. However, in the web tension interval of 3500 - 5000 N/m the reverse is true. This is not unexpected, since both the ECS model and the KB model have different hardening and softening properties. The ECS model represents the hardening by an orthotropic linear elastic stress-strain relation, and the softening by an orthotropic linear descending stress-widening relation, whereas the KB model represents the hardening by an orthotropic elastic-plastic stress-strain relation and the softening region by plasticity with the hardening equal to zero.

In order to obtain better agreement between the simulation and the experimental results, the two paper material models are combined. The regions where failure occurs are modelled with ECS material, as is indicated in Fig. 7.7 (the black regions). The regions with the ECS model are not in symmetry; this is due to the fact that the simulations for this configuration followed the measured T_w-u curves to a slightly higher web tension than for a configuration with symmetry regions. The rest of the elements in the model, cf. Fig. 7.12, use the KB model. However, as mentioned in Chapter 5, this type of combination of the ECS model and KB model may underestimate the failure stress. The simulations with the ECS and KB models of the experimental setup are shown together with the measurements in Fig. 7.10 and Fig. 7.11.

It is seen from the simulations, both for simulations with the combined model and for simulations where all elements in the mesh are given the material properties of the ECS model, that the fracture in the bridges begins first at bridges II and III, cf. Fig. 7.7, at a web tension of 1630 N/m, (no. 1 in Figs. 7.10 and 7.11). Thereafter shear fracture occurs in bridges I and IV at a web tension of 1950 N/m (no. 2 in Figs. 7.10 and 7.11), and at a web tension of 3530 N/m (no. 3 in Figs. 7.10 and 7.11) the fracture begins at the end of the slits, i.e. at points A and B in Fig. 7.7. Finally, fracture is initiated at the slits' radius, C and D in Fig. 7.7, at a web tension of 5437 N/m (no. 4 in Figs. 7.10 and 7.11). The simulation ends at a web tension of 9670 N/mm. The reason for this is that the ECS model is only applied to the elements near the region where fracture first occurs, cf. Fig. 7.7.

In Figs. 7.14, 7.15 and 7.16 the plane stress components around the U-shaped opening are shown at web tensions of 1630, 1950, 3530 and 5437 N/m for simulations with the combined model. It is clearly seen that the stresses are concentrated around the fracturing zones, i.e. I - IV and A - D in Fig. 7.7.

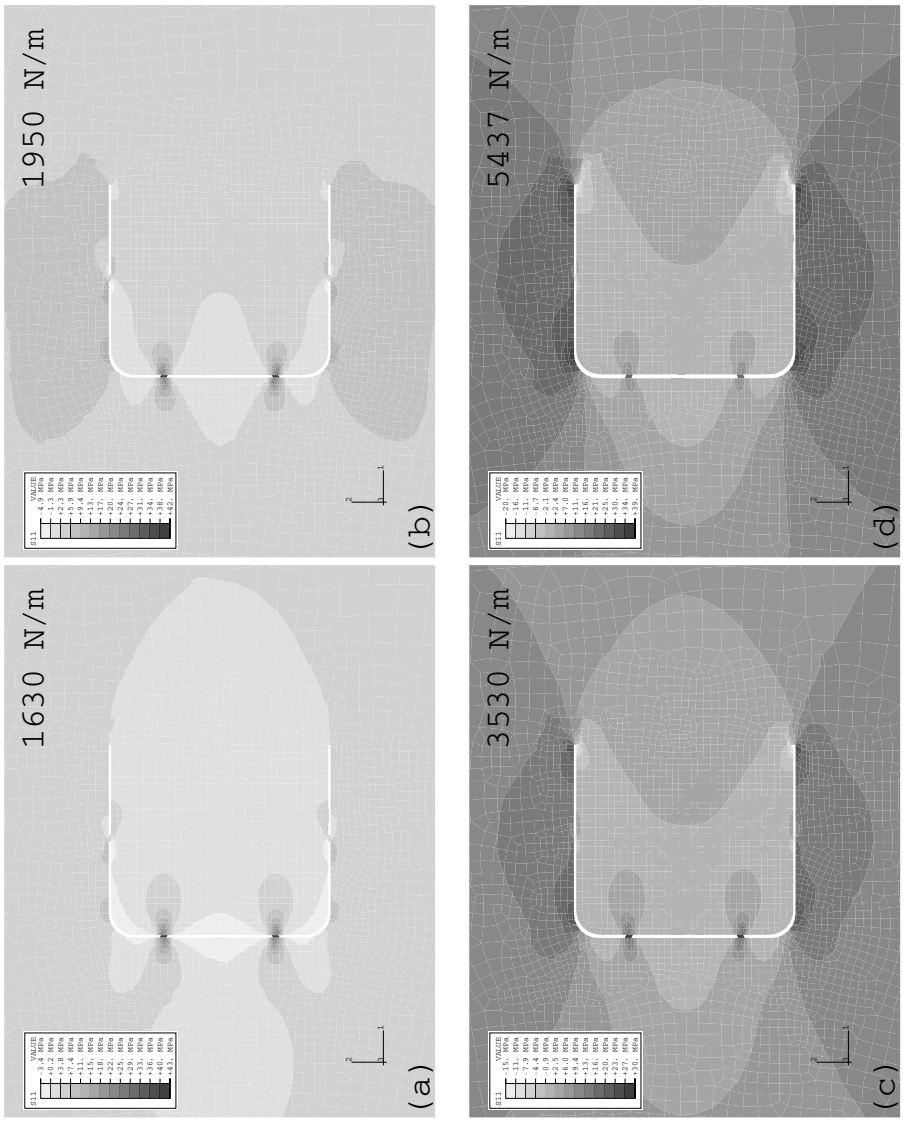

Figure 7.14: *The stress in the MD, σ_1, at the U-shaped opening. (a): The σ_1 at a web tension of 1630 N/m. (b): The σ_1 at a web tension of 1950 N/m. (c): The σ_1 at a web tension of 3530 N/m. (d): The σ_1 at a web tension of 5437 N/m.*

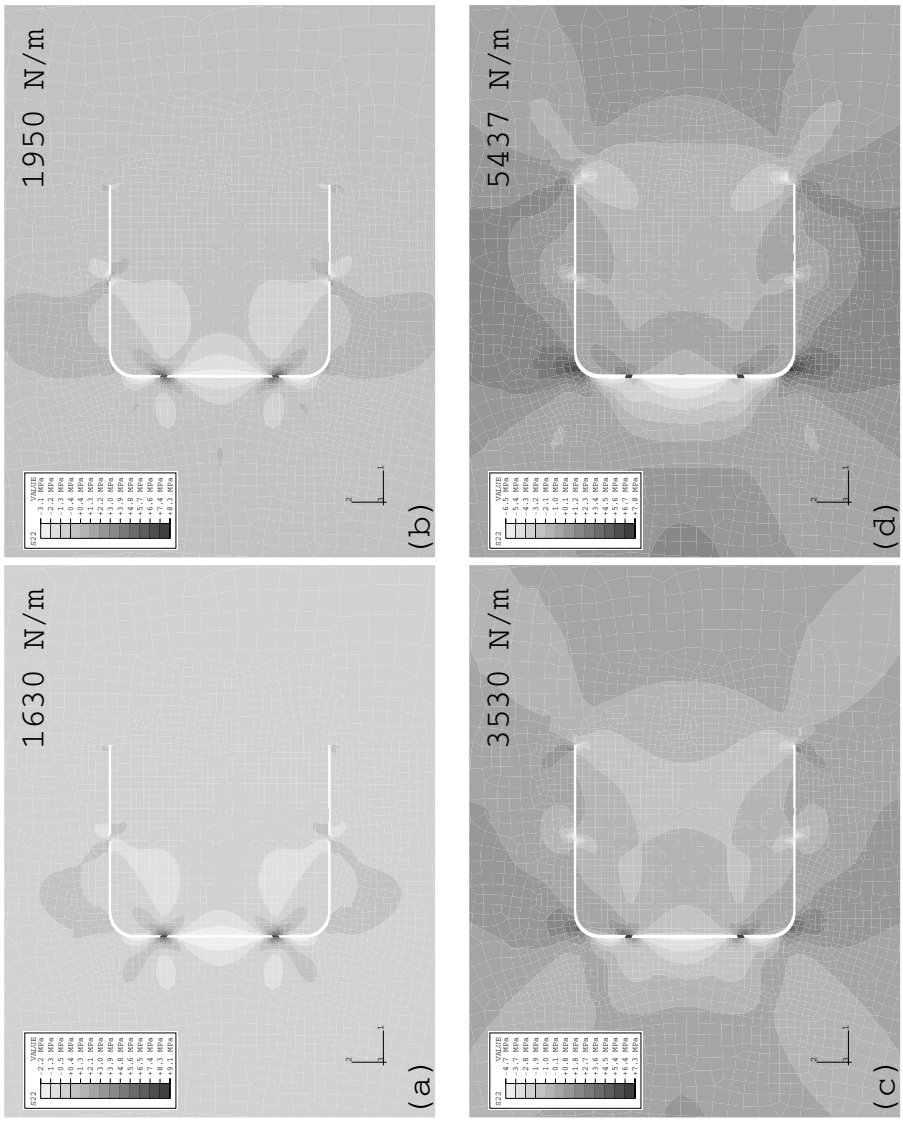

Figure 7.15: *The stress in the CD, σ_2, at the U-shaped opening. (a): The σ_2 at a web tension of 1630 N/m. (b): The σ_2 at a web tension of 1950 N/m. (c): The σ_2 at a web tension of 3530 N/m. (d): The σ_2 at a web tension of 5437 N/m.*

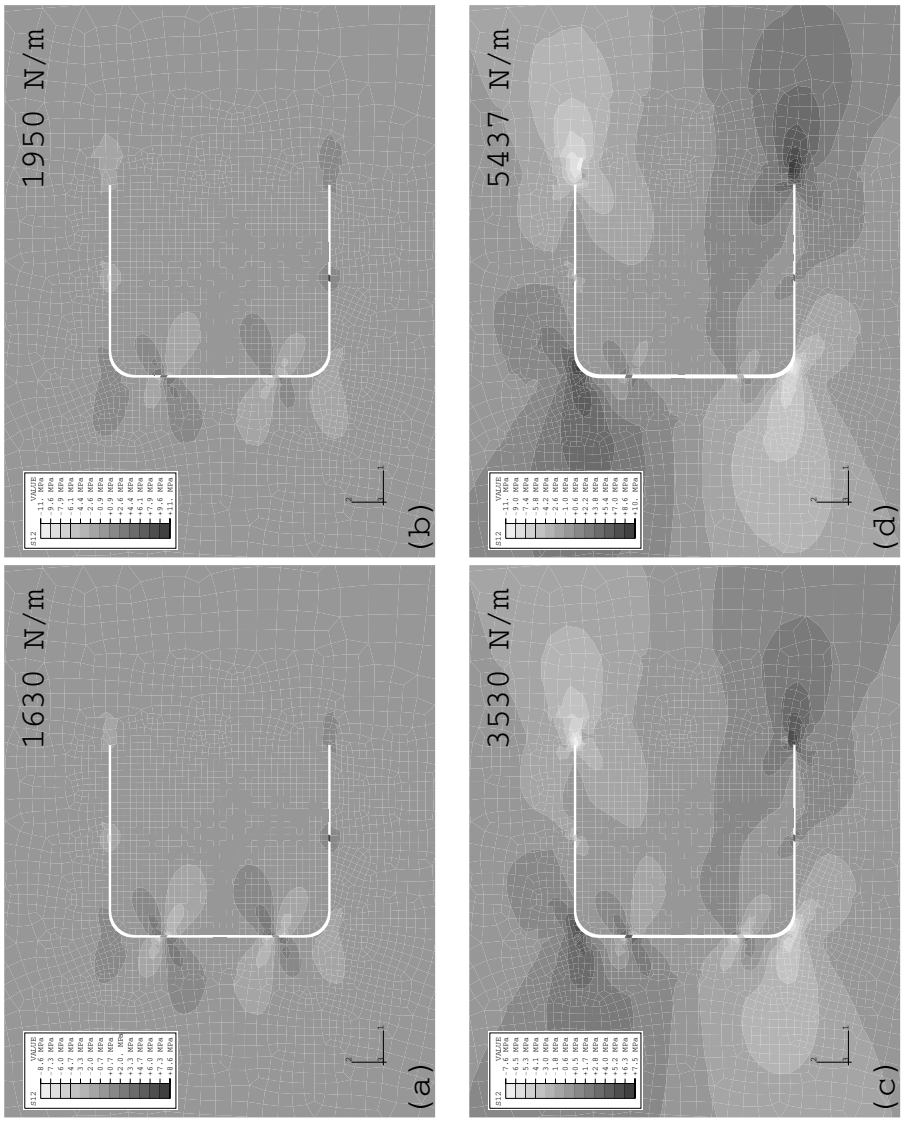

Figure 7.16: *The shear stress, σ_6, at the U-shaped opening. (a): The σ_6 at a web tension of 1630 N/m. (b): The σ_6 at a web tension of 1950 N/m. (c): The σ_6 at a web tension of 3530 N/m. (d): The σ_6 at a web tension of 5437 N/m.*

Case	Board [μm]	Metal [μm]	LDPE [μm]	$(u_s)_{max}$ [μm]	f [%]
1	390	9	30	3.56	1.74
2	390	12	40	2.47	0.44
3	390	12	30	2.52	0.51

Table 7.3: *The maximum deformation in the middle of the front slit, $(u_s)_{max}$, and the void volume fraction, f, at a web tension of 2100 N/m for different thicknesses of the package laminate.*

7.4 Simulation of a package laminate in tension

The package structure is produced in the converting process where the paperboard, polymer film and metal foil are laminated together. As was mentioned in the introduction, the paperboard, polymer film and metal foil have their own advantages and disadvantages. It is important that all of these layers preserve their functionality throughout the converting process. During the process the web tension is between 1000 and 2500 N/m, and it is therefore important to design opening geometry so that no damage will occur in the layers due to the web tension.

The laminated package material, with an axehead-shaped opening geometry with bridges, is here studied at the web tension of 2100 N/m. The axehead-shaped opening consists originally of fourteen paperboard bridges, where four are in the front with a width of 0.4 mm and the rest have a width of 0.7 mm, cf. Fig. 7.17. A sensitivity analysis is made on the package web in order to investigate how the polymer film, metal foil thickness and width and number of paperboard bridges affect the results. The metal and polymer layer thicknesses are changed in the simulations according to Table 7.3.

The package geometry in the simulation is the same as the one used in the experimental setup above, i.e. the width is $W = 167$ mm and length is $L = 200$ mm, and the punched opening is located in the center. The material models used in the simulation were the Gurson [101] model for the metal layer, Ducker-Prager [103] model for the plastic layers and the ECS models for the paperboard layer. The Gurson, Ducker-Prager and ECS model calibrations are found in Section 7.2. The geometry model consisted of three meshes, one for each of the three models, but the elements in the meshes shared common nodes. The elements in the meshes for the Gurson and Ducker-Prager models were four node elements with 2x2 Gauss point integration, and the elements in the mesh for the ECS model were four node elements with reduced integration. We are interested to know how the package behaves in the converting process with a web width of 1800 mm. To avoid modelling the entire web width consisting of nine packages in a row, it will be assumed that the package is located in a web of infinite width. This means that the boundary conditions used in the finite element model are the following: In the MD $u_1 = 0$ at $x = 0$ and $u_1 = u$ at $x = L$, whereas in the CD $u_2 = 0$ at $y = 0$ and $u_2 = 0$ at $y = W$, cf. Fig. 7.12.

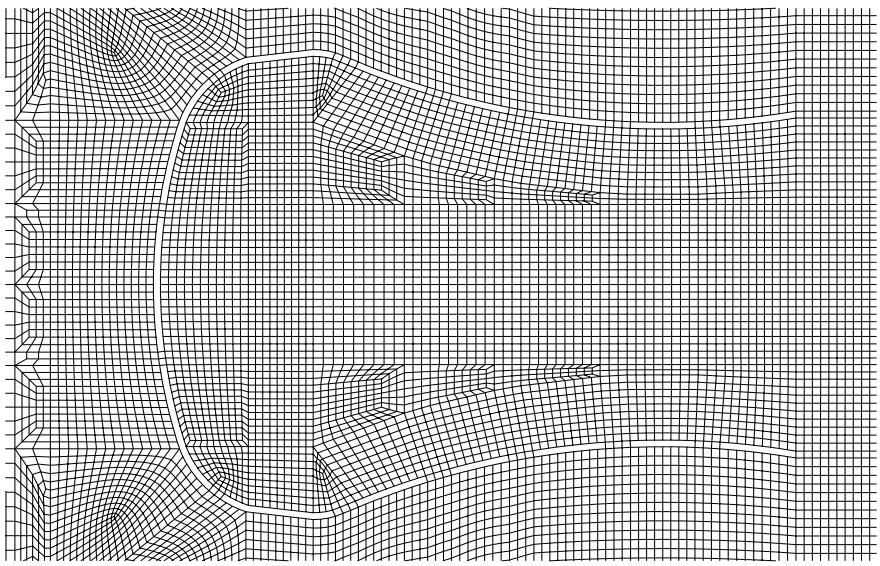

Figure 7.17: *Mesh zoom, showing the axehead-shaped opening. Mesh made by M. Knutsson.*

We shall investigate how the thicknesses of the metal and polymer layers affect the laminated opening. The reference thicknesses of the paperboard, metal foil and polymer film are 390 μm, 9 μm and 30 μm, respectively. The reference laminate is referred to as case 1 in Table 7.3. From the simulation of case 1, in Table 7.3, it is obtained that the maximum effective stresses for the paperboard, metal foil and polymer film are 9.2 MPa, 39 MPa and 3.1 MPa, respectively. All these values are below the failure strength of the paperboard, and are concentrated on the slits in the respective materials. However, a closer examination of the metal foil reveals that damage has occurred in the front slits, cf. Fig. 7.18, i.e. the material has been damaged. It is found that the maximum void volume fraction, f, and the relative density, r, in the front slits of the metal foil are 1.74 % and 0.982, respectively. The void volume fraction is defined as the ratio of the volume of voids to the total volume of the material, and the relative density is defined as the ratio of the volume of solid material to the total volume of the material, i.e. $r = 1 - f$. Note that for an undamaged metal foil the void volume fraction is zero and the relative density is equal to one. The maximum deformation in the slit is 3.56 μm and is found in the middle of the front slits, cf. Fig. 7.19. If the metal foil is increased from 9 μm to 12 μm, cf. case 3 in Table 7.3, then the simulation shows that the maximum f decreases to 0.51 % and the relative density increases to 0.994, i.e. if the metal foil is increased by 33 % then the maximum f decreases by 71 %. However, if the polymer film thickness is increased, no significant changes are noticed between case

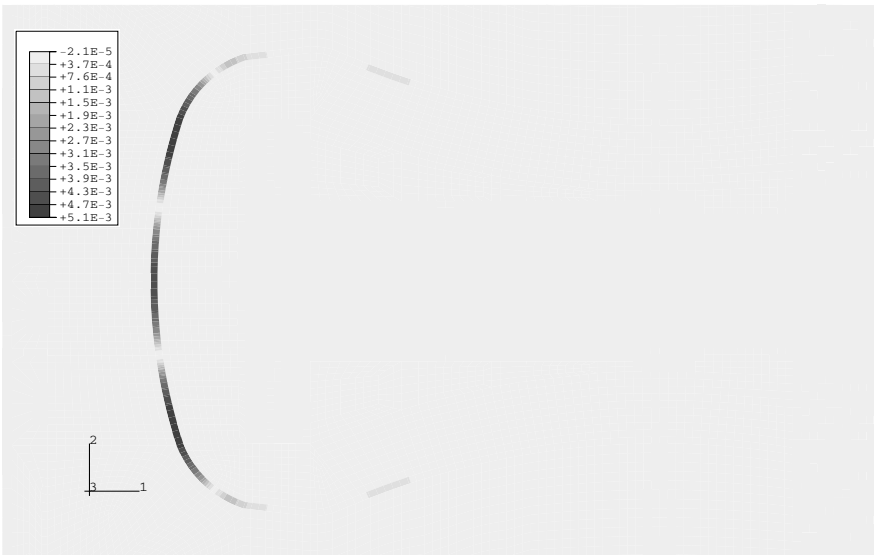

Figure 7.18: *The void volume fraction in the slits of the axehead-shaped opening at a web tension of 2100 N/m, case 3 in Table 7.3.*

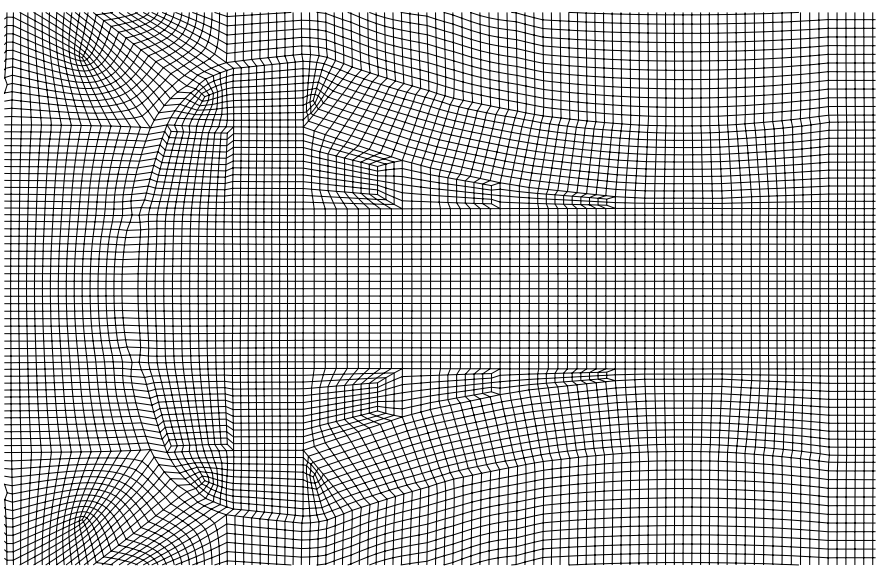

Figure 7.19: *The deformation of the axehead-shaped opening.*

2 and case 3 in Table 7.3.

The numbers and widths of the paperboard bridges are changed in the analysis in order to see if this can reduce the damage in the metal foil. However, the thicknesses of the package layers are the same as in case 1. Firstly, three new front bridges, 0.4 mm wide, are placed between the four front bridges. The simulation reveals that the maximum f decreases to 0.42 % and the relative density increases to 0.995 compared to the reference laminate, case 1 in Table 7.3. Secondly, four front bridges in the referent laminate are increased to a width of 0.8 mm. The simulation gives as a result that no significant changes are noticed in comparison to the reference simulation, i.e. case 1.

The conclusion from the simulated cases is that the metal layers for all the studied cases exhibit damage in front of the slits. It is also shown that the damage in the metal layer in the front slits decreases by approximately the same amount if three paperboard bridges are added in the front slits or if the metal foil thickness increases from 9 μm to 12 μm.

Chapter 8

Concluding remarks

8.1 Summary

It has been reported in the literature [19, 21, 32, 43, 93] that the failure mechanism in paper is related to the length of the uniaxially tested paper strip. If the paper strip is of sufficient length the paper will rupture in a brittle manner. Further shortening of the paper will show a "non-immediate" rupture [32] and eventually the paper strip will give a stable evolution of the failure zone [19, 21]. However, little attention seems to have been devoted to this phenomenon, despite its fundamental impact on fracture and damage in paper. The work described in this thesis has been devoted to this subject.

The work includes experimental, theoretical and numerical parts. The experimental work comprises testing of material properties, proposal of a test method and tests for verification. The theoretical and numerical parts include development of a material model for in-plane fracture analysis, implementation in a finite element code and a few applied fracture analyses. Three different paper types have been tested, namely newsprint, kraft paper and paperboard.

The descending branch of the uniaxial tension test curve can be divided into two phases. In its first phase the damage evolution will localize in the paper strip, until an almost free fracture surface has formed. The fracture in this phase is predominantly in the form of bond failure between the fibers [48, 70, 80]. The paper strip is now held together through single fiber bridges, and the second phase consists of pulling out these fibers, until the paper strip has been separated into two paper strips [12].

The observed fracture mechanism indicates that the measured elongation does not correspond to a homogenous deformation in the paper strip. Instead the total elongation of the paper strip, u, can be thought of as the sum of the local deformation in the fracturing damage band and a uniform strain outside the damage band. The strain outside the damage band decreases during the course of fracture due to the decrease in stress. Accordingly, fracture can be assumed to take place in the narrow band while the other part of the paper strip is unloading. On the analogy of this description of failure kinematics, the recorded stress can be thought of as a cohesive

stress, $\sigma(w)$, acting across the narrow fracture band. The widening of the damage band, w, is defined as the total elongation, u, subtracted from the uniform elongation of the relaxing undamaged part of the paper strip, ϵL, i.e. $w = u - \epsilon L$.

The $\sigma(w)$ curve shows the in-plane fracture properties of the paper. The fracture energy of the material, which is of great importance for the resistance to propagation of a crack, can be obtained from the $\sigma(w)$ curve. The fracture energy, failure strength and initial elastic modulus are shown to depend on the material orientation direction. From the tested material parameters it is possible to define an intrinsic length of the material [42]. For paper this length is direction dependent. It is related to the size of the fracture process region at the tip of a crack and it is also related to the length dependence of the fracture performance of the paper strip in uniform tension.

Structural failure in paper is here modelled with the cohesive crack approach, where the damage in the paper is smeared out in one finite element. With this as a base, an irreversible anisotropic cohesive crack constitutive model is developed for analysis of in-plane fracture of paper. This elastic-cohesive softening model rests on the concept of a failure criterion and a failure potential. During the course of fracture the size and shape of the failure criterion changes. The failure potential gives the orientation of the fracture band. This orientation is constant during the course of fracture.

The constitutive model is formulated for numerical calculations by the finite element method, taking into account that the size of each strain increment is finite. The developed constitutive routine is implemented as a user's subroutine to the commercial finite element code ABAQUS/Standard, [39]. Using the smeared crack approach, a length measure must be assigned to each element. In the actual code the square root of the element area is used. This means that the active elements should be rectangular and of small aspect ratio [39].

The constitutive model is calibrated to newsprint 45 g/m^2 and paperboard 240 g/m^2. The cohesive crack model is also able to describe the transition from unstable to stable failure of the tensile specimens without any initial crack.

A rectangular sheet containing a central crack is analysed in order to investigate how well the developed model is able to describe experimental observations of the CCS specimen. It is found that the limit loads and size effects are picked up very well by the developed model. The size of the fracture process zone is found to be very large as compared to the length of the crack and the ligament.

The in-plane mechanical behavior of a punched package material due to the web tension in the converting process is discussed. It is important that each layer's functionality is intact throughout the converting process, in order to preserve the quality of the liquid product in the package. A web with an axehead-shaped opening, which in the converting process is loaded by a web tension of 2100 N/m, is simulated to obtain a better understanding of how the individual layers are affected by changes of layer thickness and numbers of paperboard bridges and their widths.

The material models used in the simulation of the designed opening were the Gurson [101] material model for the metal layer, Ducker-Prager [103] material model for the plastic layers, and Karafillis-Boyce [49] and elastic-cohesive softening mate-

rial models for the paperboard layers. The material models were calibrated to the measured load-elongation curves obtained for metal by Magnusson and Östensson [57], for plastic by Lau [54] and for paper by Persson [73] and by the writer.

8.2 Conclusions

For obtaining the fracture energy and the fracture softening properties of paper it is important that specimen types and procedures proposed are relevant, simple and easy to use. It was found for uniaxial load-elongation tension tests that the most repeatable measure in comparison to practical convenience can be summarized in the following items.

- The ascending part of the uniaxial load-elongation curve, giving the stress-strain properties, $\sigma(\epsilon)$, including the failure strength σ_f and the elastic modulus E, should be measured according to the Tappi standard T494 os-70, [98].
- The descending part of the load-elongation curve, giving the stress-widening $\sigma(w)$, i.e. fracture softening properties of the fracture region including fracture energy G_f, should only be measured in the MD and CD with short paper strips that give stable fracture. It is recommended to use a distance between the grips of 5 mm and a paper strip 15 mm wide.

The ascending part of the load-elongation curve transformed to the stress-strain relation for the short paper strip gives the same result as for the long paper strips if the ratio between the width and the length of the specimen is less than 0.15. However, the descending part of the stress-elongation curve is found to be approximately independent of the variation of the paper strip width and different stable paper lengths. It was observed that the crack path is perpendicular to the load for uniaxial loads in the MD and CD.

The elastic-cohesive softening model implemented as a user's subroutine into a commercial finite element code is able to describe the experimentally observed anisotropic fracture softening behavior.

The simulations of the central cracked rectangular sheet (CCS) specimen reveal that the concept of autonomy in a region near the crack edge does not in general prevail, except at small scale yielding (SSY), since the crack opening displacement, δ_t, versus the extent of the process region ahead of the crack tip, R, gives different curve responses for the short and long CCS specimens. So, the process region near the crack edge can therefore not generally be described by only one unique parameter, e.g. the J-integral.

The estimate of the limit load with the cohesive softening model gives a good prediction of the experimentally obtained limit loads, cf. Table 6.1.

However, a crucial drawback is that the hardening plasticity phenomenon in paper is not included in the elastic-cohesive crack theory. This can explain a disagreement found between the measured and simulated results for the CCS loaded in the CD.

The web simulations with the axehead-shaped opening for different cases are given in Table 7.3. It is concluded from the cases in Table 7.3 that the metal layer for all the cases exhibits damage in front of the slits. It is also shown that it is equally effective to decrease the damage in the front slits by adding three paperboard bridges in the front slits so as to increase the metal foil from 9 μm to 12 μm. Furthermore, the paperboard and polymer layers are found to be unaffected at the web tension of 2100 N/m.

From the excellent agreement between the experimental and simulated performance of a U-shaped opening, it is concluded that finite element simulations of the in-plane mechanical behavior in the converting process can be made in order to get a better understanding of how a punched opening device behaves in the converting process.

8.3 Future development

In-plane behavior

The in-plane rate-independent behavior of paper in tension has been discussed in this thesis, both from experimental, theoretical and computational points of view. The fracture behavior has, however, been modelled on the assumption that the failure criterion during the course of softening is smooth and convex. This assumption should be studied experimentally. Additional experimental verification of the model is needed also with respect to oblique crack growth. Moreover, a test method for pure shear fracture tests is needed in order to get experimental results regarding the fracture softening perfomance in shear.

An elastic-plastic hardening model which models the anisotropic hardening behavior of paper more accurately than the present KB model would be of value. Of course, an even better goal to strive for is a unified elastic-plastic hardening cohesive-softening constitutive model.

For analysis of situations with bending or strong in-plane compression, the compression failure performance of paper is of great importance. It is probable that strain localization develops also during compression failure, but in other respects the compressive failure is different from tensile failure and there is a need both for modelling and for better understanding of the compressive failure performance.

All aspects of the in-plane behavior are related to the microstructure of the material: fiber properties, microstructure geometry and properties of the fiber-to-fiber connection. Because of this there should be much to be learned from loading of specimens under a microscope and from simulations by network models.

Out-of-plane behavior

The out-of-plane behavior is important in many technical applications, e.g. bending and creasing. Some preliminary attempts to measure the mechanical properties have been made, cf. [27, 73], and some initial attempts to model the out-of-plane

behavior have been made by Karafillis et al. [50]. Karafillis et al. applied their model to the creasing problem and found that the out-of-plane shear behavior is a governing factor at through-thickness compression. However, the through-thickness stress-strain behavior is the least understood and the most difficult to characterize. Hence more research is needed to obtain a full understanding of the problem. The damage evolution during bending and creasing is an important feature, and also a complex one, that needs further studies if we are to understand the underlying mechanical mechanisms in detail.

Coupling behavior

The coupling behavior between in-plane and out-of-plane is an important feature that must be well understood and investigated in order to obtain a complete constitutive description and understanding of paper.

Bibliography

[1] Andersson H. and Bergkvist H., "Analysis of a non-linear crack model", *J. Mech. Phys. Solids*, 18, 1-28 (1970).

[2] Andersson O. and Falk O., "Spontaneous crack formation in paper", *Svensk Papperstidn.*, 69, 91-99 (1966).

[3] Andersson O. and Sjöberg L., "Tensile studies of paper at different rates of elongation", *Svensk Papperstidn.*, 56(16), 615-624 (1953).

[4] Aronsson C.-G. , "Tensile fracture of composite laminates with holes and cracks", *Report No 84-5, Royal Institute of Technology*, Stockholm, Sweden, 1984.

[5] Barenblatt G. I.,"The formation of equilibrium cracks during brittle fracture. General ideas and hypotheses. Axially-symmetric cracks." *Prikl. Math. Mekh.* 23(3):434-444 (English transl. *J. Appl. Mech.* 23, 622-636) (1959).

[6] Baum G. A., "The elastic properties of paper: a review", Eds. P. Kolseth, C. Fellers, L. Salmén and M. Rigdahl, in Design criteria for paper performance., STFI-MEDDELANDE A 969, (1987).

[7] Baum G. A., Brennan D. C. and Habeger C. C., "Orthotropic elastic constants of paper", *Tappi J.*, 64(8), 97 (1981).

[8] Bažant Z. P., "Mechanics of distributed cracking", *Appl. Mech. Rev.*, 39(5), 675-705 (1986).

[9] Bažant Z. P. and Li Y-N.,"Cohesive crack model for geomaterials: Stability analysis and rate effect", *Appl. Mech. Rev.*, 6(2), S91-S96, (1994).

[10] Bažant Z. P. and Pijaudier-Cabot G.,"Nonlocal continuum damage, localization instability and convergence", *ASME J. Appl. Mech.*, 55, 287-293(1988).

[11] Besseling G. A. and van der Giessen E., *Mathematical Modelling of Inelastic Deformation*, Chapman & Hall, (1994).

[12] Bither T. W. and Waterhouse J. F., "Strength development through refining and wet pressing", *Tappi J.*, p. 201- 208, November (1992).

[13] Broberg K. B.,"The formulation of fracture mechanics", *Engng Fracture Mech.*, 16, 497-515 (1982).

[14] Broberg K. B.,"Fracture mechanics- theoria or tekhne?", *Int. J. Fracture*, 57, 85-99 (1992).

[15] Broberg K. B.,"Critical review of some methods in nonlinear fracture mechanics", *Engng Fracture Mech.*, 50, 157-164 (1995).

[16] Borst R. De and Mühlhaus H. B.,"Gradient-dependent plasticity: Formulation and algorithmic aspects", *Int. J. Numer. Meth. Eng.*, 35, 512-539 (1992).

[17] Borst R. De,"Smeared cracking, plasticity, creep and thermal loading- a unified approach", *Comp. Meth. Appl. Mech. Engng.*, 62: 89-110 (1987).

[18] Cannmo P., Runesson K. and Ristinmaa M., "Modelling of plasticity and damage in polycrystalline microstructure", *Int. J. of Plasticity* (to appear).

[19] Cavlin S.,"Sprödhetsmodul och kritisk längd", *Swedish Pulp and Paper Inst.*, PA B:78, nr 290 (1974).

[20] Choi D. and Thrope J. L.,"Progressive deformation at the crack tip in paper during Mode I fracture. Part 1- bond paper", *Tappi J.*, October 1992, 127-134 (1992).

[21] Corte H., "Faserstructur und physikalische Eigenschaften von Papier", *Das Papier*, 16, 575-587 (1962).

[22] Cosserat E. et Cosserat F., "Théorie des Corps Deformables", *Hermann, A. et Filis*, Paris, (1909).

[23] Cox H. L., "The elasticity and strength of paper and other fibrous materials", *Brit. J. Appl. Phys.*, **3**, 72-79 (1952).

[24] Dahl M. and Taskinen S., Tetra Brik Packaging system S.p.a., *Via Delfini 1*, I-411 00 Modena, Italy.

[25] Dahlblom O. and Ottosen N. S., "Smeared crack analysis using generalized fictitious crack model", *J. Engrg. Mech.*, 116(1), 55-76 (1990).

[26] Eringen A. C., *On Nonlocal Plasticity*, Prentice-Hall, 1981.

[27] Fellers C., "Procedure for measuring the interlaminar shear properties of paper", *Svensk paperstidn.*, no. 3, pp. 89- 93 (1977).

[28] Fellers C., "Bruchzähigkeit- eine neue methode zur charakterisierung von papier", *Das Papier.*, Heft 7 1993, 345-352, (1993).

[29] Fellers C., Westerlind B. and Ruvo A. De, "An investigation of biaxial failure envelope of paper: experimental study and theoretical analysis" in *Proc. 7th Fund. Research Symp.*, Cambridge, UK (1981).

[30] Fellers C., Fredlund M. and Wågberg P., "Die-cutting toughness and cracking of corrugated board", *Tappi J.*, April 1992, 103-109, (1992).

[31] Fleck N. A., Müller G. M., Ashby M. F. and Hutchinson J. W., "Strain gradients plasticity: theory and experiment", *Acta Metall. Mater.*, 42, 475-487(1994).

[32] Goldschmidt J. and Wahren D., "On the rupture mechanism of paper", *Svensk Papperstidn.*, 71 (1968) 477.

[33] Griffith A. A.,"The phenomena of rupture and flow in solids", *Phil. Trans. Royal Soc.*, A221, 163-198, (1920).

[34] Gunderson D. E. and Rowlands R. E., "Determining paperboard strength- biaxial tension, compression and shear", *Intern. Paper Phys. Conf.*, pp. 253- 263, (1983).

[35] Gustafsson P. J., "Fracture mechanics studies of non-yielding materials such as concrete", *Ph.D. Thesis LUTVDG/(TVBM-1007)/1985*, Div. of Building Materials., Lund, 1985.

[36] Hellan K.,*Introduction to fracture mechanics*, MacGraw-Hill, Inc., (1984).

[37] Helle T., "Fracture mechanics of paper", in *Design criteria for paper performance*, eds. Kolseth P., Fellers C., Salmén L. and Rigdahl M., STFI-meddelande A 969, (1987).

[38] Heyden S. and Gustafsson P.-J., "A network model for application to cellulose fibre materials", *in the 7th Int. Conf. on Mech. Behaviour of Materials*, May 1995, The Netherlands (1995).

[39] Hibbitt, Karlsson & Sorensen Inc., ABAQUS/Standard version 5.4, Pawtucket, R.I. (1994).

[40] Hill R., *The Mathematical Theory of Plasticity*, Clarendon Press, Oxford. (1950).

[41] Hill R., "A user-friendly theory of orthotropic plasticity in sheet metals", *Int. J. Mech. Sci.*, Vol. 35, No. 1, pp. 19-25 (1993).

[42] Hillerborg A., Modeer M. and Petersson P. E., "Analysis of crack formation and crack growth in concrete by means of fracture mechanics and finite elements", *Cement and Concrete Research*, Vol. 6, 773-782 (1976).

[43] HINDMAN H. and BURR G. S., "The Instron tensile tester", *(Trans.) ASME*, 71, pp. 789, (1949).

[44] HOSFORD W. F., "A generalized isotropic yield criterion", *J. Mech. Phys. Solids*, **39**, 607 (1972).

[45] IRWIN G. R., "Analysis of stresses and strains near the end of a crack traversing a plate", *J. Appl. Mech.*, 24: 361-364 (1957).

[46] JONES A. R., "An experimental investigation of the in-plane elastic moduli of paper", *Tappi*, 51(5): 203- 209 (1968).

[47] KALLMES O. and CORTE H., "The structure of paper I. The statistical geometry of an ideal two dimensional fibre network", *Tappi*, **43**, 737-752 (1960).

[48] KALLMES O. J., in *Theory and Design of Wood and Fiber Composite Materials* (Jaynne, B. A., Ed.), p. 117 (1972).

[49] KARAFILLIS A. P. and BOYCE M. C., "A general anisotropic yield criterion using bounds and a transformation weighting tensor", *J. Mech. Phys. Solids*, **41**, 1859 (1993).

[50] KARAFILLIS A. P., BOYCE M. C. and PARKS D. M., A Constitutive Model for the Anisotropic Elastic-Plastic Behavior of Paperboard, *Seminar and Workshop: Constitutive Modelling for Time-Dep. Materials, Dec. 8-9, 1994, STFI*, Stockholm, (1994).

[51] KHAN A. S., and HUANG S. *Continuum Theory of Plasticity*, John Wiley & Sons Inc., (1995).

[52] KNUTSSON M., Multi-Physics Engineering AB, *IDEON Research Park*, S-223 70 Lund, Sweden, (1995).

[53] KOITER W. T.,"Couple stresses in the theory of elasticity, I and II", *Proc. Ned. Akad. Wet. (B)*, 67(1), 17-44 (1964).

[54] LAU C. C., *A Fracture Mechanics Approach to Adhesion of Packaging Laminates*, Ph. D. thesis, Dept. of Mech. Eng., Imperial College, United Kingdom, (1993).

[55] LEKHNITSKII S. G., *Theory of Elasticity of an Anisotropic Body*, Mir Publishers, (1981).

[56] LUBLINER J., *Plasticity Theory*, MacMillan Publ. Comp. (1990).

[57] MAGNUSSON A. and ÖSTENSSON L. , "Tetrapak: Folieytans Microutseende efter Sträckning", *Technical Report (in Swedish)*, Aluminium Teknik, Gränges, 1988.

[58] MANN R. W., BAUM G. A. and HABEGER C. C., "Determination of all nine orthotropic elastic constants for machine-made paper", *Tappi*, 63(2): 163- 166 (1980).

[59] MASING G.,"Eigenspannungen und Verfestigung beim Messing", *Proc. 2nd Int. Congr. Appl. Mech.*, Zurich, 332 (1926).

[60] MAUGIN G. A., *The Thermodynamics of Plasticity and Fracture*, Cambridge University Press, (1992).

[61] MELAN E.,"Zur Plastizität des räumlichen Kontinuums", *Ing. Archiv.*, 9, 116-126 (1938).

[62] MISES R. VON, "Mechanik der festen Körper im Plastisch deformablen Zustand", *Göttinger Nachrichten, Math.-Phys. Klasse*, 582 (1913).

[63] MÜHLHAUS H. B. and AIFANTIS E. C.,"A variational principle for gradient plasticity.", *Int. J. Solids Struct.*, 28, 845-857(1991).

[64] NAGTEGAAL J. C.,"On the implementation of inelastic constitutive equations with special reference to large deformation problems", *Comp. Meth. Appl. Mech. Engng.*, 33: 469-484 (1982).

[65] NILSSON C., "On nonlocal plasticity, strain softening and localization", *Ph.D. Thesis LUTVDG/(TVSM-1007)/1994*, Dep. of Structural Mech., Lund, 1994.

[66] NISSAN A. H., "The rheological behavior of hydrogen-bonded solids", *Trans. Faraday Soc.*, 53: 700-702, (1957).

[67] OROWAN E., "Notch brittleness and the strength of metals", *Trans. Inst. Engrs. Shipbuilders*, Scotland 89, 165 (1945).

[68] OSWIN C. R., *Plastic Films and Packaging*, Applied Science Publishers Ltd (1975).

[69] PAETOW R. and GÖTTSCHING L., "Querkontraktionszahl von Papier", *Das Papier*, 44(6), (1990).

[70] PAGE D. H., "A theory for the tensile strength of paper", *Tappi*, 5(4): 674-681 (1969).

[71] PAGE D. H. and SETH R. S., "The elastic modulus of paper: II. The importance of fibre modulus, bonding and fibre length" *Tappi*, 63(6): 113- 116 (1980).

[72] PERKINS R. W., MARK R. E., COSBY C. and EUSUFZAI A. R. K., "A study of the inelastic behavior of paper", *Int. Paper Phys. Conf.*, 105- 110 (1983).

[73] Persson K. , "Material Model for Paper: Experimental and Theoretical Aspects", *Diploma Report, Lund University*, Lund, Sweden, 1991.

[74] Petersson P.-E., "Crack growth and development of fracture zones in plain concrete and similar materials", *Ph.D. Thesis LUTVDG/(TVBM-1006)/1981*, Div. of Building Materials., Lund, 1981.

[75] Pierce F. T., "Theorems on the strength of long and of composite specimens", *J. Text. Inst.*, 17 (1926) T355.

[76] Rice J. R.,"A path independent integral and the approximate analysis of strain concentration by notches and cracks", *J. Appl. Mech.* 35: 379-386 (1968).

[77] Ristinmaa M., *Cyclic Plasticity and Its Numerical Treatment*, Ph. D. thesis, Dept. of Solid Mechanics, University of Lund, Sweden, (1993).

[78] Ristinmaa R. and Vecchi M., "Use of Couple-Stress Theory in Elasto-Plasticity", *Comp. Meth. Appl. Mech. Engng.*, (To appear).

[79] Ruvo A. De, Carlsson L. and Fellers C., "The biaxial strength of paper", *Tappi J.* 63(5): 133 (1980).

[80] Sachs I. B. and Kuster T. A., "Edgewise compression failure mechanism of lineboard observed in a dynamic mode", *Tappi J.* 63(10): 69 (1980).

[81] Salmén L., Carlsson L. A., Ruvo A. De, Fellers C. and Htun M., "A treatise on the elastic and hydroexpansional properties of paper by a composite laminate approach", *Fibre Sci. Tech.*, 20: 283-296 (1984).

[82] Schellekens J. C. J., "Computational strategies for composite structures", *Dissertation*, Delft University of Technology, Faculty of Civil Engineering, Delft, The Netherlands, 1992.

[83] Schreyer H. L., "Analytical solutions for nonlinear strain-gradient softening and localization", *ASME J. Appl. Mech.*, 57, 522-528(1990).

[84] Schulgasser K. and Page D. H.,"The influence of transverse fibre properties on the in-plane elastic behaviour of paper", *Composites Sci. Techn.*, 32, 279-292 (1988).

[85] Seth R. S.,"On the work of fracture in paper", *Tappi J.*, 62 (7), 92 (1979).

[86] Seth R. S.,"Measurement of in-plane fracture toughness of paper", *Tappi J.*, 78 (10), 177-183 (1995).

[87] Seth R. S. and Page D. H.,"Fracture resistance in paper", *J. Material Sci.*, 9, 1745-1753 (1974).

[88] Seth R. S. and Page D. H.,"Fracture resistance: a failure criterion for paper", *Tappi J.*, 58 (9), 112 (1975).

[89] Setterholm V. C., Benson R. and Kuenzi E. W., "Method for measuring edgewise shear properties of paper", *Tappi J.* 51(5): 196 (1968).

[90] Shallhorn P. M. , "Fracture resistance- theory and experiment", *J. Pulp and Paper Sci.* 20(4): 119-123 (1994).

[91] Simo J. C. and Taylor R. L.,"Consistent tangent operators for rate-independent elastoplasticity", *Comp. Meth. Appl. Mech. Engng.*, 48: 101-118 (1985).

[92] Steadman R. and Fellers C., "Fracture toughness characterization of paper at different climates", *1987 Int. Paper Physics Conf.*, Auberge Mont Gabriel Mont-Rolland, Quebec, Canada (1987).

[93] Steenberg B.,"Behaviour of paper under stress and strain", *Pulp and Paper Mag. of Can.*, 50, pp. 220 (1949).

[94] Strömberg L. and Ristinmaa M., "FE-formulation of a Nonlocal Plasticity Theory", *Comp. Meth. Appl. Mech. Engng.*, Vol. 136, 127-144 (1996).

[95] Shuling J. C., Johnson M. W., Rowlands R. E. and Gunderson D. E., "Nonlinear elastic constitutive relations for cellulosic materials", in *Mechanics of cellulosic and polymeric materials*, Ed. R. W. Perkins, ASME, AMD- Vol. 99, 1- 13 (1989).

[96] Swinehart D. E. and Broek D., "Tenacity©, fracture mechanics, and unknown coater web breaks", *Tappi J.*, 79 (2), 233-237 (1996).

[97] Tappi T 403 om-85, "Bursting strength of paper".

[98] Tappi T 494 os-70, "Tensile breaking properties of paper and paperboard (using constant rate of elongation apparatus)".

[99] Tresca H., "Sur l'écoulement des corps solides soumis á de fortes pressions", *Comptes Rendus Acad. Sci.*, **59**, 754 (1864).

[100] Tryding J., "A modification of the Tsai-Wu failure criterion for the biaxial strength of paper", *Tappi J.*, 77 (8), 132 (1994).

[101] Tvergaard V. and Needlemann A., "Analysis of the Cup-Cone Fracture in a Round Tensile Bar", *Acta Metallurgica*, **32**, 157 (1984).

[102] Xikui Li, Duxbury P. G. and Lyons P.,"Considerations for the application and numerical implementation of strain hardening with the Hoffman yield criterion", *Comput. Struct.*, 52(4): 633-644 (1994).

[103] WARD I. M. and HADLEY D. W., *An Introduction to the Mechanical Properties of Solid Polymers*, John Wiley & Sons (1993).

[104] WEIBULL W.,"A statistical theory of the strength of materials", *Proceedings no. 151*, Ingeniörsvetenskapsakademien (1939).

[105] WERNERSSON H., "Fracture characterization of wood adhesive joints", *Ph.D. Thesis LUTVDG/(TVSM-1006)/1994*, Dep. of Structural Mech., Lund, 1994.

[106] ÖSTLUND S. and NILSSON F., "Cohesive modelling of process regions for cracks in linear elastic structures- fundamental aspects", *Fatigue Fract. Engng Mater. Struct.*, 16(2), 215-235(1993).